

Modification of Anti-Bacterial Activity and Bone Cell Proliferation by Surface Engineering of Ga- or Mn-Doped Ceria-Coated Biomedical Titanium Alloy

Author:

Khosravanihaghighi, Ayda

Publication Date:

2022

DOI:

<https://doi.org/10.26190/unsworks/2005>

License:

<https://creativecommons.org/licenses/by/4.0/>

Link to license to see what you are allowed to do with this resource.

Downloaded from <http://hdl.handle.net/1959.4/100095> in <https://unsworks.unsw.edu.au> on 2024-04-24

Modification of Anti-Bacterial Activity and Bone Cell
Proliferation by Surface Engineering of Ga- or Mn-Doped
Ceria-Coated Biomedical Titanium Alloy

Ayda Khosravanihaghi

Doctor of Philosophy



Faculty of Science

School of Materials Science and Engineering

UNSW Sydney

Feb 2022

THE UNIVERSITY OF NEW SOUTH WALES
Thesis/Dissertation Sheet

Surname or Family name: **Khosravanihaghighi**

First name: **Ayda**

Other name/s:

Abbreviation for degree as given in the University

calendar: **PhD**

School: **School of Materials Science and Engineering**

Faculty: **Faculty of Science**

Thesis Title

Biological Performance of Undoped and Doped CeO₂ Films on Ti-Alloy Implants

Thesis Abstract

CeO₂ thin films (~820 nm thickness) doped with 0-9 mol% Ga or Mn were fabricated by spin coating on 3D-printed Ti6Al4V followed by heat treatment at 650°C for 2 h, and these were characterised by TEM and FESEM (microstructure), 3D laser scanning confocal microscopy (topography), GAXRD (structure and mineralogy), and XPS (surface chemistry). *In vitro* testing was conducted including inhibition of bacterial growth, SBF testing, and cell attachment and proliferation studies.

The data are interpreted in terms of the following: (1) The roles of the sol-gel precursor viscosity, which affected pore filling and surface coverage, (2) Lattice contraction, which contradicted the XPS data, (3) Intervalence charge transfer, which increased the Ce³⁺ concentration but was a minor effect, (4) Substitutional solid solubility, which is consistent with Hume-Rothery's rules and the GAXRD data, (5) Redox charge compensation, where the defect equilibria highlight the key role of this mechanism, which decreased the Ce³⁺ concentration and provided the majority effect, (6) Electronegativity, which plays a small, if any, role in affecting the ion valences but is important in initiating intervalence charge transfer, (7) Multivalence charge transfer, which combined the electron exchanges between film matrix, dopants, and Ti substrate.

The most significant outcome was that the bioactivity of ceria derives directly from the Ce³⁺ concentration, which itself results from solid solubility (substitutional *and* interstitial) and charge compensation and redox. This challenges the common assumption of the dominance of oxygen vacancies in the performance of ceria. The antibacterial activity was dependent on the type, amount, and valence of the dopant, where opposite trends were observed for gram-positive *S. aureus* and gram-negative *E. coli* bacteria. All of the doped samples resulted in enhanced cell proliferation, although this was greatest at the lowest dopant concentration. Surface hydroxyapatite formation on the samples was achieved by soaking in SBF at 2 weeks and 1 month.

ORIGINALITY STATEMENT

☒ I hereby declare that this submission is my own work and to the best of my knowledge it contains no materials previously published or written by another person, or substantial proportions of material which have been accepted for the award of any other degree or diploma at UNSW or any other educational institution, except where due acknowledgement is made in the thesis. Any contribution made to the research by others, with whom I have worked at UNSW or elsewhere, is explicitly acknowledged in the thesis. I also declare that the intellectual content of this thesis is the product of my own work, except to the extent that assistance from others in the project's design and conception or in style, presentation and linguistic expression is acknowledged.

COPYRIGHT STATEMENT

☒ I hereby grant the University of New South Wales or its agents a non-exclusive licence to archive and to make available (including to members of the public) my thesis or dissertation in whole or part in the University libraries in all forms of media, now or here after known. I acknowledge that I retain all intellectual property rights which subsist in my thesis or dissertation, such as copyright and patent rights, subject to applicable law. I also retain the right to use all or part of my thesis or dissertation in future works (such as articles or books).

For any substantial portions of copyright material used in this thesis, written permission for use has been obtained, or the copyright material is removed from the final public version of the thesis.

AUTHENTICITY STATEMENT

☒ I certify that the Library deposit digital copy is a direct equivalent of the final officially approved version of my thesis.

UNSW is supportive of candidates publishing their research results during their candidature as detailed in the UNSW Thesis Examination Procedure.

Publications can be used in the candidate's thesis in lieu of a Chapter provided:

- The candidate contributed **greater than 50%** of the content in the publication and are the "primary author", i.e. they were responsible primarily for the planning, execution and preparation of the work for publication.
- The candidate has obtained approval to include the publication in their thesis in lieu of a Chapter from their Supervisor and Postgraduate Coordinator.
- The publication is not subject to any obligations or contractual agreements with a third party that would constrain its inclusion in the thesis.

☒ The candidate has declared that **their thesis contains no publications, either published or submitted for publication.**

Candidate's Declaration



I declare that I have complied with the Thesis Examination Procedure.

ACKNOWLEDGMENTS

Throughout my thesis project I have received a great deal of support and assistance.

I would first like to thank my supervisor, Professor Chris Sorrell, whose expertise was invaluable in in-depth material analysis and methodology. His insightful feedback and support helped me to learn a lot and bring my work to a higher level.

I would like to thank my joint supervisor, Dr. Pramod Koshy for his continued support and invaluable advice.

I would like to extend my appreciation to my co-supervisors and all of my collaborators, Dr. Kristopher Killian, Dr. Vedran Lovric, Dr. Sara Romanazzo, Dr. Muhammad Yasir, Prof. Mark Willcox, and Dr. Ghazaleh Bahman Rokh, since conducting the work would have been impossible without their significant support and patience.

I owe thanks to a very special person, my husband, Ehsan for his continued and unfailing love, support and understanding during my PhD project. I also would like to gratitude my lovely sister and parents, for their unconditional love and support that helps me always to believe in myself and progress in my life. I would never achieve anything without their help and support.

ABSTRACT

The two leading causes of failure of orthopaedic implants are aseptic loosening and periprosthetic joint infection. Since the numbers of primary and revision joint replacement surgeries are increasing, strategies to mitigate these failure modes have become increasingly important. However, most recent work has focused on the design of coatings to prevent infection or to enhance bone mineralisation. However, long-term success of the implants is contingent on addressing both of these issues. Consequently, the present work focussed on multifunctional orthopaedic coatings that inhibit microbial cells while still promoting osseointegration. Nanoceria has considerable potential to be used in biomedical applications owing to its unique bio-responsive redox switching and its capacity to be doped with different therapeutic ions of varying functionalities. Therefore, the effect of different cations incorporated in ceria on cellular behaviour *in vitro* as well as the anti-bacterial performance were investigated. The two main foci were: (1) characterisation of the bioceramic materials and (2) biological response to undoped and doped ceria ceramics *in vitro* using bacteria colonies forming unit (CFU) and cytotoxicity

Ceria (CeO_2) thin films (~ 820 nm thickness) doped with 0-9 mol% Ga or Mn were fabricated by spin coating on 3D-printed Ti6Al4V followed by heat treatment at 650°C for 2 h, and these were characterised by transmission electron microscopy (TEM) and field emission scanning electron microscopy (FESEM) (microstructure), 3D laser scanning confocal microscopy (topography), glancing angle X-ray diffraction (GAXRD) (structure and mineralogy), and X-ray photoelectron spectroscopy (XPS) (surface chemistry). *In vitro* testing was conducted, including inhibition of bacterial growth, simulated body fluid (SBF) testing, and cell attachment and proliferation studies.

The data are interpreted in terms of the following: (1) The roles of the sol-gel precursor viscosity, which affected pore filling and surface coverage, (2) Lattice contraction, which contradicted the XPS data, (3) Intervalence charge transfer, which increased the Ce^{3+} concentration but was a minor effect, (4) Substitutional solid solubility, which is consistent with Hume-Rothery's rules and the GAXRD data, (5) Redox charge compensation, where the defect equilibria highlight the key role of this mechanism, which decreased the Ce^{3+} concentration and provided the majority effect, (6) Electronegativity, which plays a small, if any, role in affecting the ion valences but is important in initiating intervalence charge transfer, (7) Multivalence charge transfer, which combined the electron exchanges between film matrix, dopants, and Ti substrate.

The most significant outcome was that the bioactivity of ceria derives directly from the Ce^{3+} concentration, which itself results from solid solubility (substitutional *and* interstitial) and charge compensation and redox. This challenges the common assumption of the dominance of oxygen vacancies in the performance of ceria. The antibacterial activity was dependent on the type, amount, and valence of the dopant, where opposite trends were observed for gram-positive *S. aureus* and gram-negative *E. coli* bacteria. All of the doped samples resulted in enhanced cell proliferation, although this was greatest at the lowest dopant concentration. Surface hydroxyapatite formation on the samples was achieved by soaking in SBF at 2 weeks and 1 month.

Table of Contents

	Page
ACKNOWLEDGEMENTS	i
ABSTRACT	ii
LIST OF TABLES	vi
LIST OF FIGURES	vii
 CHAPTER	
 1. Introduction	1
1.1 Aims of Project	4
 2. Literature Review	5
2.1 Metallic Orthopaedic Implants	5
2.2 Bone Morphology	10
2.2.1 Bone Morphogenetic Factor	13
2.3 Orthopaedic Implants - Challenges and Solutions	14
2.3.1 Osseointegration	15
2.3.2 Bacterial Infection	29
2.4 Properties of Ceria	45
2.4.1 Non-Biological Applications of Ceria	46
2.4.2 Biological Applications of Ceria	48
2.5 Anti-Microbial and Bioactivity Applications of Ceria	52
2.5.1 Bacterial Infection Inhibition	52
2.5.2 Promoting Bone Formation	54
 3. Material Preparation and Characterization	56
3.1 Materials	56

3.2 Material Characterization	56
3.3 Sample preparation	57
3.4 Characterization	58
3.4.1 Microstructure and Mineralogical Properties	58
3.4.2 Biological Analysis	60
4. Results and Discussion – Coating Characteristics	65
4.1 Surface and Chemical Characterization	68
4.1.1 Field Emission Scanning Electron Microscopy (FESEM) and Transmission Electron Microscopy (TEM)	68
4.1.2 3D-Laser Scanning Confocal Microscopy	69
4.2 Mineralogical Properties	73
4.2.1 Raman Microspectroscopy	73
4.2.2 X-ray Diffraction (XRD)	74
4.2.3. X-Ray Photoelectron Spectroscopy (XPS)	90
4.3 Summary and Conclusions	103
5. Results and Discussion – Biological Performance	105
5.1 Antibacterial Assays	106
5.2 Acellular Mineralisation (Apatite Formation)	112
5.2.1 SBF	119
5.3 Cell Adhesion and Proliferation Assays	124
6. Summary and Conclusions	130
6.1 Research Recommendation	135
References	136

LIST OF TABLES

Table 2.1. An overview of metal implants.....	9
Table 2.2. An overview of bone morphogenetic proteins (BMPs) and their applications in human body.13	
Table 2.3. Osseintegration challenges and possible solutions	Error! Bookmark not defined.
Table 2.4. Bacterial infection challenges and possible solutions	Error! Bookmark not defined.
Table 2.5. Summary of some therapeutic ions and their biological functions	41
Table 2.6. Non biological applications of ceria.....	Error! Bookmark not defined.
Table 2.7. Biological applications of ceria	Error! Bookmark not defined.
Table 2.8. Comparison of mechanical properties of cortical bone, Ti6Al4V, and CeO₂ Error! Bookmark not defined.	
Table 3.1. Comparison of ionic concentrations in blood plasma and prepared SBF	61
Table 4.1. Crystallographic data for CeO₂ coatings calcined at 650°C for 2 h	79
Table 4. 2. Relevant Shannon crystal radii.....	81
Table 4.3. Crystallographic data for 3D-printed Ti6Al4V after heating at 650°C for 2 h	87
Table 4.4. Reported electronegativities of Ti, Ce, Ga, and Mn in different scales	90
Table 4. 5. XPS surface compositions for Ce, Ga, and Mn (at%).....	92
Table 4.6. Potential defect equilibria for substitutional and interstitial solid solubilities and ionic and electronic charge compensation for both valences of matrix (Ce³⁺, Ce⁴⁺) and three valences of dopants (Mn²⁺, Mn³⁺, Mn⁴⁺) and (Ga⁺, Ga³⁺, Ga⁴⁺).....	97
Table 5.1. Relative proportions of thin film phases following soaking in SBF based on maximal GAXRD peak heights.....	Error! Bookmark not defined.
Table 6. 1. Summative comparison of data.....	Error! Bookmark not defined.

LIST OF FIGURES

Figure 2.1. Light micrographs of portions of alveolar bone of rat showing giant multinucleated osteoclasts (Oc), bone matrix (B), osteocyte (Ot), polarized osteoblast (Ob)	11
Figure 2.2. Spongy and compact bone	12
Figure 2.3. SEM micrograph of eXalt pore structure	17
Figure 2.4 Schematic of biological responses to bioactive ions	45
Figure 4. 1. Thermodynamic stability diagrams of the (a) Ce-O system, (b) Ga-O system, and (c) Mn-O system calculated using FACT-Sage 7.0 and modified by other references (Chen et al., 2015, Asadian, 2012, Kang and Jung, 2016b, A. Nicholas Grundy, 2002, Kang and Jung, 2016a)	66
Figure 4. 2. TEM images: (a) cross section of undoped CeO ₂ -coated sample; FESEM images: (b) uncoated substrate, (c) undoped CeO ₂ coating, (d-f) Ga-doped CeO ₂ coatings, (g-i) Mn-doped CeO ₂ coatings; coatings calcined at 650°C for 2 h; GC = Ga-doped CeO ₂ ; MC = Mn-doped CeO ₂ ; preceding numbers = dopant level (mol%, metal basis).....	69
Figure 4.3. 3D laser scanning confocal microscopy image of surface topographies: (a) Summary of roughnesses (Ra), (b) uncoated substrate, (c) undoped CeO ₂ coating, (d-f) Ga-doped CeO ₂ coatings, (g-i) Mn-doped CeO ₂ coatings; coatings calcined at 650°C for 2 h	71
Figure 4.4. Undoped, Ga-doped, Mn-doped CeO ₂ samples: Top – Transparencies of sols, Middle – Viscosities of sols deposited on smooth Ti substrates, Bottom – Comparative viscosities of sols (left – 1 mol% dopant, middle – 5 mol% dopant, right – 9 mol% dopant) deposited on smooth Ti substrates	72
Figure 4.5 Laser Raman microspectra of (a) undoped, Ga-doped, and Mn-doped CeO ₂ sol-gel films (unannealed) and fused SiO ₂ substrate; (b) Ga-doped CeO ₂ coatings, (c) Mn-doped CeO ₂ coatings; calcined at 650°C for 2 h (identical peak intensity ranges)	74
Figure 4.6. GAXRD patterns of: (a) Ga-doped CeO ₂ coatings, (b) Mn-doped CeO ₂ coatings; coatings calcined at 650°C for 2 h (identical peak intensity ranges except for the uncoated substrate)	75
Figure 4. 7 Gibbs free energies of formation for (a) possible film-substrate reactions, (b) Mn oxides at various temperatures (TiO ₂ is rutile polymorph).....	77
Figure 4.8. Calculated sizes of interstices in CeO ₂ (<u>Ce^{VIII}4 += 0.111 nm, O^{IV}2-= 0.124 nm</u>)	78

Figure 4.9. Graphical Rietveld analytical data for: (a) lattice parameters, (b) unit cell volumes, (c) crystallite sizes for (left) uncoated and CeO₂-coated substrates, (centre) Ga-doped CeO₂ coatings, (right) Mn-doped CeO₂ coatings, all with corresponding Ti6Al4V data; coatings calcined at 650°C for 2 h..... 86

Figure 4. 10. XPS spectra: (a) Ce3d for undoped and Ga-doped CeO₂-coated substrates, (b) Ce3d for undoped and Mn-doped CeO₂-coated substrates, (c) O1s for undoped and Ga-doped CeO₂-coated substrates, (d) O1s for undoped and Mn-doped CeO₂-coated substrates, (e) 2P_{3/2} for Ga-doped CeO₂-coated substrates, (f) 2P_{3/2} and 2P_{1/2} for Mn-doped CeO₂-coated substrates, (g) Ti2p3 for undoped and Ga-doped CeO₂-coated substrates, (h) Ti2p3 for undoped and Mn-doped CeO₂-coated substrates; coatings calcined at 650°C for 2 h (peak identifications based on data from National Institute of Standards and Technology XPS database..... 91

Figure 4. 11. Relative XPS data: (a) effects of Ga dopant level on Ce levels, (b) effects of Mn dopant level on Ce levels, (c) effects of Ga and Mn dopant levels on Ce/O and Ce⁴⁺/Ce³⁺ ratios 93

Figure 4.12. Representative IVCT reactions and integrated role of MVCT reactions for Ga-doped and Mn-doped CeO₂ thin films deposited on Ti-based substrates 103

Figure 5.1. Structural differences between the cell walls of gram-positive and gram-negative bacteriaError! Bookmark not defined.

Figure 5. 2. *S. aureus* and *E. coli* bacterial reduction: (a) Ga-doped samples, (b) Mn-doped samples, *S. aureus* and *E. coli* bacterial adhesion (relative to control (uncoated sample): (c) Ga-doped samples, (d) Mn-doped samples, (e) *S. aureus* and *E. coli* bacterial survival rates after 24 h incubation (bacterial concentration = CFU/mL; * $p < 0.05$, ** $p < 0.01$, * $p < 0.001$, and **** $p < 0.0001$) Error! Bookmark not defined.**

Figure 5. 3. GAXRD patterns (intensities scaled identically) of: (a) CeO₂-coated substrate, (b) HA reference peaks according to ICDD 01-074-0565, (c-e) Ga-doped CeO₂ coatings, (f-h) Mn-doped CeO₂ coatings; calcined at 650°C for 2 h followed by immersion in 200 mL SBF solution for 2 weeks or 1 monthError! Bookmark not defined.

Figure 5. 4. FESEM images of HA precipitation after immersion in SBF for 2 weeks or 1 month: (a,b) positive control, (c,d) CeO₂-coated, (e,f) 1GC, (g,h) 5GC, (i,j) 9GC, (k,l) 1MC, (m,n) 5MC, (o,p) 9MC; calcined at 650°C (insets: 10 µm scale bar)..... 117

Figure 5. 5. ICP-OES results for ionic concentrations of residual SBF after immersion for 2 weeks or 1 month: (a) Ce, (b) Ga, (c) Mn (single-point data) and (d) Ca, (e) P (multiple-point data), (f) Ca/P ratio; calcined at 650°C for 2 h (* for 5GC (a) was off-scale)Error! Bookmark not defined.

Figure 5. 6. GAXRD pattern of positive control after immersion in 200 mL in SBF for 1 month; powder sample placed on glass substrate (inset shows the amorphous hump at $\sim 23^\circ 2\theta$ / 0.387 nm)..... Error! Bookmark not defined.

Figure 5. 7. (a) and (b) Cell attachment and proliferation of MG-63 cells cultured up to 7 days on: TCP, uncoated, CeO₂-Coated, Ga-doped CeO₂ coated, and Mn-doped CeO₂ coated substrates analysed by the MTS assay (OD at 490 nm), and (c) and (d) effects of dopants on cytotoxicity values (for samples cultured for 7 days) and [Ce] from XPS data.....Error! Bookmark not defined.

Figure 5. 8. FESEM images of cell attachment (4 h) and cell proliferation (2 days) following seeding by MG-63 cells on the substrates for: (a,b) uncoated, (c,d) CeO₂-coated, (e-j) Ga-doped CeO₂-coated, and (k-p) Ga-doped CeO₂-coated substrates (10 μ m scale bar)Error! Bookmark not defined.

1. Introduction

There is an increasing demand for orthopaedic implants owing to the increase in the numbers of aging population. Different materials have been used for these applications over the years. In ancient times, wood, gold and ivory were used as implants for repairing craniofacial defects. In World War II, pilots used polymethylmethacrylate (PMMA), a non-degradable polyacrylate, as intraocular implantation during aircraft crashes [1]. During the 1960s and 1970s, the research in implants was focussed on enhancing mechanical integrity while immune response was not given much importance [2]. Later on, research started to focus on the chemical and physical properties and their impact on the biological response of the body to these implants.

Carbon- and vanadium-based implant materials have been replaced by stainless steel, passivated cobalt-chromium alloys, and titanium alloys while polymers, nylons and polyesters have been replaced by polytetrafluorethylene (PTFE), PMMA, polyethylene, and silicones owing to their *inert* nature [3]. Since these materials do not have a biologically active surface to stimulate osseointegration or prevent infection, additional coatings are needed to address these mentioned problems. Such a coating should be biocompatible, osteoinductive and have mechanical stability and anti-microbial properties.

The optimal choice of materials for implants depends on a combination of design, structural, microstructural, mechanical, chemical, and physiological issues [4]. Titanium-based alloys have emerged as the lead metallic material for implants owing to their bioinertness, biocompatibility, and potential for the introduction of bioactivity through surface modification. Pure titanium is used mostly for dental implants, whereas the titanium alloy Ti6Al4V is used most commonly for orthopaedic implants.

Although biocompatibility and adequate bulk mechanical properties are the starting points for orthopaedic biomaterials, ancillary factors, such as corrosion resistance and surface roughness, also are important [5]. This is the case because the biological response to an implant involves cell adhesion, proliferation, and differentiation, which are dependent on factors including surface chemistry, energy, and wettability [6, 7]. A different sort of consideration is the potential for the bacterial adhesion that causes biofilm formation, which can preclude cell attachment as well as osseointegration [8, 9]. Therefore, the modification of implant surfaces aims at improving both biocompatibility and antibacterial activity [10].

Consequently, there has been a commensurate amount of work in the surface engineering of metallic implants [11] according to two strategic directions. The first strategy is surface modification of the implant itself [12], including but not limited to sand blasting, anodisation, etc. The second strategy involves the deposition of thin films [13-15], including but not limited to sputtering, electrodeposition, anodization, dip coating and sol-gel dip/spin coating, etc. Of the preceding techniques, sol-gel spin coating is recognised one of the simplest and most economic processes for the application of thin films [14-21]. The surface materials used to enhance the bioactivity include *in situ* passivating TiO₂ [22], *ex situ*, applied TiO₂ [23], hydroxyapatite layer [24], hybrid inorganic-organic coating (*e.g.*, apatite/collagen coatings [25]), glass-ceramic coating [26], and ceramic-metal composite coating [27].

In addition to bioactivity, the other factors to consider are the potential for antibacterial characteristics [28, 29] and the effectiveness of cell attachment to the implant [30, 31]. To these ends, a range of physical and chemical surface modifications has been developed. For the introduction of antibacterial functionality, these include but not limited to bactericidal

coating [32], and altered surface topography (to expose nanowires [33], nanotubes [34], or cicada wings [35]). For the enhancement of cell attachment, several techniques have been used [10], including calcium phosphate coating [36], biomolecular coating [37], and engineered surface topography [38]. Strategies to combine inhibition of bacterial infection and enhancement of cell attachment involve the inclusion of therapeutic ions [39-45] into resorbable metallic alloys [46] and resorbable coatings [47] as well as the modification of surfaces by methods such as ion implantation [48], as summarised in Table S1. Ce^{3+} , Ga^{3+} , and Mn^{2+} have been shown to inhibit bacterial growth while stimulating apatite formation and osteoblast growth and proliferation. Further, these ions incorporated as oxide particles have been shown to exhibit low toxicity and beneficial effects against *S. aureus* and *E. coli*, which suggests their potential for *in vivo* applications as antibacterial coatings [49-54].

Currently none of the commercial prosthesis in use have all the above-mentioned desired characteristics [55]. Most studies have focussed either on osseointegration or antibacterial infection with these two factors being interconnected [10]. Right after implantation, the implant provides a ready surface for host cell or bacterial colonisation. If host cells win the ‘race’, strong tissue integration and prevention of microbial attachments will occur [56]. In general, the prosthesis lifespan is 15 to 20 years. However, owing to issues, some implants need to be replaced prior to the due date [57]. Thus, further investigations are recommended to achieve long-term success of the implants.

The principal aim of the present work was to improve the performance of orthopaedic implants through the use of coatings of biocatalytic CeO_2 deposited on biomedical grade Ti6Al4V alloy. Improvement in the bioactivity of the CeO_2 thin films was explored through the effects of Ga or Mn doping on the resultant structural, microstructural, and chemical effects as well as the

antibacterial performance and osteoblastic cell proliferation.

1.1 Aims of Project

As mentioned previously, orthopaedic implants are essential biomedical devices but they remain subject to some drawbacks that reduce their lifespans [58]. The major issues to be overcome are bacterial infection and aseptic loosening [10, 59, 60]. Consequently, many researchers have investigated these two issues individually [10]. Consequently, many researchers have investigated these two issues individually [10]. The present work aims to enhance bone cell attachment and proliferation and reduce the bacterial growth by changing the surface composition of Ti-based implants. To this end, 3D-printed Ti6Al4V substrates with specific surface roughness were obtained and spin coated with sol-gel CeO₂. The thin films were doped with either Ga³⁺ or Mn²⁺ and heat treated at 650°C for 2 h in air. The physical properties were investigated in terms of the microstructures, mineralogies, and chemical compositions. The biological properties were investigated in terms of the culturing of *E. coli* or *S. aureus* bacteria and MG-63 bone cells on the samples in order to evaluate the antibacterial performance and bone cell growth, respectively.

2. Literature Review

This review presents some major challenges associated with the performance of existing implant materials. There will be focus on coatings on implant surfaces and their effects on enhancing osseointegration and anti-microbial characteristics.

2.1 Metallic Orthopaedic Implants

Owing to the superior mechanical properties of metals and alloys, these are used for biomedical applications. The benefits and drawbacks of different metallic materials for implants are given in **Table 2.1**. Navarro *et al.* categorised the implants into three categories, namely bioinert (no interaction with biological tissue), bioactive (induces growth of living organisms, tissues or cells), and biodegradable (decomposed by biological means) [61]. Gold is used in facial surgeries including dental and eyelid implantation [62] for tarsorrhaphy, which is a surgical procedure to narrow the eyelid using gold wire implants [63]. However, according to Hench, bioinert materials result in loose adhesion between the implant and the host tissue and lack the capability to defend the immune system of the body because of their inert surface [64]. Stainless steel (SS 316 L) is another metal that is used as an implant; its advantages include low cost, high availability, good corrosion resistance, and ease of fabrication; however, its use for permanent orthopaedic implants has been restricted owing to poor mechanical stability, fatigue strength, and wear resistance [61, 65].

Tantalum was a rare-earth metal introduced by Burke in 1940 for use in subcutaneous, tendon repairing [66]. Wang *et al.* revealed that by the production of nanotubular tantalum surface through anodizing, the corrosion, hydrophilicity, and surface energy increased in comparison to pure tantalum. Moreover, the nanotubes stimulated the differentiation of osteoblast cells which helped to increase the biocompatibility [67, 68]. However, there are some disadvantages

including the high elastic modulus (>186 GPa), high density (16.6 g/cm³), and difficulty in fabrication of different shapes [68, 69]

Cobalt-chrome alloys are another group of implants that are a good alternative to stainless steels; these have better corrosion resistance owing to the formation of a durable passive layer on the surface and good mechanical properties. Cobalt-chrome alloys contain cobalt, chromium, molybdenum, and nickel with the latter two contributing to enhancing the corrosion resistance [70]. However, the major issue is that chromium and nickel are carcinogenic and have been found in blood and urine samples of people with implants [65].

Owing to these issues, titanium and its alloys (CP Ti, Ti6Al4V) have become increasingly used in the biomedical industry since they can address all of the previously mentioned issues [61]. In comparison to the two former materials, titanium shows good corrosion resistance and biocompatibility, and this derives from the protective titanium oxide (TiO₂) layer [70]. Pure titanium (CP Ti) with alpha microstructure is mostly used in dental implants, whereas titanium alloy (Ti6Al4V) with alpha-beta phases is used in orthopaedic implants. The presence of aluminium and vanadium in the alloy enhances the mechanical strength of titanium alloys [61]. Implants composed of pure titanium have been seen to be prone to fatigue corrosion [71-73] and thus titanium-zirconium (TiZr1317: 83-87% Ti and 13-17% Zr) alloys have been developed for use as dental implants and show higher mechanical stress resistance than implants with pure titanium; patients prefer these group of implants because of the colour which mimics teeth better; however, drawbacks include their price and limitation for several applications [74].

Generally, titanium alloys have been seen to be biocompatible and non-toxic, except when the materials are produced by powder metallurgy and also contain molybdenum, niobium, and silicon [75]. Li *et al.* demonstrated that there is an optimal limit since higher concentrations can trigger cytotoxicity [76]. Another group of implants are magnesium alloys with the extensive investigation being done to enhance their biocompatibility and mechanical strength. Since Mg-alloys have similar Young's modulus to that of for the bone ($E=10-30$ GPa), there is a lower chance of stress shielding. However, these show low corrosion resistance and produce hydrogen gas, which results in a high degradation rate of surrounding tissues [77].

The optimal choice of materials for implants depends on a combination of design, structural, microstructural, mechanical, chemical, and physiological issues [4]. However, recent work has focussed on tailoring implants to increase their bioactivity so that they can induce mineralization and bone regeneration [78]. One method is to fabricate a coating to stimulate cell nucleation and proliferation, since metallic implants do not have bioactive characteristics [61]. The three major types of coatings used for Ti-implants are as follows: hydroxyapatite (HA) which is a type of calcium phosphate (CaP), [79], bioactive glasses [80], and organic coatings. Titania coatings, owing to their non-toxicity and antibacterial properties are an interesting material for use as implant coatings [81].

Organic biomolecular coatings are composed of organic components present in bone and are divided into four categories, namely extracellular proteins (ECM) such as collagen or peptides, bone growth factor (BMP-2, BMP-7), immobilised DNA (Deoxyribonucleic acid) for reinforcing structure and enzyme-like coatings [79, 82, 83]. Having an organic-inorganic composite coating is another development for improving the characteristics of Ti-implants [84]. Alam *et al.* evaluated different pellet-shaped implants composed of five ratios of HA/beta

tricalcium phosphate (β -TCP), as carriers for recombinant human bone morphogenetic protein-2 (rhBMP-2) and they concluded that the regeneration of bone showed a direct relation with HA-TCP ratio and the presence of high amounts of Recombinant human BMPs(rhBMP) [85]. Similarly, tests on using co-precipitated CaP and BMP-2 on Ti-alloy discs showed that adding BMP-2 into CaP coatings resulted in samples that could help with osteogenesis [86].

Another method to make implants bioactive and to enhance osseointegration is to modify the implant surface to promote deposition and cell adhesion to the surface [61]. Fabricating titania nanotubular (TNT) surfaces is one method that has been used to tailor the architecture and this is achieved by anodization, where the pore sizes can be controlled by changing the processing conditions, thereby improving the potential for cell adhesion, growth, and differentiation [87, 88]. The use of lasers is another method to modify the implant surfaces and this can provide better advantages in tailoring the surface in comparison to methods like grit-blasting, acid-etching, and anodic oxidation [89].

Apart from being bioinert and bioactive, another important desirable characteristic is biodegradability for implants coatings [61]. A biocompatible coating or implant that degrades after a certain amount of time is called biodegradable [90]. Ma *et al.* fabricated 3-D microporous hydrogel coatings containing chitosan and gelatine via electrophoretic deposition method (EPD) on titanium alloys. Both *in vitro* and *in vivo* tests revealed significant degradation after 28 days as well as attachment and proliferation of cells and formation of new bone, respectively [91]. Enhancement in the osseointegration of Ti-implant was tested by delivery of BMP-2 from biodegradable nanoparticles of chitosan-tripolyphosphate (CS-TPP) coating, and it was revealed that the degree of biodegradation of CS-TPP coating was chitosan dose-dependent [92]. Maria *et al.* gained interesting results by doping gallium (Ga) into

chitosan/poly (acrylic acid) coatings which were then electrodeposited on Ti-implants. This showed a reduction in *Escherichia coli* (*E. coli*) and *Pseudomonas aeruginosa* (*P. aeruginosa*) growth without affecting osseointegration, which even increased osteoblastic differentiation at the primary stages [93]. Boris *et al.* introduced another property called biomimicry and this refers to smart biomaterials that involve fabricating cells, tissues, and organs by synthetic methods similar to those seen in biochemical processes [94].

Table 2.1. *An overview of metal implants*

	<i>Advantages</i>	<i>Disadvantages</i>	<i>Applications</i>	<i>Ref.</i>
<i>Gold</i>	Bio-inert	Decrease immunity system	Facial	[62]
<i>Stainless Steel</i>	Low cost, easy to shape, corrosion resistance	Poor mechanical resistance	Fracture plates, hip nails, screw	[65]
<i>Tantalum</i>	Corrosion resistance, and increase osteoblast cells	High modulus and density	Bone	[66]
<i>Cobalt-Chrome Alloys</i>	Corrosion resistance, and mechanical strength	Carcinogen	Joint replacement	[70]
<i>Titanium-Zirconium Alloys</i>	Mechanical strength	Expensive and minimal application	Dental implant	[74]
<i>Titanium and Ti-Alloys</i>	Corrosion resistance, biocompatibility	Hard to shape, expensive	Prosthetics, Implants, Screw	[61]

<i>Magnesium Alloys</i>	Biocompatible, low stress shielding, light weight	Corrosion, hydrogen evolution	Screw, plates, pins, Biodegradable orthopaedic devices	[77]

2.2 Bone Morphology

Bone is a porous tissue (vessels and red bone marrow canals) and the hardest organ of the body and comes in different shapes depending on the function, and provides mechanical support to soft tissues. Broad and flat like scapula play a role as anchors for big muscles, on the other hand, hollow with thick walls like femur, the ulna and the radius bear weight and perform as a lever arm [95].

Bone contains a fluid phase, a solid structure, and cells, which are composed of extracellular matrix (amorphous and fibrous) and cells (osteoblasts), bone lining cells, osteocytes, and osteoclasts [96]. Bone cells are covered by a large matrix called ‘extracellular matrix’ (ECM); the matrix consists of inorganic salts including calcium and phosphate ions along with hydroxyapatite. The organic matrix provides flexibility for bone and is composed of collagenous protein (mostly collagen type I), non-collagenous protein like osteonectin, sialoprotein, osteocalcin, bone morphogenetic proteins (BMPs), and growth factor [96-99]. Osteoblasts cells, that differentiate from mesenchymal cells, are the large cells with the responsibility for synthesizing and mineralizing bone [100, 101]. Osteoblast cells are derived from organic matrix deposition followed by mineralization [96]. A matrix producing osteoblasts (**Figure 2.1**) is influenced by one of the three stages: elimination by apoptosis, engagement in mineralization, or remaining intact on the bone surface as bone lining cells, which are flat-layers and covering bone surface. Wein showed that these cells play significant roles within the cycle of remodeling bone matrix [102].

Osteocyte cells are 90-95% of the whole bone cells as seen in **Figure 2.1** and have long lifetimes of up to 25 years [98]. These cells are different from osteoblasts and osteoclasts and they result from mesenchymal stem cells (MSCs) via differentiation of osteoblast cells. During bone mineralization, osteoblast cells establish osteoid, non-mineralized bone matrix, and changes into osteocytes.

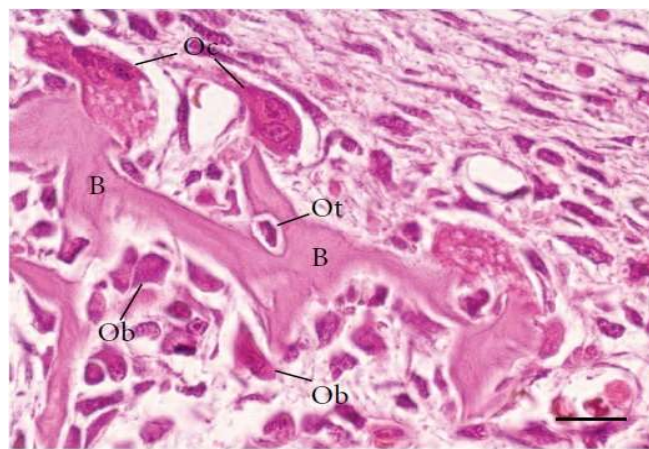


Figure 2.1. Light micrographs of portions of alveolar bone of rat showing giant multinucleated osteoclasts (Oc), bone matrix (B), osteocyte (Ot), polarized osteoblast (Ob)

Scale bar: 15 μm . [96]

Osteoclast cells differentiate multinucleated cells and result in dissolution and absorption of bone tissue through the occupation of the pits on the bone surface called How to ship's lacunae. There are some common skeletal diseases deriving from osteoclasts like osteoporosis which causes the lower density of bone and bone fracture. Moreover, Charles *et al.* revealed that osteoclasts were not limited only to bone resorption but also interfere in osteoblast differentiation during the cycle of bone's remodelling [96, 103].

Orthopaedic implants are commonly classified as osteoinductive, osteoconductive, and osseointegration. Briefly, osteoinductive refers to primitive, undifferentiated, and pluripotent cells, in which, embryonic stem (ES) cells are pluripotent cells and are induced to differentiate into osteogenic precursors, which are capable of proliferating and differentiating into osteoblasts and lead to bone cells formation [104] which are stimulated to develop into the bone-forming cell lineage or induce osteogenesis. Osteoconductive means bone grows on the surface or down into pores, channels or tubes. Lastly, osseointegration points to direct contact between existing bone and implant surface and results in the formation of bony tissue around the implant without the formation of fibrous tissues [105]. In general bone matrix not only provides bone cell support but also play an important role in bone cell adhesion [106, 107].

Bone matrix is divided into two groups: bundle bone (in fracture healing) and lamellar bone (fibrous bone). Weiner *et al.* described the lamellar bone structure as composed of five sublayers with different orientations and called it multifunctional [108]. Lamellar bone (osteon units) is divided into two categories: compact bone and spongy bone. The former refers to dense bone and is filled with organic substances e.g., collagen and inorganic salts which contain bone cells (osteoblasts), lymphatic and blood vessels and nerves [109]. Spongy bone (**Figure 2.2**), trabecular or cancellous bone is light and provides protection for red bone marrow and most of the flat, irregular, short, and the epiphyses (end of the long bones) structures are composed of this kind of bone [110].

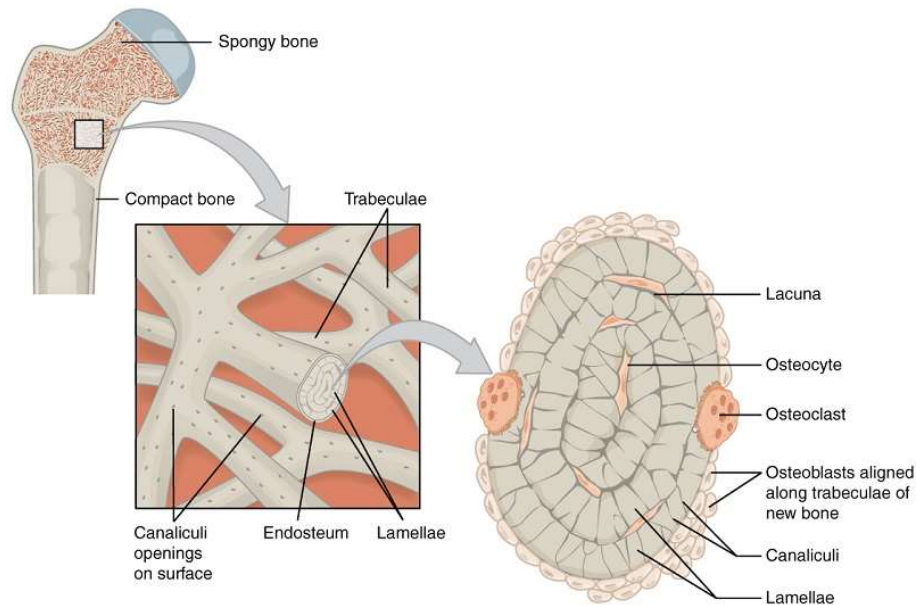


Figure 2.2. Spongy and compact bone [110]

2.2.1 Bone Morphogenetic Factor

Bone morphogenetic factors (BMPs) are growth factors, known as metabologens and cytokines [111], that modulate and differentiate mesenchymal cells and were first discovered in 1965 [112-114]. Signal transmission through intracellular signals (SMAD) causes immobilizing of proteins which plays an important role in the development of bone, cartilage and central nervous system (CNS) during the early stages of human bone formation [115]. There are different types of BMPs (BMP-1 to BMP-15) with BMP-2 to BMP-15 belonging to transforming growth factors (**Table 2.2**); these growth factor proteins are highly used in bone-related issues [83, 116, 117]. According to Groeneveld *et al.*, the osteoinductive efficiency of BMPs is dependent on their concentration, properties of their carriers, and local growth factors [118].

Table 2.2. *An overview of bone morphogenetic proteins (BMPs) and their applications in human body [118]*

BONE MORPHOGENETIC FACTOR	APPLICATION
---------------------------	-------------

BMP-2	Bone induction
BMP-3	Bone induction
BMP-4	Bone induction
BMP-5	Skeletal formation in embryology
BMP-6	Bone induction
BMP-7	Bon induction
BMP-8 - BMP-11	No report of osteoinductive nature
BMP-12	Inhibition of terminal myoblast differentiation
BMP-13	Inhibition of terminal myoblast differentiation & ectopic induction of tendon and ligament
BMP-14	Ectopic induction of tendon and ligament
BMP-15	No report of osteoinductive nature

2.3 Orthopaedic Implants - Challenges and Solutions

Of the two leading causes of implant failures, poor osseointegration was responsible for ~18% of failures and bacterial infection accounted for ~20% of failures [10]. Osseointegration depends on success in fixation initially, during surgery, and postoperatively. However, aseptic loosening can occur owing to implant micromotion relative to the host bone, which triggers the generation of wear particles and consequent inflammation [10]. Although aseptic loosening and bacterial infection generally are unrelated, recent work has revealed that aseptic loosening can stimulate bacterial infection [119]. Consequently, it is relevant to examine both issues simultaneously despite their general acceptance as independent variables.

Infections generally are considered to be capable of propagating into durable biofilms when the number of bacterial colonies exceeds $\sim 10^2$ colony-forming units (CFU) [120, 121]. Two of the most common sources of bacterial infection at implant sites are *Staphylococcus aureus* (*S.*

aureus) and *Escherichia coli* (*E. coli*), which are gram-positive and gram-negative, respectively [122, 123]. The former is responsible for approximately two-thirds of all implant infections [29, 124]. In addition, the success of an implant after surgery is strongly dependent on the adhesion and growth of healthy cells, which result in osseointegration followed by tissue integration [125]. Alternatively, if pathogens attach and propagate, the resultant bacterial infection can lead to implant failure.

2.3.1 Osseointegration

Orthopaedic implants are mostly used for fracture fixation (e.g. spinal fixation devices, fracture plates, wires, pins and screws) and joint replacement (arthroplasties for hip, knee, ankle shoulder, elbow, wrist and finger) [101]. Osseointegration is the formation of a direct connection between structural and functional properties of living bone and the surface of the implant [126]. Osseointegration is highly dependent on two important stages in the implantation procedure. First is the consistency of the implant during surgery, which is the surgeon's responsibility. Secondly, implant loosening tends to occur with time with aseptic loosening being the reason for major prosthesis replacement. Osseointegration challenges and possible solutions are summarized in **Table 2.3**. Increasing the amounts of physical activity has resulted in higher load on implants and this has increased the risk of interface motion and subsequent failure of implants [59]. A small micromotion of implants may influence the bone regeneration and inhibit bone ingrowth [127].

Wear debris is another issue which derives from the implant system and this has numerous implications such as osteolysis and failure of the implant [128]. To approach this problem, Fournier *et al.* developed a novel orthopaedic implant coating material which is called “eXalt”, which was composed of superelastic nitinol wire that was knitted into 3-dimensional spacer fabric structure (**Figure 2.3**). The presence of this coating resulted in better initial fixation with

in vivo tests showing improvement in bone growth [129]. Poor matching between bone moduli (10-30 GPa) and the moduli of the material (Ti-alloys: 110 GPa and Co-Cr alloy: 230 GPa) [130] has been found to be a major culprit of loosening of biomaterial and stress shielding of bone. Fixation can be achieved by employing a porous matrix of metal which has low elastic modulus. So, by designing a metal with a close modulus to the bone, improved bone ingrowth is achievable [131]. Von sees developed the pre-augmentation of the soft-tissue expansion with hydrogel expanders with the aim of higher functional microvessel density which resulted in more rapid osseointegration [132]. Furthermore, a biodegradable osteoconductive hydrogel scaffold, containing transforming growth factor- β (TGF- β) and insulin-like growth factor-1 (IGF-1), could induce bone generation [133]. Although recombinant human bone morphogenetic proteins (rh-BMPs) have considerable potential in bone formation, the optimal local delivery system is the key issue that should be explored. That is why a composite comprised of poly-D, L-lactic acid-*p*-dioxanone-polyethylene glycol block copolymer (PLA-DX-PEG) with the molar ratio of 45:17:38 and molar weight of ~9500, *p*-dioxanone was used as a biodegradable material to control the rate of degradation and which was synthesized by ring-opening polymerization, briefly 25 mg of PLA-DX-PEG was diluted and liquidized in acetone then added to the different amount of rhBMP-2 following by soaking in type I collagen sponge disk, lyophilizing and finally squeezing to form the implant with 25 μ l volume. Radiographic and histologic examinations revealed new bone formation and could be used for larger defect areas in the bone [134].

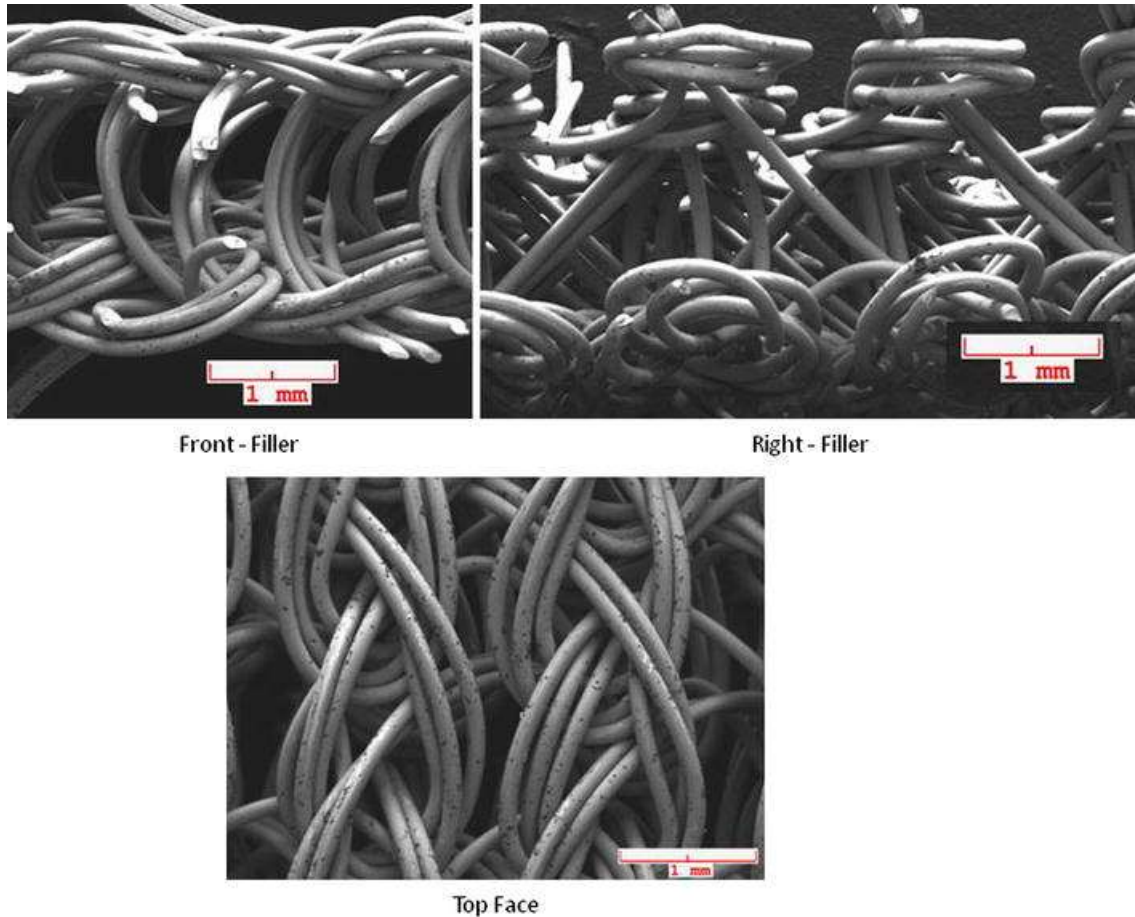


Figure 2.3. SEM micrograph of eXalt pore structure [129]

Poor bone in-growth on implants is another issue. A possible solution to address this problem is coating the surface [105]. Hydroxyapatite (HA) is commonly used as the coating and is a CaP subclass [135]. To optimize the HA coating properties in terms of osseointegration and prevention of bacterial infection, additives are added. Varying concentration of zinc (0, 2, 5, 10, 15 mol %) has been added to HA via the sol-gel method. It was revealed that the higher Zn-dopant (15 mol%) and the higher calcination temperature (900°C) resulted in better bioactivity and better mechanical strength [136]. Fielding *et al.* doped 2 wt% silver (Ag) and 1 wt% strontium (Sr) into hydroxyapatite (HA) coating and concluded that additives have a positive effect on cell proliferation and differentiation activity after 11 days, compared with undoped HA samples [137]. Gloria *et al.* developed 3D magnetic nanocomposite scaffolds for

bone tissue engineering by doping iron (Fe) into HA (0.1 mol of FeCl₂ and FeCl₃: in 75 ml of H₂O). They reached the conclusion that the resulting nanocomposite promoted osteogenic differentiation [138].

Lithium (Li)-doped HA has been widely investigated. According to Wang *et al.*, *in vitro* tests revealed that Li-doped HA in low amounts (0.5 mol%) resulted in higher strength, and this was accompanied by fast osteoblast-mediated degradation rate and osteoblast activity [139]. Organic additives have also been used to enhance HA performance. Jing *et al.* used collagen along with 2.5 µg of rhBMP-2 and 0.5 µg arginylglycylaspartic acid peptide (RGD) and this mixture was successfully infiltrated into porous HA coatings and *in vivo* tests showed enhanced bone formation and mesenchymal cell (MSC) proliferation [140]. Researchers also fabricated HA nanoparticles complexed with chitosan into nanoscale nondegradable electrostatic multilayers which were capped with a degradable poly(β -amino ester)-based film incorporating physiological dose (250 µg/ml) of rhBMP-2. They demonstrated upregulating of osteogenic markers and MSC differentiation, which resulted in an improvement in calcium deposition in shorter times compared to a substrate containing only HA or rhBMP-2 [141].

Improving surface topography is another technique that can promote interactions between osteogenic cells while limiting bacterial infection. A new surface architecture (OsteoAnchor) for orthopaedic stem cell components has been developed through the fabrication of anchor-like surface architecture on the surface of the implants using a direct metal laser sintering method. Through the friction test, the ratio of transverse force to applied normal force was measured, this ratio for stem applications confirmed the motion resistance of stem against transverse load. Moreover, the fixation of OsteoAnchor was obtained via micromotion test with the highest mean value of 10.48 µm being much lower than that seen for the plasma

sprayed stem with the value of 16.14 μm . This work resulted in growing hard bone, rather than fibrous tissue into porous substrates. Hence, long-term and secure fixation, especially in the primary stages of the implantation was observed to occur [142, 143].

Lan *et al.* used a combination of two surface modifications including nanostructures generated by acid etching, which provides the excellent rough surface with suitable topography and roughness, and ultraviolet (UV) treatment. They found that the modification method resulted in lower rate of bacterial infection and improved bone mesenchymal stem cells [144]. Another technique of modifying the implant surface is anodic oxidation, which previously has been shown to induce bone formation by promoting cell adhesion and differentiation. In general, anodic oxidation results in a surface with nanopits and the hydrophilic nature of these areas would provide a situation for cells to grow, attach, and proliferate more readily [145].

Hall *et al.* examined anodic oxidation on Ti-alloy beads for hip arthroplasty in H_3PO_4 and this led to increased bone ingrowth and decrease in the formation of fibrous tissue (limiting the growth of fibroblasts) [146]. Huang *et al.* produced hierarchical structure (micro/submicron/nano-scale) on Ti-substrate through three inexpensive cumulative methods, including sequentially-conducted sandblasting as well as primary and secondary acid etching treatment. This resulted in improved antibacterial ability and excellent osteoconductivity for the modified surfaces and these were mainly attributed to high surface area which increased mechanical binding, provided peri-implant tissues regeneration followed by enhancement of protein adsorption, which confirms biological fixation [147, 148].

Bioactive glasses, which are degradable ceramic materials that contain key elements and molecules to encourage osteogenesis, offer another solution to improve osseointegration.

Cattini *et al.* worked on suspension plasma sprayed (SPS) bioactive glass coatings. They deposited bioactive glass on the surface of implant with the aim of adhesion improvement between orthopaedic implants and bone. They concluded that the best degree of crystallinity and porosity could be achieved at a hydrogen flow rate of 7.5 slpm (standard litre per minute) with the spray distance of 50 to 70 mm and power of 36 to 40 kW. *In vitro* tests revealed the formation of a surface layer of hydroxy-carbonated-apatite after immersion in simulated body fluid (SBF) [149].

Patel *et al.* fabricated chitosan/nano bioactive glass (CH-BGn) coatings through electrophoretic technique (EPD). They came to the conclusion that CH-BGn coatings have acceptable cell adhesion and growth and promoted osteogenic differentiation through culturing pre-osteoblastic MCT3-E1 on coatings and showed antibacterial effect against *Streptococcus* mutants which was confirmed by Na-ampicillin drug model [150, 151]. In another research, bioactive composite orthopaedic coatings with antibacterial capability containing chitosan, Bioglass[®] particles (9.8 μm), and silver nanoparticles (Ag-NPs, 50 nm), were deposited on stainless steel 316 through electrophoretic deposition (EPD). On immersion in SBF, HA formation was revealed which made the coating bioactive. With the sustained release of silver ions from the coating, it showed antibacterial properties. Moreover, cellular attachment and proliferation were achieved through appropriate levels of incorporation of silver in the composite coating [152].

Das *et al.* made a newly engineered composite coating containing bioactive glass-ceramic, which was grafted with 58 mol% porous silica (SiO_2) nanofibers on inert glass. Homogeneous growth of flake-like carbonated HAP layer was formed on the surface; the cell adhesion and proliferation resulted from the embedded porous silica nanofibers which increased

hydrophilicity [153]. Another group fabricated bioactive glass coatings by laser cladding on ceramic acetabular cups for hip joint prosthesis. They produced surfaces with curved geometry rather than flat ones and this resulted in excellent joins between glass and ceramic substrate, leading to good bioactive behaviour and the formation of an apatite layer by immersion in SBF [154].

In order to eliminate the poor mechanical properties, Trafder *et al.* applied microwave sintering to promote the mechanical strength of 3D printed β -TCP scaffolds with 3D interconnected macropores. *In vitro* tests showed that an increase in sintering temperature would decrease the pore size; the smaller the pore sizes (500 nm), the greater the living cell density, and *in vivo* tests demonstrated that both micro- and macropores promoted osteogenesis in a rat femur model [155]. In further research by this group, 1 wt% of each strontium oxide (SrO) and magnesium oxide (MgO) were doped into TCP; *in vivo* tests showed increased bone formation. Tests with rat femoral defect models showed increasing extracellular matrix (ECM) formation and acceleration of mineralization [156].

To enhance cellular function in response to the implant surface, micro- and nano-scale topography are critical. Maher *et al.* fabricated micro and nano-topography on Ti-implants by electrochemical anodization (with the electrolyte of 0.1 M NH_4F and 1.5 M lactic acid) of 3D printed titanium wafers. Using such a structure (mixture of micro- and nano-topography) helped to improve bone support and localized drug delivery. More interestingly, thanks to their flexibility in design, which resulted from 3D printing, these implants can be made in different shapes and dimensions to meet individual patient needs [157]. Others applied antibacterial coating consisting of polyvinyl alcohol (PVA), polyethylene acid (PAA), and green-

synthesized (Ag-NPs) to the surface of 3D-printed [105] implant and the results showed that bone regeneration increased and bacterial infection rate decreased significantly [158].

Several implant coatings have been investigated to render them osteoinductive, including growth factors and chemokines. Generally, bone is composed of inorganic mineral phase as well as an organic matrix, which is mainly composed of collagen. Collagen is the most abundant protein in extracellular matrix (ECM) proteins. By changing the design of the coatings containing these biological molecules, interesting results can be achieved in terms of bone mineralization [10].

A research study was conducted on osteoblast cell proliferation and differentiation by doping silver (Ag) in hydroxyapatite (HA) coatings (1.0-1.5 wt% of AgNO₃). This study demonstrated that HA coating stimulated osteoconductivity and the addition of Ag enhanced bacterial resistance. HA induced more rapid osseointegration which means higher bony growth and early mineralization at the bone-implant interface compared to uncoated Ti implants [159]. Kazemzadeh-narbat *et al.* tested drug release and bone growth of antimicrobial peptide-loaded (AMP) octacalcium phosphate (OCP) coating on implants. They found out the coating can effectively kill *S. aureus* and *P. aeruginosa* without negatively affecting MG-63 osteoblast like cells [160]. Another group achieved similar results and compared osteoblastic cells and bacterial response for two different nanoparticulates comprised of 0.1 mg/mL clindamycin (antibiotic for bone infection treatments) with one composed of calcium phosphate (CaP) and the other containing poly-(D,L-lactide-co-glycolide)-coated calcium phosphate; the results showed positive response for osteoblast-like cells growth [161].

Hydrogels can be used as materials to mimic the extracellular matrix (ECM) and are composed of synthetic polymers like poly(ethylene glycol) (PEG), poly(vinyl alcohol) (PVA), polyacrylamide (PAM), poly(2-hydroxyethyl methacrylate) (HEMA), poly (vinylpyrrolidone) (PVP), or natural polymers such as collagen, hyaluronic acid (HA), alginate, gelatine, elastin chondroitin sulphate, heparin, dextran, and chitosan [162]. Bone morphogenetic proteins (BMPs) are cytokines and probably the most important growth factors in bone formation and healing. Carriers for the delivery of BMPs range from nanoparticles to complex three-dimensional (3D) scaffolds, membranes for tissue-guided regeneration, biomimetic surfaces, and smart thermosensitive hydrogels. Synthetic polymers, natural origin polymers, inorganic materials and composites may be used as BMP delivery carriers [117].

Shi *et al.* functionalized Ti-alloy substrate by first covalently grafting carboxymethyl chitosan (CMC), followed by conjugation of bone morphogenetic protein-2 (BMP-2) to the CMC-grafted surface. They concluded that this reduced bacterial adhesion and promoted cell attachment, alkaline phosphatase activity, and calcium mineral deposition of both osteoblasts and human bone marrow-derived mesenchymal stem cells (BMSCs) [163].

Although growth factors are very promising molecules to enhance bone regeneration, delivery systems play important roles to translate them to clinical use. The first issue of the delivery system is that the targeted cells receive the optimal concentration of growth factors at the right time. Moreover, safety and cost-effectiveness are also two other key elements that should be taken into consideration [164]. Gene therapy is an effective approach to address the problem of protein delivery of growth factor through safe and efficient non-viral vectors [165, 166].

A collagen scaffold was used to deliver polyethyleneimine (PEI)-plasmid (pDNA) which encoded the fibroblast growth factor (FGF) family that is responsible for secreting and transforming cells, via autocrine cell proliferation [167], platelet derived growth factor-B (PDGF-B) complex. *In vitro* tests showed that PEI-pPDGF-B complex activated collagen scaffolds increased cellular attachment and proliferation [168].

Mishra *et al.* used a growth factor regime of 5 ng/mL basic fibroblast growth factor (FGF-2), 40 ng/mL platelet-derived growth factor (PDGF-BB), and 20 ng/mL epidermal growth factor (EGF) to obtain uniform coverage and higher proliferation of bone marrow-derived human mesenchymal stem cells (BM-hMSCs) of a resorbable poly (propylene fumarate) scaffold. Moreover, to study BM-hMSC differentiation to an ECM-secreting osteoblast, seven experimental groups containing BMP-2, 50 ng/mL BMP-4, 50 ng/mL BMP-6, and 27 ng/mL BMP-7 (explained in section 2.1) along with an osteogenic medium containing 10^{-7} M dexamethasone, 10 mM β -glycerophosphate, and 50 μ g/mL ascorbic acid were chosen. They realized that EGF, FGF-2, and PDGF-BB were the best combination for proliferation, whilst BMP-7 helped in differentiation, and this was successful in combination with osteogenic media [169].

Otsuru *et al.* examined the contribution of osteoblastic cells to osteogenesis in BMP-induced model of ectopic bone formation and they found that employing BMP-2 could stimulate the circulation of bone marrow-derived osteoprogenitor cells (MOPCs) [170]. Higashino *et al.* hypothesized that chemokines, such as stromal cell-derived factor-1 (SDF-1), were involved with mobilization of bone marrow cells. Stromal cell-derived factor-1 α (SDF-1 α) and its cellular receptor CXCR4 have been demonstrated to increase the number of cells produced from the bone marrow and mediate the injured tissues. So, adding 10 μ g SDF-1 to 5 μ g BMP-

2 may result in improvement of the BMP efficiency *in vivo*, which makes them more favourable for use in orthopaedic implants [171]. Hwang *et al.* conducted a similar study on sequential treatment with 0.5 µg SDF-1 and 0.5 µg BMP-2 in calvarial defects. They compared treatments such as periodic percutaneous injections of PBS and the cytokine SDF-1 and BMP-2 into implanted scaffolds. *In vitro* experiments revealed SDF-1 followed by BMP-2 treatment, showed the strongest osteoblastic differentiation and promoted cell migration; the treatment can be a successful strategy for speeding up bone regeneration in critical size defects [172].

Raphel *et al.* focused on engineered protein coatings to enhance bone regeneration of orthopaedic and dental implants. They synthesised recombinantly- and purified-elastin-like protein (ELP) followed by conjugating diazirine into it. Then by dissolving ELP in PBS, the samples were prepared by spin coating for substrates. Alkaline phosphate activity showed an early increase in hMSCs which resulted in fast osteogenic differentiation and mineral deposition on adhesive ELP coatings. As pointed before, micromotion may lead to aseptic loosening and implant failure at very early stages, and for ELP coatings, this issue was controlled by the elastin nature of the coatings, which stable the coating on the surface and this would lead to the cell adherence, and osseointegration [173].

Table 2.3. *Osseintegration challenges and possible solutions* [10]

Challenges	Possible solutions	Ref.
Gaps at implant-bone interface	Biocompatible gap filling	• Knit nitinol wire fabric [129]
		• Hydrogel scaffold [133]
	Calcium phosphate-like coatings	[136]
		• 15 mol% Zn-doped HA [137]
		• (2 Ag/1 Sr) wt%-doped HA [138]
		• Fe-doped HA [139]
		• 0.5 mol% Li-doped HA [140]
		• HA- 1 mL collagen/0.5 RGD-2.5 µg rhBMP-2 [141]
		• 10 wt% HA/chitosan-rhBMP-2
Poor bone in-growth on implant	Engineering surface topography	[142,
		• Anchor-like surface 143]
		• Acid-etching/UV [144]
		• Anodic oxidation [146]
		• Hierarchical structure [147]
	Bioactive glass coatings	• SPS Bioglass® coatings [149]

Challenges	Possible solutions	Ref.
Poor bone deposition on implant surface	<ul style="list-style-type: none"> Chitosan/10% Nano bioactive glass 	[152]
	<ul style="list-style-type: none"> EPD 9.7 μm Bioglass[®]/chitosan/<2.5 ppm Nano-silver 	[153]
	<ul style="list-style-type: none"> Porous SiO₂ (58 mol%) nanofibers grafted bioactive glass-ceramic coating 	
	<ul style="list-style-type: none"> Bioactive glass coatings by laser cladding 	[154]
	3D printing of coatings <ul style="list-style-type: none"> Microwave sintering TCP scaffold 	[155]
	<ul style="list-style-type: none"> 1 wt% SrO & 1 wt% MgO doped in TCP scaffold 	[156]
	<ul style="list-style-type: none"> Electrochemical Anodizing/3D printing 	[157]
	<ul style="list-style-type: none"> 3D-printed implants with antibacterial coating 	[158]
	Biomolecular coatings combining ECM <ul style="list-style-type: none"> HA/1 wt% Ag 	[159]
	<ul style="list-style-type: none"> AMP/OCP 	[160]
	<ul style="list-style-type: none"> 0.1 mg/mL Clindamycin/CaP and Clindamycin/CaP with poly-lactide-co-glycolide 	[161]
Poor bone deposition on implant surface	Biomolecular coating containing growth factors <ul style="list-style-type: none"> 0.1 mL BMP-2 / 10mg/mL CMCS-grafted surface 	[163]
	<ul style="list-style-type: none"> Gene activated matrix (PEI-pPDGF-B) 	[168]
	<ul style="list-style-type: none"> Growth factor regime for PPF scaffolds 	[169]
	Employing osteogenic cells <ul style="list-style-type: none"> BMP-2 	[170]
	<ul style="list-style-type: none"> 0.5 μg SDF-1/ 0.5μg BMP-2 	[172]

Challenges	Possible solutions	Ref.
	<ul style="list-style-type: none"> • ELP-coatings 	[173]

In brief, the two main strategies for promoting osseointegration are (1) altering the implant surface topography or (2) deposition of a coating to enhance implant biocompatibility, cell adhesion, cell proliferation, and hence bone regeneration [174]. The former refers to the alteration of the surface microstructure or nanostructure to improve interactions between bone cells and implant surface [10], generally by roughening the surface topography for mechanical interlocking [175]. The latter refers to coatings on metallic implants to improve bone cell deposition and in-growth at the implant surface. These coatings include calcium phosphate coatings [176], bioactive glass coatings [177], bioinert oxide coatings [178], and biomolecular coatings [179].

These modification strategies can be either individual or a combination of physical, chemical, and/or biological. Physical techniques include machining [180], grit blasting [181], laser treatment [182], plasma spraying [183], and PVD [184]. Chemical procedures include anodisation [146], sol-gel [185], acid etching [181], alkali treatment [186], and CVD [187]. Biological approaches include the recruitment of osteogenic cells by protein-seeding and embedding directly in the porous metal surface [188, 189].

2.3.2 Bacterial Infection

Bacterial infection in orthopaedic implants is still a major issue. Implant surfaces are prone to the risk of infection because of the formation of biofilms which decreases the immune response at the body/implant interface [190]. It has been predicted that the demand for arthroplasty surgeries in the US by 2030 will increase by 673% and 174% for knee and hip replacement surgeries, respectively [191]. It is inevitable that some implants will require revision arthroplasty. Hence, 2017 and 2018 surveys by the National Joint Registries (NJR) of Australia [192] and the US [193] revealed that primary arthroplasty surgeries in Australia increased by

5.7% and 1.1% for knee and hip replacements, respectively, while the respective revision surgeries increased by 7.4% and 8.9%. These numbers were slightly different for the US, where primary and revision arthroplasty surgeries for knee and hip replacements increased respectively 8.2% and 27.3% and by 9.1% and 5.6%. The number-one cause of revision surgery is periprosthetic joint infection since it accounts for 13% of hip and 23% of knee arthroplasty revision procedures according to the 2010 National Joint Registry of England and Wales report [194]. In order to find the best solution to fight off bacterial infections, making the classification and identifying the acuteness or chronicity of the infection is the crucial point that should be taken into account [195]. Kargupta *et al.* categorized orthopaedic infections into three different groups based on the time of infection with respect to the operation: early, delayed, and late [196].

Early infections are described as manifestations of infection at the implant site and normally occur within the first three months after surgery. Virulent microorganisms like *S. aureus* trigger these infections which will be followed by local pain, erythema, edema, wound healing disorder, large hematoma, and fever [197]. At this stage, maintaining the prosthesis may be possible and the patient can recover from the infection by taking effective antibiotics [198]. From 3 months to 2 years, delayed infection may occur, which may be due to the presence of a few initial infecting bacteria, poor growing conditions, or low-virulence bacteria such as *Staphylococci* [195, 197]. Antibiotics which were recommended for early infections cannot be used for this stage.

Normally, a surgical procedure is needed to remove the implant and infected tissue, followed by treatment with local antibiotics. Maintaining the implant can be possible if the fractured implant is still stable, while a fracture is continuously healing [196]. For times greater than 2

years, late-stage infection would result owing to bacterial colonization which is followed by severe pain and surgical procedure to correct it. The prescribed treatments vary for individuals owing to differences in medical history, implant type, and location, infection severity, time of diagnosis, body immune system, and infection location [199].

There are different types of antimicrobial strategies used to fight off bacterial infection but their impacts on osseointegration are not clear [10]. Finding a winning strategy to consider bactericidal effects while targeting bone regeneration has been considered for the following recommended solutions (**Table 2.4**). One practical method would be surface engineering to reduce the adhesion of bacteria on to the implant surface. Making a non-interactive implant surface by using polymer brush like polyethylene glycol (PEG) is extensively used. In one project, poly(L-lysine)-*grafted*-poly (ethylene glycol) (PLL-*g*-PEG) functionalized with RGD (Arg-Asp-Gly)-type peptide, resulted in inhibition of the *S. aureus* adhesion and restoration of fibroblast and osteoblast attachment [200]. Another example of Ti-alloy substrates modification involved covalently linked dextran-grafted surfaces to BMP-2 via a chemical conjugation process, which reduced *S. aureus* and *S. epidermidis* adhesion and enhanced osteoblast function [201].

Another group introduced surface-initiated polymerization (SIP) techniques to induce chain elongation and mechanochemically activate polymer chains. This technique was able to withstand effectively biofouling or act as a low-friction coating [202]. Buzzacchera *et al.* established a system for the coating of implantable devices by growing antifouling polymer brushes from a bioinspired chitosan hydrogel. The polymer brush coatings showed strong and effective resistance to protein fouling and enhanced hemocompatibility [203].

Another alternative solution to promote controlled and rapid healing is to employ nanotube coatings. In one study, nanotubular surfaces were created with anodizing; *in vitro* tests revealed increasing osteoblast differentiation and matrix production and both short-term and long-term osseointegration. Moreover, no inflammation or fibrosis was seen in cell culture tests [87]. Tailoring the Ti-implant surface with silver (Ag) incorporation into titania nanotubes (TiO₂-NTs) is another solution and this enhanced tissue integration and assisted in removal of planktonic bacteria in the first days after implantation; furthermore, it prevented bacterial adhesion for 30 days or more [204].

There is a competition between cell adhesion and bacteria adhesion and thus enhancing osteoblast integration can reduce bacterial colonisation [205]. Peng *et al.* fabricated titanium oxide (TiO₂) nanotube arrays of 30 nm and 80 nm in diameter to optimize the bacterial and osteoblast adhesion on the surface of implant. They showed a reduction in bacterial adhesion and enhancement of C3H10T1/2 cell adhesion, especially for 80 nm TiO₂ nanotube arrays [206]. To avoid bacterial colonization on Ti-implant surface, a coating with nanostructure of Ti was produced by employing the glancing angle deposition (GAD) technique with magnetron sputtering. This work prevented biofilm formation and showed good response for bone formation [207].

Cao *et al.* made TiO₂ coatings containing nanoparticles of silver (Ag NPs) by changing the atomic-scale heating effect of silver plasma immersion ion implantation. They compared different sizes of Ag NPs and this revealed distinctively different characteristics. The larger the Ag NPs (5-25 nm), the more protective they are against bacterial infection and hence the anti-bacterial activity can be controlled by tailoring the size [208].

Qiao *et al.* used Ag-plasma immersion ion-implantation (Ag-PIII) to lower the Ag NPs mobility, which is derived from small sizes of AgNPs and showed that Ag-PIII method can control the release and mobility of Ag-particles leading to increased bone formation around implant surfaces [209]. A dual Zn/Ag implantation into titanium by plasma immersion ion implantation and the resultant micro-galvanic couples has also been shown to decrease corrosion rate and enhance initial adhesion and proliferation, differentiation, osteogenesis activity, and antibacterial ability both *in vitro* and *in vivo* [210]. At the same time, Huang *et al.* looked at the influence of Ca/Ag (1×10^{-17} ions per cm^2) dual-ion implantation on nanograined titanium alloys with nano-grained (NG) and coarse-grained (CG) surfaces and they showed better osteogenic activity and antibacterial properties for NG surfaces [211].

Chitosan is a polysaccharide derived from hard outer skeleton of shellfish like crab, lobster, and shrimp and it has become an interesting antimicrobial compound [212, 213]. Furthermore, chitosan is considered to be an acceptable and satisfactory biopolymer with a wide variety of applications in drug delivery, tissue engineering, gene therapy, and theranostics [214]. Chua *et al.* worked on hyaluronic acid/chitosan (HA/CH) polyelectrolyte multilayers (PEMs) and arginylglycylaspartic acid (RGD) to study the biocompatibility and the consistency of its antibacterial characterisation. They showed promising results indicating that immobilizing RGD-containing peptides on HA/CH PEM-functionalized Ti substrates could increase osteoblast function with steady antibacterial properties [215].

Zheng *et al.* tried to determine bacterial colonization and osteoblast growth simultaneously for antibacterial coatings and immobilized growth factors containing carboxymethyl chitosan (CMC) and BMP-2 along with three types of anchoring molecules (silane, dopamine (DA), and polydopamine (PDA)). Interestingly, they concluded that DA and PDA were more stable than

silane and coupling BMP-2 and CMC together revealed more stable protein adjustment. However, the anchors did not show significant bacterial inhibition, but CMC resulted in 75-80% improved prevention of bacterial colonization in comparison with Pristine-Ti [216]. Zhao *et al.* fabricated polydopamine (PDOP) films as an intermediate layer for post-immobilization of chitosan-lauric acid (Chi-LA) conjugate on Ti implants. According to antibacterial assays against *S. aureus* and *P. aeruginosa*, for Chi-LA modified Ti-substrate, adherence and growth of bacteria was decreased; *in vitro* tests revealed improvement in mineralization capacity of osteoblasts [217].

To release antibiotics constantly and to reduce the risk of after-surgery infection, 0.81 mg/ml ciprofloxacin-loaded chitosan NP coating was made for Ti-implant and successful results were seen [218]. To have the mentioned properties, Ordikhani *et al.* fabricated chitosan coating containing different amounts of vancomycin via cathodic electrophoretic deposition method (EPD) on titanium foils. The coating was non-toxic to MG-63 osteoblast-like cell line and bacteria colonization was reduced by 85%; further *in vitro* electrochemical tests revealed a remarkable reduction in corrosion current density[219]. EPD was adopted to coat the chitosan matrix containing gelatin nanospheres loaded with antibiotics (vancomycin & moxifloxacin) on stainless steel plates and this strategy could be used to control the delivery of antibiotics, hence preventing bacterial infection [220].

Cometa *et al.* investigated the fabrication of chitosan coating loaded with silver to promote biological activity of Ti-implants. They produced antibacterial coating of chitosan and silver through EPD on poly (acrylic acid)-coated Ti-substrates. From MG- 63 osteoblast-like cell cultures and *S. aureus* and *P. aeruginosa* tests, the effective silver amount was determined to be 0.3% and < 0.1 ppm for 7 days and 21 days, respectively [221].

One of the possible solutions to recover from delayed infections which may occur after 3 months and extend to 2 years, can be using antibiotics for prolonged period. Vancomycin is a promising antibiotic to prevent the colonization of *S. aureus* and *Staphylococcus epidermidis* (*S. epidermidis*) on Ti-implants [222-224]. Studies have shown that only Rifampicin and other rifamycinics can provide action against *Staphylococcus*, while other antimicrobial agents have a minimal bactericidal (killing bacteria) concentration (MBC) [225].

Asharani *et al.* worked on Ag-NPs dosage-dependency in human cells and realised that Ag-np could cause harmful effects on mitochondria, decrease ATP (energy currency of body), and increase reactive oxygen species (ROS) [226]. They examined the use of $\sim 0.4 \mu\text{g}/\text{cm}^2$ to $\sim 23.6 \mu\text{g}/\text{cm}^2$ AG-np into a layer-by-layer deposition of polymeric thin films containing poly (allylamine hydrochloride) (PAH) and poly (acrylic acid) (PAA). They found the small amount of $\sim 0.4 \mu\text{g}/\text{cm}^2$ Ag-np was sufficient for the polymeric films to reduce the growth of *S. epidermidis* by 99.9999% and they were not toxic and also stimulated cell attachment and growth [227]. Liu *et al.* evaluated the use of 20-40 nm Ag-np and 17.5% (w/v) poly(DL-lactic-co-glycolic) (PLGA) as a coating for stainless steel alloy (SNPSA) and showed SNPSA could be suitable due to its bactericidal and osteoinductive properties [228].

Managing the Ag-release may result in long-term antimicrobial activity. To address this issue a group of researchers embedded Ag_2O np into titania nanotubes (NT) via anodizing and sputtering. The architecture of the coating facilitated the adequate generation of Ag^+ , which provided longer antibacterial ability as well as positive effects on promoting cell spread [229]. Tilmaciu *et al.* fabricated mercaptodecylphosphonic acid (MDPA) monolayers followed by reaction with AgNO_3 ($\sim 0.65 \text{ n.mol.cm}^{-2}$) and the results showed great inhibition against *E. coli*

and *S. epidermidis* adhesion as well as increased osteoblast numbers [230]. Researchers have also devised coatings composed of three layers: 1000 nm HA as first layer, $1.5 \mu\text{g cm}^{-2}$ Ag-np as the second layer, and 150 or 1000 nm CaP as the third layer which was fabricated via electrophoretic deposition of Ag-np along with radio frequency magnetron sputtering of CaP on titanium. The three-layer coating showed good mechanical stability and adequate antimicrobial effect through semi-quantitative turbidity test for the upper HA layer against *E. coli*. This also showed that the latter property can provide a situation where silver is released slowly [231].

The functionality and biocompatibility of Ag-np strongly depend on size, shape of particle as well as the processing conditions such as pH [232]. There are other ions which possess similar characteristics to Ag in terms of killing bacteria in biomaterial applications. Zinc is one of those materials that can play the same role as Ag [233]. Hu *et al.* doped Zn into TiO₂ coatings by plasma electrolytic oxidation method on titanium. The resultant coatings showed encouraging results for resisting *E. coli* and *S. aureus* and more interestingly, the antibacterial activity was enhanced by increasing the amount of Zn (7.1 ± 0.6 to 9.3 ± 0.8) wt.%. Furthermore, no toxicity was observed, and *in vitro* tests confirmed the cytocompatibility, proliferation, and differentiation of rat bone marrow stem cells [234].

Svensson *et al.* fabricated a new coating consisting of nanosized palladium (Pd), gold (Au), and silver (Ag) (1.20 ± 0.13 , 0.14 ± 0.01 and $1.01 \pm 0.32 \mu\text{g}$, respectively) on Ti-screw for rabbit tibiae and femur. They found out that this combination, not only increased osseointegration but also diminished the need for antibiotics by enhancing the infection-resistance against bacteria [235]. Copper is another alternative which showed beneficial effects in the maturation process of blood vessels and angiogenesis [233]. Julian *et al.* analysed the

incorporation of 1 mol% of CuO and ZnO in silicate bioactive glasses and glass ceramics and the results showed that the addition of Cu and Zn into the bioactive materials can result in bone regeneration, owing to control of bacterial growth and promotion of osteogenesis and angiogenesis [236].

Gallium (Ga) is also promising material in terms of bacterial infection prohibition. 3-D scaffold composites based on Bioglass[®] with high porosity were fabricated by the foam replication method and then coated with sodium crosslinked with Ga³⁺. The results showed that the composite had better mechanical and bioactivity properties and favourable antibacterial effects. Generally, Ga³⁺ has the same size as Fe³⁺ and thus it is hard for microorganisms to make distinction between them; further iron is redox active but Ga is redox inactive and thus infective bacteria cannot clarify between these two elements and consume Ga instead of Fe [43]. Research by Valappil *et al.* showed that doping Ga in phosphate-based glasses could result in good bacterial resistance [237].

Another outstanding material which is being considered is cerium. Ceria (CeO₂) have a wide variety of applications in biomaterial industry, owing to its antioxidant properties which arise from its reversible transformation between Ce(III) and Ce(IV) oxidation states; this increases the likelihood of cell-viability under oxidative stress [44, 45]. Many researchers are trying to investigate the potential of this material for biological applications [238].

Table 2.4. *Bacterial infection challenges and possible solutions* [10]

Challenges	Possible Solutions	Ref.
Primary infection	Implant Surface Engineering	• PLL-g-PEG/PEG-RGD) [200]
		• 0.5 ml BMP-2/ 2mg/ml dextran-grafted surface [201]
		• SIP technique [202]
		• 35% w/v Chitosan hydrogel [203]
		• Anodizing Ti-nanotubular surface in 0.5 vol% [87]
		• NT (anodizing: 0.5 wt% NH ₄ F) - 2 M AgNO ₃ [204]
		• 80 nm TiO ₂ -NT [206]
		• TiO ₂ -NT (GAD technique) [207]
	Bactericidal Surface Engineering	• Tailoring Ag size-scale (5-25 nm) [208]
		• Ag-PIII [209]
		• Zn/Ag Ti-co-implanted [210,
		• Ca/Ag (1×10 ⁻¹⁷ ions per cm ²) on NG & CG Ti-surface 211]
		• HA/CH and RGD [215]
		• CMCS/BMP-2 (Saline, DA, PDA) [216]
		• 1 wt% Chi – 24 ml LA/PDOP [217]
		• 0.81 mg/ml Ciprofloxacin/Chitosan

Challenges	Possible Solutions	Ref.
Delayed infection	<ul style="list-style-type: none"> 0.5 g/L Chitosan/Vancomycin 	[218]
	<ul style="list-style-type: none"> Chitosan/25 ml gelatine/antibiotics 	[219]
	<ul style="list-style-type: none"> Chitosan/ < 0.1 ppm silver 	[220]
		[221]
	Prolonged Usage of Antibiotic <ul style="list-style-type: none"> Vancomycin Rifampicin 	[222-224] [225]
	Antimicrobial-Realising Control <ul style="list-style-type: none"> 0.4 µg/cm² Ag-np 20-40 nm Ag-np / 17.5 w/v PLGA Ag-np/NT (Anodizing: 0.3 wt.% NH₄F) (~ 0.65 mol/Cm²) AgNO₃/MDPA 1000 nm HA/ 1.5 µg/Cm² Ag-np/1000 nm CaP 	[226] [228, 229] [230] [231]
	Alternatives to Silver <ul style="list-style-type: none"> (7.1±0.6 and 9.3±0.8) wt% Zn (1.20 ± 0.13 µg) Pd / (0.14 ± 0.01) µg Au / (1.01 ± 0.32) µg Ag 1 mol% Cu/ 1 mol% Zn 600 mM Ga 194.8 µg/ml Ce 	[234] [235] [236] [43] [45]

In brief, one of the key strategies against infection is to increase bioactivity through surface modification is the enhancement of the antibacterial characteristics [28, 29] and the effectiveness of cell attachment to the implant [30, 31]. To these ends, different techniques for physical and chemical surface modification for reduction of the affinity of bacteria to adhere and develop biofilms on implant surfaces have been examined [28]. These antibacterial approaches include anti-adhesive coatings [239], bactericidal coatings [32], and altered surface topographies (to expose nanowires [33], nanotubes [34], or cicada wings [35]). The cell-attachment approaches include calcium phosphate coatings [36], biomolecular coatings [37], and engineered surface topographies [38].

Of the physical and chemical strategies used for surface modification [240], the former include physical vapour deposition (PVD) [241], plasma spraying, and plasma immersion ion implantation and deposition (PIII&D) [242, 243] and the latter includes chemical vapour deposition (CVD) and sol-gel [17]. The sol-gel method is used commonly because it offers the advantages of compositional variability owing to the use of a precursor solution, room-temperature and atmospheric-pressure fabrication, simplicity of the process, high speed, and low cost [244].

There also are strategies to combine the hindrance of bacterial infection and the enhancement of osseointegration. These include the insertion of therapeutic ions [39-45] into resorbable metallic alloys [46], resorbable bioceramics [245], and resorbable biomolecules [47] as well as doping of the surfaces by methods such as diffusion [246] and ion implantation [48]. Relevant information about these therapeutic ions is summarised in **Table 2.5**.

Table 2.5. Summary of some therapeutic ions and their biological functions

<i>Ion</i>	<i>FDA- Approved^a</i>	<i>FDA Established Pharmacologic Class (EPC)</i>	<i>Function</i>	<i>Ref.</i>
Ti	✓	Food, drugs, cosmetics, metal containing implant	Enhancement of osteoblast attachment and bone regeneration	[247-249]
			Bactericidal effect against <i>S. aureus</i> and <i>Porphyromonas gingivalis</i> (<i>P. gingivalis</i>)	[250, 251]
Ca	✓	Phosphate binder, blood coagulation factor	Regulation of proliferation and differentiation of osteoblasts and bone mesenchymal stem cells (bMSCs)	[252]
			Enhancement of osteogenic properties	[253]
Mg	✓	Osmotic laxative, urinary calculi dissolution agent	Regulation of Ca and Na ion channels	[254]
			Improvement of cell adhesion and stability	[255]
Ag	✓	Sulphonamide antibacterial	Antibacterial activity against <i>E. coli</i> , <i>S. aureus</i> , and <i>Pseudomonas aeruginosa</i> (<i>P. aeruginosa</i>)	[256]
			Cyto-protection and anti-inflammation	[257]
Zn	✓	Copper absorption inhibitor	Stimulation of bone formation and decrease in bone resorption	[258]
			Antibacterial activity against <i>S. aureus</i>	[259]
Ce	✓	Treatment for Parkinson's disease	Improvement of osteoblast differentiation	[260-262]
			Antibacterial and anti-inflammatory capabilities	[263-265]

Ga	✓	Radioactive diagnostic agent, calcium resorption inhibitor	Selective osteoblast/osteoclast activity	[93, 266]
			Antibacterial activity against <i>E. coli</i> and <i>S. aureus</i>	[267, 268]
Mn	✓	Paramagnetic contrast agent	Promotion of adhesion, proliferation, differentiation, and mineralisation of osteoblasts	[269, 270]
			Antibacterial activity against <i>E. coli</i> and <i>Bacillus cereus</i> (<i>B. cereus</i>)	[271, 272]

^a According to US Food and Drug Administration (FDA) established pharmacologic class (EPC)

In relation to the present work, Ce^{3+} , Ga^{3+} , Mn^{2+} ions have been shown to minimise bacterial growth while stimulating osseointegration [49-54]. All of these ions incorporated in oxide nanoparticles have been shown to exhibit minimising effects against *S. aureus* and *E. coli* while increasing the osseointegration, thereby suggesting their potential for *in vivo* applications as multifunctional coatings.

Dopants in CeO_2

Ga^{3+} : It has been reported that Ga^{3+} exhibited bactericidal activity upon substituting for biological Fe^{3+} , which plays a key role in a microorganism's metabolic processes, including respiration, oxygen transport, DNA regulation, and survival of bacteria [273]. The similar sixfold-coordinated valences of Fe^{3+} and Ga^{3+} ($\text{Ga}^{3+} = 0.62 \text{ nm}$; $\text{Fe}^{3+} (\text{HS}) = 0.645 \text{ nm}$ [274], where the high spin (HS) configuration is likely [275]) suggest ready substitution and so allows Ga^{3+} to act as a Trojan horse [276]. Ga^{3+} has been reported to have osteoblastic and antibacterial properties [277, 278]. Ga^{3+} has been reported to attack both *E. coli* and *S. aureus* in burn wound infections [279] [280]. Ga^{3+} has been reported to accelerate early osteoblastic differentiation but also to interrupt albeit as an adsorbed salt rather than a solid solute [281]. Further, *in vivo* studies showed that gallium nitrate exhibited the unique capability of reducing the osteocalcin mRNA levels without affecting other involved mRNAs [282]. Ga^{3+} also is FDA-approved as a drug component for the treatment of diseases resulting from hypercalcemia cancers (*e.g.*, Paget's disease) and infectious diseases (*e.g.*, acute atopic dermatitis) [277, 278].

Mn^{2+} : Mn^{2+} is a trace mineral that is vital to human physiology in the activation of metabolic enzymes involved in electron-transfer reactions, anti-oxidant behaviour, and regulation of cellular processes. Mn^{2+} has been detected in the human brain, liver, and hair [283, 284]. It has been reported that incorporation of 9 mol% Mn in CeO_2 enhanced the bactericidal activity by 40% and

46% against *S. aureus* and *E. coli*, respectively [285]. The bactericidal activity of Mn has been reported to result from the formation of ROS at the NP surfaces. Mesaros *et al.* [271] reported that interstitial solid solubility of Mn^{2+} in ZnO and the associated electronic charge compensation resulted in enhanced antibacterial activity, presumably through the generation of hydroxyl radicals. Mn^{2+} also has been shown to have promising effects on implant bone in-growth the strong affinity with extracellular matrix proteins [286]. *In vivo* studies suggested that Mn^{2+} can increase the bone mineral density through the acceleration of the bone formation process [97]. Mn^{2+} also has been shown to preserve the rigidity of bone connective tissue, the deficiency of which would result in adverse effects on carbohydrate, glucose, and lipid metabolisms [287].

Figure 2.4 summarises the potential biological responses to the relevant ions Ti, Ce, Ga, and Mn. Ti has been observed to favour osteoblast attachment, differentiation, and hence bone regeneration; it also has exhibited minimisation of bacterial growth [247-251]. Ce is known to regulate the proliferation and differentiation of osteoblasts as well as promote hydroxyapatite (HA) precipitation [260-262, 288]. Like Ti, Ce is a catalyst that can inhibit bacterial proliferation; Ce also exhibits anti-inflammatory capabilities [263-265]. Ga has been reported to show antibacterial activity as well as osteoblast proliferation and osteoclast minimisation capabilities [93, 266-268]. In common with the other ions, Mn is a biologically active ion and it can enhance osteoblast adhesion, differentiation, and mineralisation as well as provide antibacterial properties [269-272]. While the present work confirms the bioactivities of these ions, it also reveals that Ga enhances hydroxyapatite precipitation upon exposure to SBF and Mn has the capacity to kill both *S. aureus* and *E. coli*.

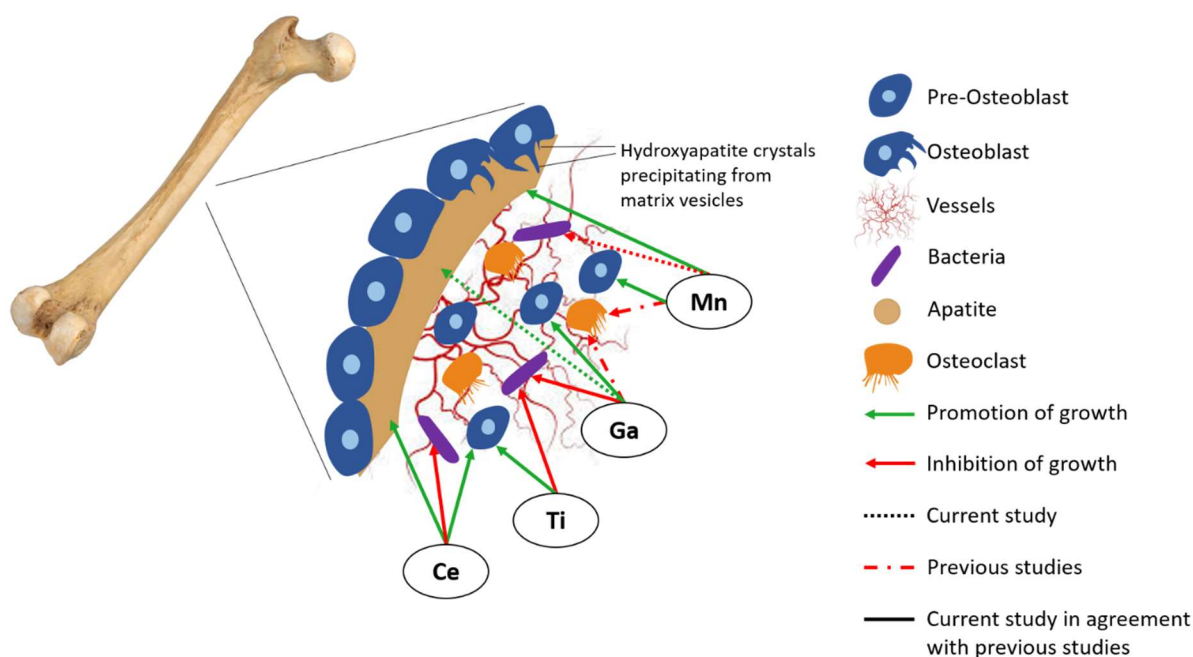
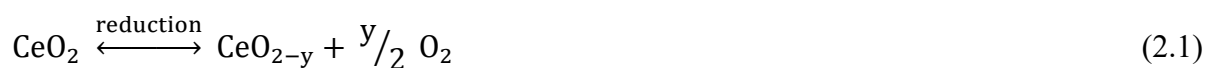


Figure 2.4 Schematic of biological responses to bioactive ions [289, 290]

2.4 Properties of Ceria

CeO₂ is widely used in the medical industry. The reversible switching between Ce(III) ↔ Ce(IV) and the resultant defect structure allow nanoceria to provide protection against reactive oxygen species (ROS) [238, 291]. Catalysis [292], corrosion prevention [293], photoenergy [294], electrochemical cells [295], biomaterials [296], thermal barrier [297], chemical mechanical planarization [298], microelectronics [299], glass abrasives [300], optical devices [301], and UV-absorbers [302] are some of applications of cerium oxides.



Ceria has been widely used in cancer therapy [303]; cerium oxide nanoparticles (CNPs) were found to prevent cancer cell migration in gastric cancer, which was responsible for nearly 700,000 deaths in 2012 [304]. In another study, porous ceria nanorods have been investigated to act as a biomarker of breast cancer and provide beneficial results due to higher surface area and chemical and catalytic

stability under severe conditions [305]. Ovarian and colon cancer were two other tumour-induced oxidative stress models for which nanoceria (NC) has been considered. The uptake and intracellular localisation of NC in both cell lines were dependent on the endocytosis mechanism and diameter of NC, which at 7 nm revealed better control over cell proliferation of colon and ovarian cancer cells [291, 306].

Fighting against bone cancer cells was another capability of CNPs coated with 0.01 M dextran [307]. Researchers found out cytotoxicity of NC was highly time- and dosage-dependent and at higher oxidative stresses, increased lipid peroxidation and cell membrane damage would result [50]. Another study proved the biocompatibility and prevention of antifilm formation characteristics of ceria and this was done by stabilizing zirconia-based ceramic with ceria; both *in vitro* and *in vivo* tests demonstrated the clinical potential of this matrix to be used as implant material [308].

2.4.1 Non-Biological Applications of Ceria

Ceria (CeO_2) has a fluorite crystal structure with cations in face-centred cubic unit cells and anions in octahedral interstitial sites (cerium cations coordinated by eight-nearest oxygens as anions) (Table 2.6). When doping occurred, and a cerium cation (Ce^{4+}) is replaced with the dopant substitutionally, the lattice oxygen atoms are removed in order to keep the lattice electrically neutral, which leads to the formation of oxygen vacancies [309, 310].

Table 2.6 lists some of the non-biological applications of ceria. Murugan *et al.* utilized 3wt% Mg, Ca, Sr, and Ba as dopants for 0.1 M ceria nanostructures through hydrothermal techniques and the photocatalytic activity of samples was measured by aqueous solution of methylene blue (MB) dye. It was noted that alkaline metal ions in comparison with pure samples showed higher activity for photodegradation of MB [311]. Utilizing suspended graphene oxide (GO) modified by Hummers

method [312] resulted in better separation of electrons and holes owing to GO light absorbency [313]. Yavo *et al.* doped 10 mol% of Gd in ceria by co-precipitation technique to study the electromechanical properties. They found that the electrorestrictive property of the sample could be changed by altering charge trapping or voltage distribution at the grain boundaries [314]. Indium addition into Gd-doped ceria (0.5, 1, 1.5, 2 and 5 at% in GDC) helped to increase migration energy of the grain interior of the reduction in the median dopant size and down regulation of the dissolution energy of grain interior [315],[316]. Wattanathana *et al.* evaluated doping of samarium (Sm) through metal triethanolamine complex decomposition technique into ceria (SDC). The conductivity of the samples was monitored by impedance spectroscopy and 15 mol% of Sm showed excellent conductivity[317].

Co-doping aluminium (Al) and rhodium (Rh) in to ceria for water gas shift reaction (WGS) and CO oxidation via single step solution combustion, resulted in greater catalytic performance [318]. Mandapaka *et al.* co-doped 5 at% Zn and 2 at% platinum (Pt) in ceria by combustion synthesis method for WGS and CO oxidation [319]. Incorporating 1-2 mol% ceria in anatase TiO₂, with the aim of supporting material for platinum (Pt) in catalytic combustion of methanol in low temperature and catalytic tests revealed great stability of ceria-TiO₂/Pt [320]. Huang *et al.* added Mn in to ceria via sol-gel method and tested catalytic activity for soot oxidation capacity of diesel engines and they concluded that by 50% Mn-content, ignition and peak temperature decreasing and lattice defects increased [321].

Table 2.6. *Non biological applications of ceria*

<i>Dopants</i>	<i>Method</i>	<i>Applications</i>	<i>Ref</i>
3 wt% Mg²⁺, Ca²⁺, Sr²⁺, Ba²⁺	Hydrothermal method	Photocatalyst	[311]
Graphene Oxide	Hummers method & Hydrothermal	Photocatalyst	[313]

10 mol% Gd	Co-precipitation	Electrostriction	[314]
1 at% In	Cold isostatic pressing	Fuel cells	[315]
15 mol% Sm³⁺	Thermal decomposition	Fuel cells	[317]
5 at% Al, 2 at% Rh	Solution combustion synthesis	Catalyst	[318]
5 at% Zn, 2 at% Pt	Solution combustion synthesis	Catalyst	[319]
1-2 mol% CeO₂ TiO₂	Evaporation-induced self-assembly	Catalyst	[320]
50 at% Mn	Sol-gel	Catalyst	[321]

2.4.2 Biological Applications of Ceria

Ceria also shows favourable biological performance (**Table 2.7**). Yabe *et al.* doped different metal ions with soft solution chemical method into ceria, including Mg²⁺, Ca²⁺, Sr²⁺, Ba²⁺, Y³⁺, La³⁺, Nd³⁺, Sm³⁺, Eu³⁺, Tb³⁺ to evaluate catalytic activity in sunscreen. Doping of 20 mol% Ca²⁺ in 0.8 M ceria resulted in decreased particle sizes of 2-4 nm and significant activity in visible light [322]. Zn²⁺ doped ceria (Ce_{1-x}Zn_xO₂, x= 0.01, 0.03, and 0.05) was fabricated and the resultant cytotoxicity analysis by MTT assay (cell metabolic activity assessment) revealed that cytotoxicity was Zn-dosage dependent with the best performance seen in samples with <3% Zn [323].

Doping ceria (10 and 30 wt%) in hydroxyapatite via ball milling followed by calcination at 1300°C for 1 h showed that the higher the amount of ceria (30 wt%), the greater the osteogenic activity [324]. Yuan *et al.* focused on doping different mol% (0.5, 1, 2 mol%) ceria in hydroxyapatite and polylactic acid (HA/PLA) and a uniform and dense coating with good thermal resistance were obtained. The addition of PLA had a positive effect on preventing HA from decomposing [325]. Doping 10 and 30 wt% of ceria in calcium silicate coatings (CS) was done through solid-state reaction and this was then applied on Ti-6Al-4V with atmosphere plasma spraying (APS); the coating showed better chemical stability and an increase in osteogenic properties [326].

Incorporating ZnO and CuO into ceria to form 4.2 nm crystallite ZnO-CuO-CeO₂ with the rapid and easy technique of chemical precipitation, contributed to reasonable electrochemical behaviours and antibacterial activity; however, it showed more resistance against gram-negative bacteria (*E. coli*) than gram-positive bacteria (*S. aureus*) [327]. To produce anti-oxidant activity and to improve physical strength, Clark *et al.* doped titanium in ceria and (CeTiO₂) reached a nano-sized composite (15-20 nm) and the results indicated that nano-CeTiO₂ reduced the amount of hydrogen peroxide, which triggered the cell damage, and hence it may be a good candidate in treating diseases like Alzheimer [328]. Gionco *et al.* added cerium into ZrO₂, to prepare a matrix with photosensitive property to visible light which allowed photons with low energy to transfer between bands [329].

Table 2.7. *Biological applications of ceria*

<i>Medium</i>	<i>Method</i>	<i>Applications</i>	<i>Ref.</i>
20 mol% Ca²⁺	Chemical solution method	UV filter	[322]
3 wt% Zn²⁺	Sol-gel	Biomedical	[323]
30 wt% CeO₂ in HA	Plasma spray	Orthopaedic implant coating	[324]
2 mol% in HA/PLA	Chemical precipitation	Implant coating	[325]
30 wt% CeO₂ in CS	Solid-state reaction	Orthopaedic implant coating	[326]
0.2 M ZnO-CuO	Chemical precipitation	Biomedical	[327]
12.5 at% Ti	Flame spray pyrolysis	Drug delivery	[328]
0.5 mol% CeO₂ in Zr	Sol-gel	Photocatalyst	[329]

2.4.2.1 CeO₂ Surface Coating

CeO₂ or ceria has emerged as a key biocatalytic material for a range of reasons [330, 331]. Despite these advantages, its applicability of a surface coating has not been explored extensively. However,

since such coatings generally require heat treatment in order to effect bonding to the substrate, thermal expansion (α) mismatch can lead to residual stresses that can accelerate coating deterioration or cause immediate failure upon cooling. Upon successful fabrication of a CeO_2 coating, it provides the capacity to introduce or enhance the antibacterial activity through the action of the constituent ceria nanoparticles (CeNPs) against gram-positive and gram-negative pathogens. However, the nature of the synthesis, the exposure conditions, and the type of pathogen affect the performance of ceria against bacteria. The key materials variables that can be engineered to improve the performance are as follows [332-347]:

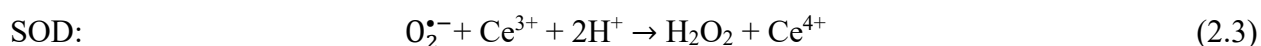
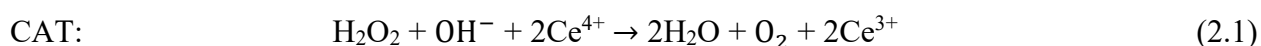
- **Ce Concentration:** Increasing the concentration of CeNPs decreases bacterial growth, regardless of which gram-reaction occurs, although CeNPs are more efficient in killing gram-negative than gram-positive bacteria.
- **$\text{Ce}^{3+}/\text{Ce}^{4+}$ Ratio:** The antibacterial activity of CeNPs increases with increasing $\text{Ce}^{3+}/\text{Ce}^{4+}$ ratio owing to the ready $\text{Ce}^{4+} \rightarrow \text{Ce}^{3+}$ reduction, resultant charge-compensating oxygen vacancy ($\text{V}_\text{O}^{\bullet\bullet}$) formation through the reaction $2\text{Ce}^{4+} \rightarrow 2\text{Ce}^{3+} + \text{V}_\text{O}^{\bullet\bullet}$, and associated generation of pro-oxidant reactive oxygen species (ROS), which kill bacteria. Increased $[\text{V}_\text{O}^{\bullet\bullet}]$ is known to result in superior antioxidant behaviour of CeNPs.
- **pH:** Alteration of the pH alters the CeNP surface charge and hence the affinity of pathogens to adsorb. The healthy physiological environment exhibits a slightly basic pH of 7.4 while diseased environments tend to be slightly acidic, with a pH range of 6.2-6.8. As the $\text{Ce}^{4+} \leftrightarrow \text{Ce}^{3+}$ redox switching occurs readily upon change in pH, the physiological environment favours a high Ce^{3+} concentration ($[\text{Ce}^{3+}]$) while diseased environments favour high Ce^{4+} concentration ($[\text{Ce}^{4+}]$). This suggests that the antibacterial activity against gram-positive bacteria would be greater than that of gram-negative bacteria in the physiological environment.

- **Surface Area:** The efficiency of the antibacterial performance CeNPs is increased with increasing surface areas and associated high $[Ce^{3+}]$ and $V_O^{\bullet\bullet}$ concentration ($[V_O^{\bullet\bullet}]$) through latter's role as an active catalytic site for ROS formation.
- **Size:** The size of CeNPs is important in that smaller NPs have greater surface area to volume ratios, which effectively increase the surface energies and hence reactivities. This effect also facilitates the agglomeration of NPs, which increases the effective particle size and may decrease the effective roughness. CeNPs in the size range 15-40 nm exhibited increasing gram-positive antibacterial activity with decreasing size while gram-negative bacteria showed converse behaviour.
- **Roughness:** The nature of the surfaces of CeNPs can play a significant role in affecting the reactivity against bacteria owing to the greater affinity of cells to attach to rough rather than smooth surfaces. Increasing roughness also increases the surface area.
- **Shape:** While all three of the principal euhedral forms of CeNPs (octahedral, cubic, rod-like) exhibit enhanced antibacterial activities, the octahedral morphology generally is observed to be of much smaller dimensions and higher $[Ce^{3+}]$ than the other two morphologies. However, the implication of superior antibacterial performance of octahedra is mitigated by the fact that the exposed planes are the most stable and they are nonpolar, which suggests a reduced tendency of bacteria to adsorb on these surfaces.
- **Surface Charge:** The surface charge, which is assessed in terms of the zeta potential, can alter the biological response (cellular uptake and protein adsorption) to CeNPs by bacteria owing to the electrostatic interaction between the CeNPs and the cell wall. Since the zeta potential is altered by both pH and the change distribution of adsorbed species, then both factors are important. Hence, the dominant role of the latter is indicated by the counter-intuitive observation that gram-negative *E. coli* exhibited greater attraction to CeNPs in

phosphate-buffered saline (PBS) at pH 7.4 (with higher $[\text{Ce}^{3+}]$ – less positive/more negative) than normal saline (NS) at pH 5.5 (with higher $[\text{Ce}^{4+}]$ – more positive/less negative).

2.4.2.2 Mechanism of ROS Generation

ROS are generated through both non-biological and biological processes. In the former, catalysts facilitate the formation of charge carriers (*viz.*, electrons and holes) [348], which interact with proximal oxygen and water to form four major ROS, which is superoxide ($\text{O}_2^{\bullet-}$), hydroxyl (OH^{\bullet}), singlet oxygen ($^1\text{O}_2$), and hydrogen peroxide (H_2O_2) [349]. In the latter, cyclic ROS production and scavenging are based on the rapid and reversible switching of the $\text{Ce}^{3+} \leftrightarrow \text{Ce}^{4+}$ redox couple [340] and the respective formation \leftrightarrow annihilation of $\text{V}_\text{O}^{\bullet\bullet}$, which confer CeNPs with autoregenerative antioxidant characteristics involving (a) a catalase (CAT) biomimetic reaction, where H_2O_2 is decomposed to H_2O and O_2 by $\text{Ce}^{4+} \rightarrow \text{Ce}^{3+}$ reduction and (2) a superoxide dismutase (SOD) biomimetic reaction, where $\text{O}_2^{\bullet-}$ is reduced to a peroxide group by reverse $\text{Ce}^{3+} \rightarrow \text{Ce}^{4+}$ oxidation [350].



2.5 Anti-Microbial and Bioactivity Applications of Ceria

2.5.1 Bacterial Infection Inhibition

Mechanism of Bacterial Death: There are two mechanisms by which CeNPs affect microorganisms [332, 351, 352]. The first is through penetration of the cell wall and internalisation. This results in cytotoxicity to the lysosome owing to ROS-induced oxidative stress and the consequent release of inflammatory cytokines [332, 353, 354]. The second is surface contact, which results in the

destruction of the bacteria during the stages of (1) cell wall disruption; (2) oxidative stress from the generation of ROS; (3) chemical degradation of bacterial DNA, RNA, and proteins; (4) and dysregulation of nutrient transport [355, 356].

A further consideration is the potential for limited Ce solubility through dissolution and/or the detachment of CeO₂ nanofragments. When Ce is released, it can interfere with bacterial respiration and electron flow [333], followed by reaction with thiol (-SH) groups or adsorption on transporters and resultant hindrance of nutrient transportation [263, 357]. The Ce⁴⁺ → Ce³⁺ reduction and consequent ROS generation can dysregulate the function of biological molecules by attacking nucleic acids, proteins, polysaccharides, and lipids, thereby killing bacteria [358, 359]. The final stage is the hydrolysis of DNA oligomers by Ce⁴⁺, which interrupt protective biofilm formation [360].

Antoine *et al.* evaluated the effects of CNPs on Gram-negative bacteria (*E. coli*) and they concluded that the increased percentages of NPs can lead to lower percentage of bacteria colony forming units (CFU) [361]. Wang *et al.* justified the capability of CNPs to fight against bacteria as the unique property of forming reactive oxygen species (ROS) [362]. Xiao *et al.* investigated the effects of CNPs on prevention of proliferation and differentiation of gastric cancer cells and found CNPs are a suitable candidate for cancer treatment and more interestingly, *in vivo* tests revealed antibacterial activity of CNPs [304].

Doping of bioactive glass (BG) with ceria can affect bacterial activity. Goh *et al.* produced BG with different percentages of ceria via sol-gel method, and obtained outstanding results indicating that adding 5 or 10 mol% of ceria can provide antibacterial properties while maintaining bioactivity [330]. Kasinathan *et al.* doped ceria in TiO₂ and the results showed good activity; moreover

bacterial inhibition was confirmed as being ceria-dose dependent against gram-positive and gram-negative microbial strains [363]. Surendra *et al.* synthesized nanoparticles of ceria (CNPs) via *Moringa oleifera* peel extract method and tested photocatalytic activity with crystal violet dye as well as antibacterial activity and they showed that CNPs had antibacterial properties against *E. coli* and [364].

2.5.2 Promoting Bone Formation

Ceria nanoparticles have shown attractive effects on the proliferation, differentiation and mineralization of primary osteoblasts [365]. Salinas *et al.* introduced doped Ce_2O_3 , Ga_2O_3 and ZnO into ordered mesoporous bioactive 80% SiO_2 -15% CaO -5% P_2O_5 glass as an interesting bioactive scaffold owing to its stability in textural properties (porosity and surface area) and apatite-like forming ability [366]. Zhang *et al.* incorporated ceria in mesoporous calcium-silicate (CeO_2 -MCS) along with triblock copolymer (P123) as a structure-directing (pore former), to investigate the drug delivery capability for bone regeneration. The results showed that adding ceria into the mesoporous calcium-silicate (MCS) induced the proliferation and alkaline phosphate activity (ALP) of osteoblast-like MC3T3-E1 cells and at the same time maintained mesoporous structure [367]. Ying *et al.* also revealed the importance of Ce-dosage by comparing different concentrations of Ce and concluded that lower percentage of Ce (0.001 μm) increased bone marrow stromal cells (BMSCs) and ALP activity [368]. Jordan *et al.* found the porous ceria foam like Bioglass is a good candidate for orthopaedic tissue engineering [369]. CNPs unlike other NPs are not toxic but are size-sensitive for use in nerve cell protection [44]. Utilizing nanoceria (3-5 nm) as a osteogenic supplement in 3-D nanocomposite bioactive glass scaffold increased the production of collagen by human mesenchymal stem cells (HMSCs) and this enhanced osteoblast proliferation without any toxic effects [51].

Table 2.8 summarises some of the key properties of cortical bone, the Ti6Al4V biomedical titanium substrate, and the CeO₂ coatings, which are the subject of the present work.

Table 2.8. *Comparison of mechanical properties of cortical bone, Ti6Al4V, and CeO₂ [61, 370-383]*

<i>Mechanical Property</i>	<i>Cortical Bone</i>	<i>Commercial Ti6Al4V</i>	<i>3D Printed Ti6Al4V</i>	<i>Bulk CeO₂</i>	<i>Thin Film CeO₂</i>
Young's Modulus, E (GPa)	11 – 21	55 – 110	110 ± 7	227 ± 10	17 – 25
Tensile¹/Yield² Strength (MPa)	140 ± 19 ¹	850 – 900 ²	1030 ± 70 ²	300 ± 10 ¹	91 – 100 ¹
Vickers Microhardness (H_v)	123 ± 42	349	400 – 430	1100 – 1200	22 ± 20 ^a

^a Converted from Berkovich nanoindentation data [384]

3. Material Preparation and Characterization

3.1 Materials

CeO₂ (ceria) was used as the coating material since it is considered to be an advantageous biomaterial [44, 45, 50, 238, 385, 386]. In order to optimise the ceria-based coating for the generation of new bone and the inhibition of bacterial colonisation, gallium (Ga³⁺) and manganese (Mn²⁺) were used as dopants at different levels (5-9 mol%) using the sol-gel method. Since osteoblast proliferation and maturation are highly dependent on the quality of the implant surface, especially the roughness, which plays a significant role in cell adherence [387, 388], a standardised surface in the form of 3D printed Ti6Al4V (average roughness R_a = 15 µm) was used. The CeO₂ sol-gel coating then was applied by spin coating and subsequent recrystallisation by annealing at 650°C for 2 h.

3.2 Material Characterization

3.2.1 Compositional and structural

- *3D Laser Scanning Confocal Microscopy*
 - Topography and roughness
- *X-ray Diffraction (XRD)*
 - Crystalline structure and composition
- *Focused ion beam (FIB)*
 - Grain distribution and thickness
- *X-Ray Photoelectron Spectroscopy (XPS)*
 - Surface composition

3.2.2 Biological Tests (*in vitro*)

- *Simulated Body Fluid (SBF)*
 - Apatite forming layer ability

- *MTS Cytotoxicity Assay*
 - Cytotoxicity and cellular proliferation
- *Bacterial Performance*
 - *Staphylococcus aureus* (*S. aureus*) S38
 - *Escherichia coli* (*E. coli*) SK12

3.3 Sample preparation

Samples were 3D-printed Ti6Al4V sheets, of 1 cm × 1 cm size (Advanced Manufacturing Services, Australia), with an Ra roughness of $\sim 16 \pm 0.2 \mu\text{m}$. Prior to coating application, each substrate was cleaned ultrasonically for 1 h each sequentially in acetone and ethanol, followed by rapid drying in flowing N₂. The precursor solution for the CeO₂ thin films was prepared by dissolving cerium nitrate hexahydrate (Ce(NO₃)₃·6H₂O, 99.99 wt% trace metal basis, Sigma-Aldrich, Australia) in isopropanol (Reagent Plus, 99 wt%, Sigma-Aldrich, Australia) to obtain 1 M concentration (43.422 g of Ce(NO₃)₃·6H₂O was dissolved in 100 mL of isopropanol) by magnetic stirring for 2 h in a Pyrex beaker. Dopant salts Mn(NO₃)₂·4H₂O (98 wt%, Sigma-Aldrich) and Ga(NO₃)₃·9H₂O (99.9 wt%, Sigma-Aldrich, Australia) was used at the concentrations of 0.00, 1.00, 5.00, and 9.00 mol% (metal basis). Each solution was stirred magnetically for 2 h in a Pyrex beaker. Spin coating (Laurell Technologies, WS-65052, USA) was carried out by deposition of 0.2 mL (~ten drops) of each solution onto a substrate while spinning at 2000 rpm, followed by drying by spinning for ~10 sec and then placing on a hot plate at preheated to 50°C for 15 min. These processes were repeated nine additional times for a total of ten coatings, which resulted in the fabrication of continuous coatings without macroscopic crack formation. Following these procedures, all of the samples were placed simultaneously on a high-Al₂O₃ firebrick and calcined in a muffle furnace at 650°C for 2 h (heating rate of 1°C/min; natural cooling).

3.4 Characterisation

3.4.1 Microstructure and Mineralogical Properties

3.4.1.1 Scanning Electron Microscopy (SEM)

Scanning electron microscopy (SEM: FEI Nova NanoSEM 450) was performed to assess the morphology and microstructure of the films. To increase the conductivity samples were sputter-coated with carbon (DCT Nano-Structured Coatings) prior to SEM analysis. Following are the experimental parameters:

- Detector: Trough lens detector (TLD)
- High Voltage: 5 kV
- Spot size: 3
- Lens mode: Immersion
- Working distance: 5 mm

3.4.1.2 Transmission Electron Microscopy (TEM)

Transmission electron microscopy (JEOL TEM-1400) was use used to obtain high resolution of cross section of Ce-coating thickness. The operating parameters are as follows:

- Beam current: 55 μ A
- HT voltage: 100 kV
- Electron source: Field emission gun

3.4.1.3 X-Ray Diffraction (XRD)

Ceria crystallinity and phases were determined by x-ray diffraction (PANalytical Xpert Multipurpose X-ray Diffraction System). The experimental parameters are as follows:

- Divergent slit: 1/8°
- Scanning range (2 θ): 20°-100°

- Step size (2θ): 0.026°
- Time per step: 197 s
- Scanning speed: $0.033^\circ/\text{s}$

3.4.1.4 Focused Ion Beam (FIB) Milling

The thickness and the integrity of the coating were analysed by focused ion beam milling (FIB; FEI Nova 200 dual beam focused ion beam system, Ga source, fine-beam current 100 pA).

3.4.1.6 X-Ray Photoelectron Spectroscopy (XPS)

The chemical composition was analysed using X-ray photoelectron spectroscopy (Thermo Scientific ESCALAB250Xi). The operating parameters are as follows:

- Power: 120W (13.8 kV x 8.7 mA)
- Spot Size: 500 μm
- Photoelectron take-off angle: 90°
- Pass energy (survey scans): 100 eV
- Pass energy (region scans): 20 eV

3.4.1.7 Laser Raman Microspectroscopy

Laser Raman microspectroscopy (Renishaw inVia laser Raman Microscope with 514 nm argon ion laser) was used to identify the phases of CeO_2 thin films. The operating parameters are as follows:

- Laser wavelength: 514.5 nm
- Laser working power: 25 mW
- Grating: 2400 lines/mm
- Objective lens: 50x
- Laser spot size: 1.5 μm

- Exposure time: 1 time/s
- Scanning range: 100-800 Raman shift/cm

3.4.1.8 Inductively Coupled Plasma Optical Emission Spectroscopy (ICP-OES)

The ionic concentrations of the Ce, Ga, Mn, Ca, and PO₄ ions after immersion in the SBF solution were determined by inductively coupled plasma optical emission spectroscopy (ICP-OES, PerkinElmer Optima, USA).

3.4.2 Biological Analysis

3.4.2.1 Bioactivity Test

Immersion of bioactive surface in SBF is one way to examine the HA formation ability of the surface *in vitro*. In this project, the SBF solution was made based on Kokubo's instruction [389, 390], which involves the dissolution (in order) in distilled water of NaCl, NaHCO₃, KCl, K₂HP₄·3H₂O, MgCl₂·6H₂O, 1M HCl, CaCl₂, Na₂SO₄, and Tris + 1M HCl. The ionic concentrations of the SBF compared with those of human blood plasma are given in **Table 3.1**. The samples were sterilised by autoclaving, dip-cleaned in ethanol, washed in triplicate by spray (pipette) washing with 1 M PBS, and immersed in SBF solution. CeO₂, Ga-doped CeO₂, and Mn-doped CeO₂ coatings as well as a bioactive glass material (Bioactive Bone Graft Unigraft, USA) as positive control were placed in individual polypropylene containers containing 150 mL SBF solution. Each container was incubated at 37°C and removed at the time point of 2 weeks (15 days) or 1 month (30 days). The samples subsequently were examined by field emission scanning electron microscopy and glancing-angle X-ray diffraction; the solutions analysed by inductively coupled plasma optical emission spectroscopy (ICP-OES, PerkinElmer Optima, USA).

Table 3.1. *Comparison of ionic concentrations in blood plasma and prepared SBF*

<i>Species</i>	<i>Ion Concentrations (mmol/L)</i>	
	<i>Blood Plasma</i>	<i>Prepared SBF</i>
Ca²⁺	2.5	2.1
HPO₄²⁻	1.0	0.9
Na⁺	142.0	141.3
Cl⁻	148.8	148.1
Mg²⁺	1.5	1.5
K⁺	5.0	5.1
SO₄²⁻	0.5	0.5
HCO₃⁻	4.2	4.1

3.4.2.2 Antibacterial Performance

Since counting colony forming units (CFU) is a common method for the measurement of the extent of bacterial growth [29], then colonies of *S. aureus* strain 38 and *E. coli* strain K12 were grown separately on nutrient agar (1000 mL of milli Q water added to CM003 Nutrient Agar, OXOID, UK) by incubating at 37°C under 5% CO₂ for 18 h. Multiple colonies then were transferred to 10 mL tryptone broth medium (TSB, OXOID, UK) and incubated for 24 h. The bacteria were collected by centrifuging (5000 g for 10 minutes), washed two times with 1 M phosphate buffered saline (PBS, Thermo Fisher Scientific, UK), and pipetted into 40 mL of fresh TSB. In order to adjust the optical density (OD) to 0.1 of the TSB suspension at 660 nm, which is equivalent to 10⁸ colony forming units per mL of suspension (CFU/mL), the nutrient agar was cultured and then serially diluted to ensure the correct number of the colonies [391]. The samples were autoclaved, rinsed with ethanol, and washed thoroughly with 1 M PBS before seeding. Following this, 4 mL of the adjusted TSB containing *S. aureus* or *E. coli* was pipetted into each well of a 6-well plate containing the sample and orbitally shaken (120 rpm) in the incubator for 24 h. The media were removed by

pipetting and the residue of each well was rinsed twice with PBS to remove non-adherent bacteria. Each sample was placed in a sterile lidded plastic tube containing 2 mL of PBS, sealed, magnetically stirred for 2 min, and vortexed vigorously for 2 min in order to release the adhered bacteria from the uncoated and coated substrate surfaces. Triplicate aliquots of the serial dilutions were cultured on nutrient agar and incubated for 24 h, after which the numbers of CFU were determined. These experiments were performed twice in triplicate, using the uncoated samples were used as negative controls. Statistical evaluation was done by one-way analysis of variance (ANOVA). The statistical significance (p-values) was calculated using Prism 8 Software.

3.4.2.3 Cell adhesion and proliferation assays

Human osteoblast-like cells (MG63) were cultured in Dulbecco's Modified Eagle Medium (DMEM; Sigma-Aldrich, Australia) supplemented with 1 mM sodium pyruvate, 4 mM L-glutamine, 100 mg/L streptomycins, 10% v/v fetal bovine serum, and 1% v/v non-essential amino acids [387]. Cells were seeded at 2×10^4 cells/well into each well of a 24-well polystyrene plate (Ultra-Low Attachment 24-Well Plate, Corning Inc., USA). The samples were sterilised by autoclaving, dip-cleaned in ethanol, and washed in triplicate by spray (pipette) washing with 1 M PBS. The cell culturing was done in triplicate at the time points 4 h, 2 days, 4 days, 7 days as follows:

- Wells with cells and sample (uncoated, CeO₂, Ga-doped CeO₂, or Mn-doped CeO₂ coating)
- Wells with medium and sample
- Wells with medium only (negative control)
- Wells with cells only (positive control; treated culture plate (TCP))

The standard cell viability assays have in common the requirement of chemical reduction of the tetrazolium reagent to formazan and the latter's solubilisation in cell culture medium. However, the MTS assay is a recently developed technique that offers some advantages over the other commonly

used assays, which are MTT and CCK-8 (or WST-8). These advantages include less complexity as it involves a single step instead of multiple steps, it is less toxic to cells, and it is faster [393].

The well plates were maintained during incubation in a humidified atmosphere (95% RH) at 37°C and 5% CO₂. Cell adhesion and proliferation were examined by the MTS assay (MTS assay, Promega, Australia). According to the manufacturer's instructions, the MTS reagent, containing tetrazolium inner salt 3-(4,5-dimethylthiazol-2-yl)-5-(3-carboxymethoxyphenyl)-2-(4-sulfophenyl)-2H-tetrazolium, was added to all wells 4 h prior to each abovenamed time point, followed by 4 h further incubation. The exception was for the first time point, when MTS reagent addition was done at 3.5 h, followed by incubation for 30 min.). Subsequently, 100 µL from each well was pipetted and transferred to a 96-well polystyrene plate (Sigma-Aldrich, Australia) and analysed immediately afterward by UV-Vis absorbance spectrophotometry at 490 nm using a plate reader (SynergyTM HTX Multi-Mode Microplate Reader, BioTek Instruments, USA).

For analysis by FESEM, samples with attached cells were removed from the wells and placed in the wells of a new 24-well polystyrene plate (Corning Inc., USA). Dead cells were removed by washing in 1 mL of 0.1 M PBS. The suspension was removed and replaced by pipette with 2.5% v/v glutaraldehyde, followed by curing in air at 20°C for 30 min in order to fix the cells. The fixative was removed from each well and the samples were washed by soaking for 5 min in 0.1 M PBS in triplicate. The samples then were dehydrated by soaking in a series of aqueous ethanol solutions of increasing concentration (30, 50, 70, 90, and 100%) for 30 min each, with the final soaks being done twice. After removal of the ethanol by pipetting, 0.5 mL of bis (trimethylsilyl)amine (HMDS, Sigma-Aldrich, Australia) were added to each well and the plate was stood cured in the air at 20°C for 20 min. Following removal by pipetting of the HMDS from each well, the plate was dried in air at 20°C for 12 h.

4. Results and Discussion – Coating Characteristics

Ceria in nanoparticulate form has been reported to show promise in various biological applications, including biosensing, bioanalysis, and disease therapy [341, 393-397]. CeO₂ is unique in its ability to undergo continuous and reversible Ce⁴⁺ ↔ Ce³⁺ switching and the consequent manifestation of pro-oxidant and anti-oxidant behaviour, resulting in the associated formation and elimination, respectively, of reactive oxygen species (ROS). This capability makes CeO₂ a promising candidate in reactive oxygen intermediated (ROI) conditions and in the improvement of the activity of alkaline phosphate (ALP), which is an osteoblast marker [51]. In effect, this switching can catalyse ROS neutralisation [341, 393] through the scavenging of hydrogen peroxide (H₂O₂), the superoxide radical •O²⁻, and the hydroxyl radical •OH, which are the principal ROS involved in the progression of cancer and other diseases [395-397].

Since enzymes that regulate ROS are metalloproteins that operate through the use of metal cofactors, metal oxide nanoparticles have been developed in order to mimic enzymatic reactions at biological levels [398]. The enzyme-like radical-scavenging behaviour of ceria derives from the intrinsic structural defect Ce³⁺ and the charge-compensating oxygen vacancies (V_O^{••}), despite the thermodynamic stability of CeO₂ (**Figure 4.1a**), where the low reduction potential for Ce³⁺/Ce⁴⁺ redox facilitates Ce⁴⁺ ↔ Ce³⁺ switching [341, 393, 399]. It has been shown that the redox potential of ceria is determined by the oxygen vacancy concentration ([V_O^{••}]) and a range of other structural, microstructural, and physicochemical factors [393] but also that increased [V_O^{••}] results in superior anti-oxidant behaviour [341].

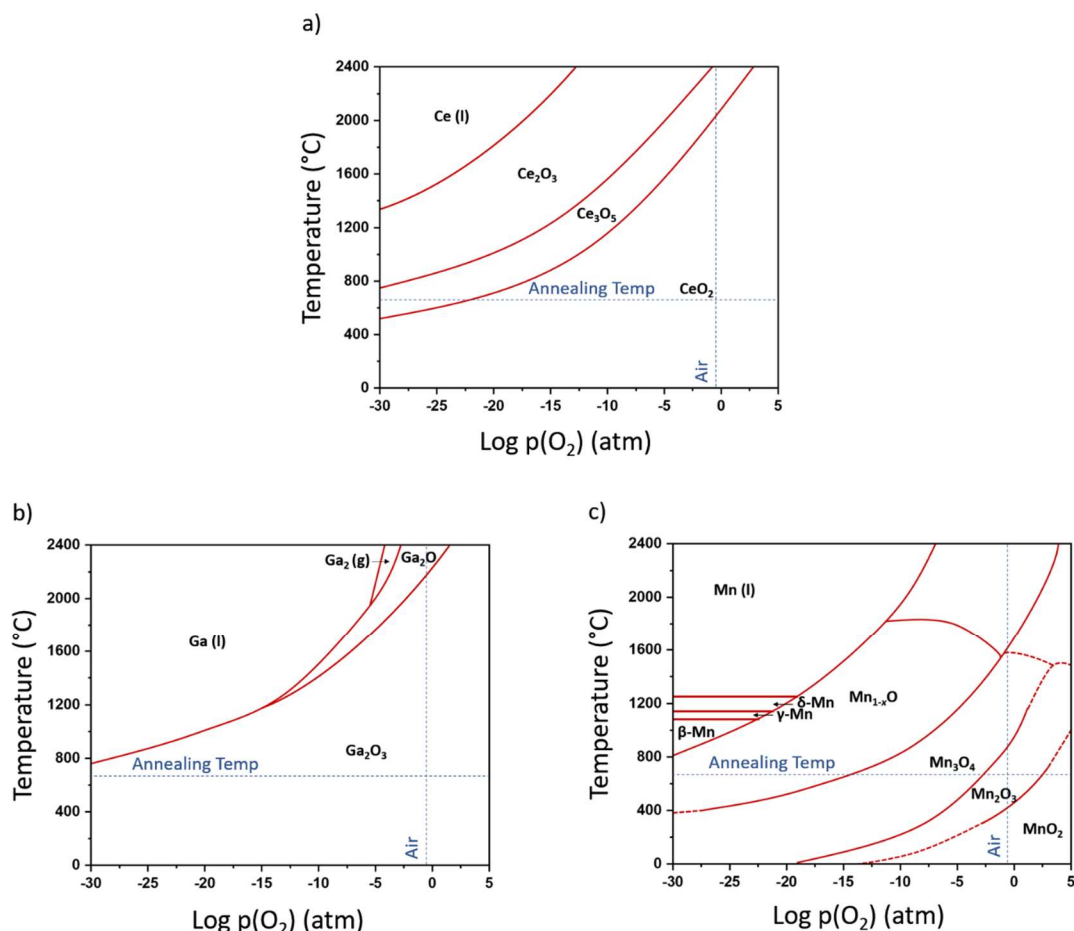


Figure 4.1. Thermodynamic stability diagrams of the (a) Ce-O system, (b) Ga-O system, and (c) Mn-O system calculated using FACT-Sage 7.0 and modified by other references [400-404]

Yanyan *et al.* [344] have shown that the $\text{Ce}^{4+}/\text{Ce}^{3+}$ ratio plays a significant role, where the lower the ratio, the better the antibacterial performance [346]. In particular, the effectiveness of CeO₂ is enhanced with the high surface areas and consequent high concentrations of Ce³⁺ through the fabrication of nanoparticles (NPs) [345]. Mengzhen *et al.* [346] divided the killing of bacteria into two stages: adsorption and antibacterial activity. The first stage includes electrostatic attraction between CeO₂ NPs and bacteria surfaces. The zeta potential of CeO₂ varies significantly from positive to negative as a function of processing method, although there is a clear trend of positive values in more acidic environments [342, 343, 345, 405], which are consistent with elevated Ce³⁺ concentrations. Since both gram-positive and gram-negative bacteria strains exhibit negative

surface charges [406, 407], this again highlights the importance of the $\text{Ce}^{4+}/\text{Ce}^{3+}$ ratio. The second stage is the antibacterial activity, which involves two possible processes [346]. The first mechanism is oxidative stress from the oxidation of the lipid contents, thus stimulating the formation of ROS that can degrade bacterial DNA, RNA, and proteins; the pro-oxidant formation of ROS is the major antibacterial mechanism for CeO_2 . The bacterial countermeasure to this process is the release of enzymes, including catalase and superoxide dismutase, to neutralise the ROS [408]. The second alternative mechanism is the reduction or elimination of nutrient transfer. Here, following adsorption of the CeO_2 NPs to the pathogen surfaces, the NPs may link to the mesosomes in the cell wall and interrupt cellular respiration and differentiation [409]; the NPs also may block nutrient transfer by reacting with the thiol groups (which transport the nutrients through the cell wall) of the proteins on the cell wall, thereby decreasing cell wall permeability. All these phenomena can lead to cell death.

Ga^{3+} has been shown to exhibit bactericidal activity upon replacement of Fe^{3+} in bacterial enzymatic pathways, which play a key role in the initiation, growth, and functioning of infections [273]. It has been shown that $\text{Ga}(\text{NO}_3)_3$ solution has osteoblastic and antibacterial properties and, as an FDA-approved drug, is used in the treatment of cancers resulting from hypercalcemia (*e.g.*, Paget's disease) and infectious diseases (*e.g.*, acute atopic dermatitis) [277, 278]. Mn^{2+} is a trace element that is distributed throughout the tissues, of which 99% is incorporated in bones [283, 284]. It is responsible for activating the metabolic enzymes involved in electron transfer reactions, antioxidant behaviour, and phosphorylation; the latter plays a significant role in the regulation of cellular processes. Unlike Ga^{3+} , which is a very stable valence state (**Figure 4.1b**), $\text{Mn}^{2+} \leftrightarrow \text{Mn}^{3+}$ occurs relatively easily (**Figure 4.1c**).

The intentions of the present work were to explore the structural, microstructural, and chemical effects of Ga³⁺- and Mn²⁺-doped CeO₂ as a sol-gel spin-coated thin films applied to 3D-printed biomedical-grade Ti6Al4V substrates. Since such coatings generally require heat treatment in order to effect bonding, thermal expansion (α) mismatch can lead to residual stresses that can accelerate coating deterioration or cause immediate failure upon cooling. In the present work, the thermal contractions upon cooling from 650°C for Ti6Al4V ($9.40 \times 10^{-6} \text{ }^{\circ}\text{C}^{-1}$) and CeO₂ ($7.69 \times 10^{-6} \text{ }^{\circ}\text{C}^{-1}$) [410-415] result in residual compressive stress on the deposited thin film on a substrate [416]. The ability to engineer the residual stress by alteration of the coating and/or surface and the attendant reduction in the E_g could be used to enhance the reactive oxygen species (ROS) production in order to kill bacteria.

4.1 Surface and Chemical Characterization

4.1.1 Field Emission Scanning Electron Microscopy (FESEM) and Transmission Electron Microscopy (TEM)

Figure 4.2 shows the morphologies of the substrate and coatings. **Figure 4.2a** shows a representative TEM image of a cross section of an undoped coating on the substrate, revealing a dense and well adhered film of uniform thickness of $\sim 0.82 \text{ nm}$. The SEM images of the undoped (**Figure 4.2b**) and doped (**Figure 4.2c-i**) samples show that the rough surface profile of the implant was retained in that the depressions were filled by the sol-gel but the substrate projections were retained as rounded asperities. EDS mapping of the dopants was not indicative owing to beam penetration and consequent dominance of the Ti signal. The samples generally exhibited angular cracks owing to shrinkage during drying and/or calcination, although the highest dopant levels (9GC, 9MC) exhibited lower densities of cracks, with the Mn-doped thin film being nearly crack-free. The differences in cracking are attributed to both variable viscosities and substrate penetration as a function of dopant level, as discussed subsequently.

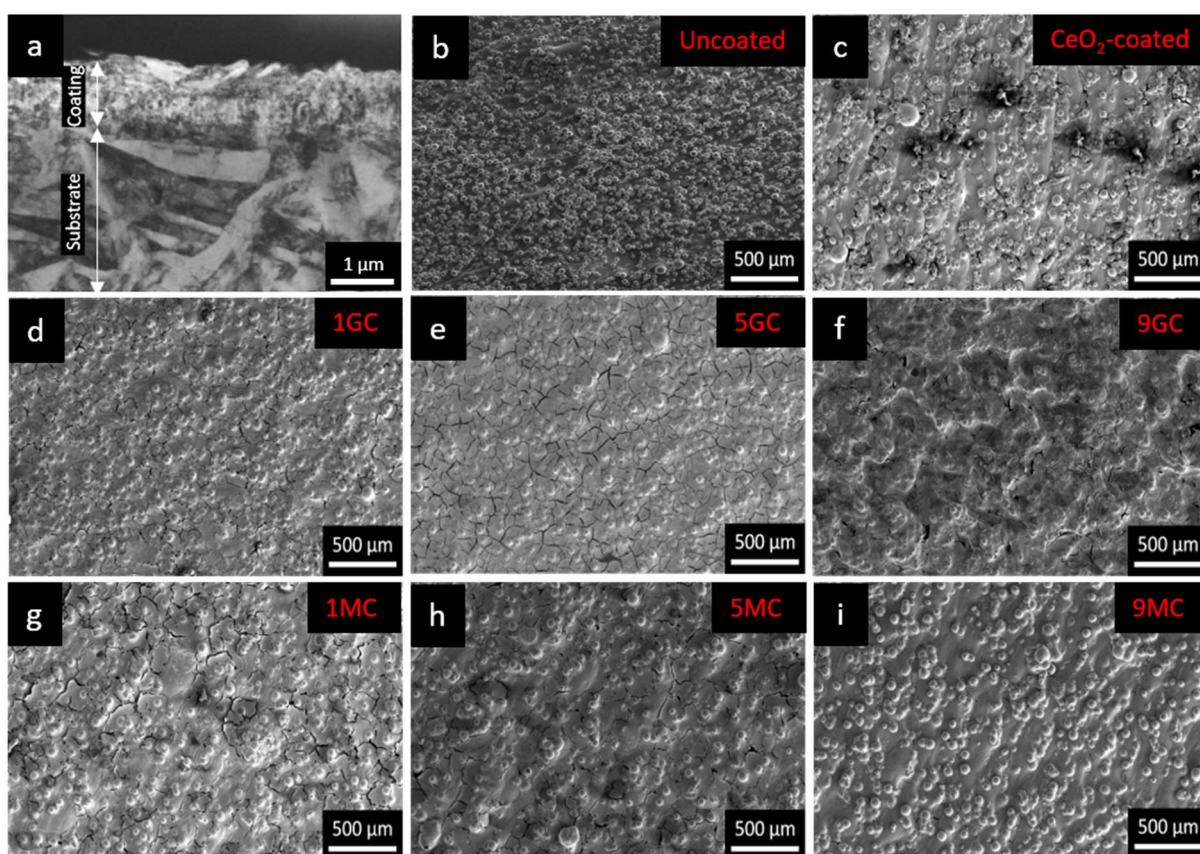


Figure 4.2. TEM images: (a) cross section of undoped CeO₂-coated sample; FESEM images: (b) uncoated substrate, (c) undoped CeO₂ coating, (d-f) Ga-doped CeO₂ coatings, (g-i) Mn-doped CeO₂ coatings; coatings calcined at 650°C for 2 h; GC = Ga-doped CeO₂; MC = Mn-doped CeO₂; preceding numbers = dopant level (mol%, metal basis)

4.1.2 3D-Laser Scanning Confocal Microscopy

The adhesion of bone cells (osteoblasts) is highly dependent on the surface features especially, roughness [417]. In the previous research, it was concluded that the roughness of the implant can trigger bone cell proliferation and differentiation by providing the suitable surface for the cells to attach and replicate and will result in bone-implant fixation.[418, 419]. So, effective fixation of implant in long run (osseointegration) strongly relies on bone on-growth and ingrowth (growing of bone cells on the implant and into the pores, respectively)[420, 421].

Figure 4.3 shows 3D laser scanning confocal microscopy images of the surface topographies (field of view 709.6 μm x 1000 μm). The surface roughness (Ra), which are summarised in **Figure 4.3a**, decreased only slightly when the substrate was CeO_2 -coated. This indicates that there was little coating of the asperities and most of the sol-gel was located in the depressions. The Ra values of the Ga-doped CeO_2 thin film initially increased slightly ($14 \pm 0.1 \mu\text{m}$). This indicates that the asperity heights were increased by the viscous coating while that over the depressions effectively was suspended over them. The Ra values of the Ga-doped CeO_2 at higher dopant levels decreased, especially at the highest dopant level. This reflected the observed increase in viscosity with doping, because of dopant-clusters forming and its corporation the viscosity coefficient increased, which effectively stiffened the suspended coatings and reduced sagging. The FESEM images, which indicate relative viscosities of the precursor films, reveal that increasing dopant levels increase the viscosity and decrease the roughness. This effect is a general phenomenon that results from the increasing network complexity of the solution, which reduces flow [16, 41-42]. As expected, this effect varied for Ga and Mn, where the former exhibited greater viscosity than the latter, as revealed numerically by the Ra roughnesses. The complexity of the network also was revealed through the cracking, which was reduced as the viscosity increased. These observations suggest that both dopants increased the viscosity and decreased the shrinkage and associated cracking owing to the preceding. However, the effects from Ga doping were greater than those from Mn doping, so the precursor of the latter was able to flow into the pores, allowing the substrate asperities to remain visible, while the precursor of the former effectively covered most of the substrate, allowing only the general profile established by the asperities.

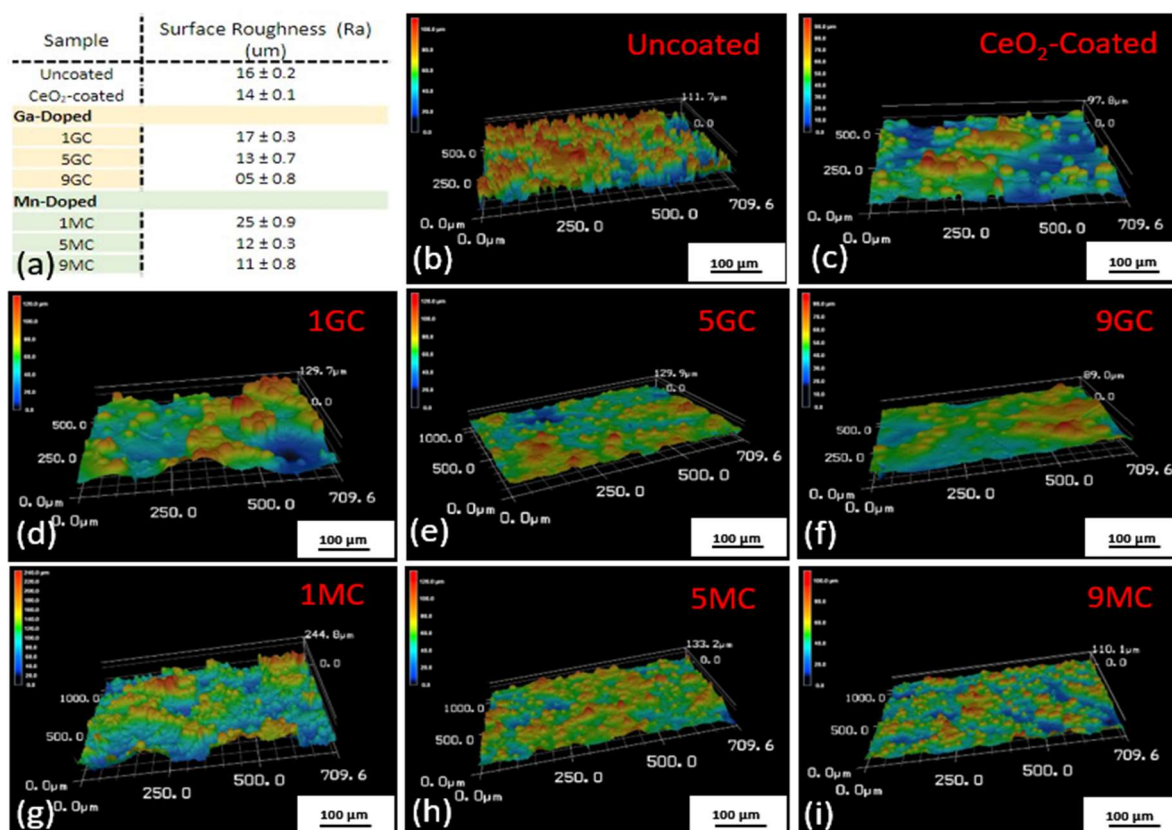


Figure 4.3. 3D laser scanning confocal microscopy image of surface topographies: (a) Summary of roughnesses (Ra), (b) uncoated substrate, (c) undoped CeO₂ coating, (d-f) Ga-doped CeO₂ coatings, (g-i) Mn-doped CeO₂ coatings; coatings calcined at 650°C for 2 h

The Ra values of the Mn-doped CeO₂ thin film initially increased significantly. This suggests that wetting by Mn was greater than that by Ga, so the asperities were well coated by the sol-gel but the viscosity, which was observed to be lower than that of the Ga-doped precursors, allowed the Mn-doped precursor to flow into the depressions. The comparative viscosities, shown in **Figure 4.4**, confirm the preceding. The Ra values of the Mn-doped CeO₂ thin films at higher dopant levels decreased to values equivalent to that of the intermediate Ga-doped CeO₂ thin film. Hence, the viscosities of the Mn-doped precursors were sufficient to prevent the filling of the depressions, thereby coating the substrates relatively continuously but not to the extent shown by the highest Ga-doped precursor.

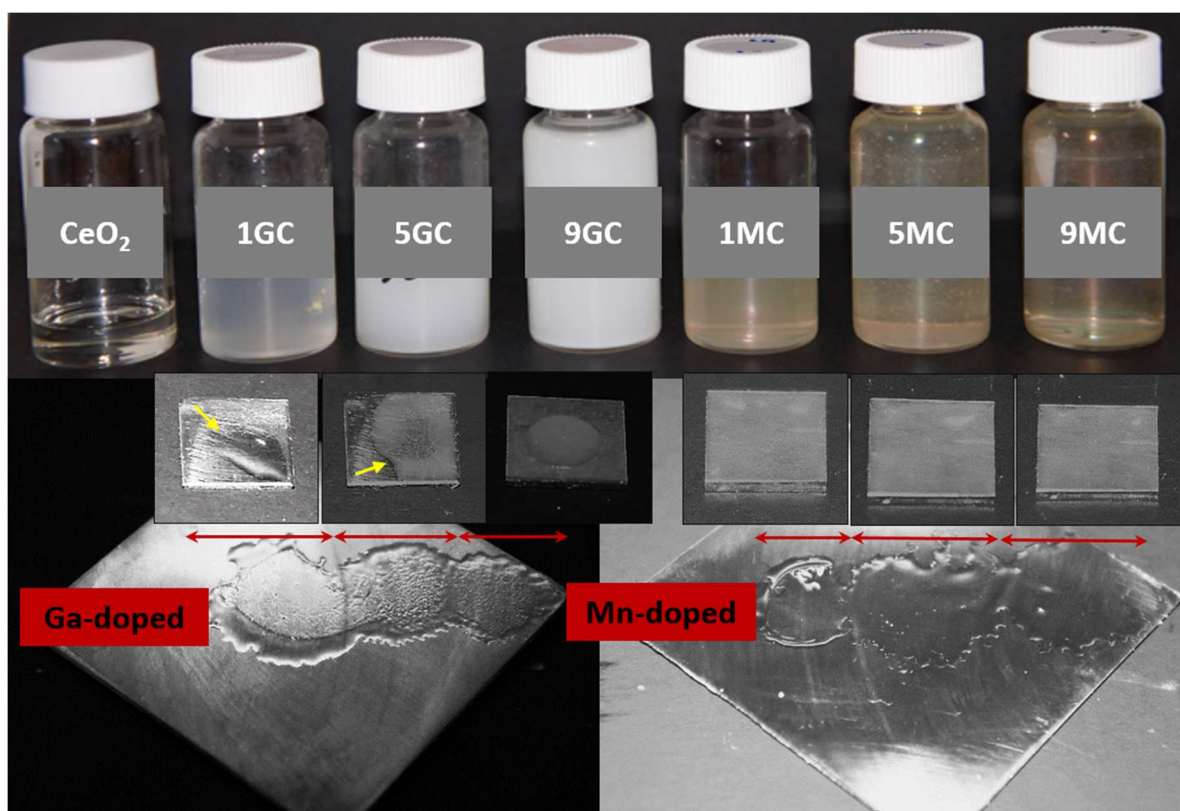


Figure 4.4. Undoped, Ga-doped, Mn-doped CeO_2 samples: Top – Transparencies of sols, Middle – Viscosities of sols deposited on smooth Ti substrates, Bottom – Comparative viscosities of sols (left – 1 mol% dopant, middle – 5 mol% dopant, right – 9 mol% dopant) deposited on smooth Ti substrates

An additional observation is that the broader topographical features, which are shown in **Figures 4.4b-i**, are revealed in the surfaces of the uncoated substrate and those of the coated films of the lowest dopant level. Here, the uneven large-scale topography, as opposed to the local surface roughnesses, are revealed. Both the unevenness and roughness clearly are mitigated by the application of the thin films, especially at the highest dopant levels, which yield the most viscous and hence least deformable thin films. These are in a good agreement with viscosity results in **Figure 4.4**, which clearly reveals the change in wetting by increasing the dopant level. For the Ga-

doped precursors, the addition of more Ga increased the extent of precipitation while the wetting decreased. In contrast, the Mn-doped precursors revealed a reverse trend.

The accompanying images of the translucencies of the precursor liquids reveal that the precursors consisted of suspensions, where increasing the Ga dopant concentration increased the precipitation while increasing the Mn dopant concentration increased the precipitate's solubility.

4.2 Mineralogical Properties

4.2.1 Raman Microspectroscopy

The natures of the precipitates were assessed by Raman by placing a drop of suspension on a fused silica substrate, which revealed that the precipitates were amorphous (**Figure 4.5a**). Since the extents of precipitation/solubility were opposite for the two dopant systems, this suggests that the precipitates are not Ce-based but that they consist of dopant species. If so, then the presence of precipitates indicates that the extents of doping of CeO_2 are underestimated, which increases differentially with Ga and decreases with Mn.

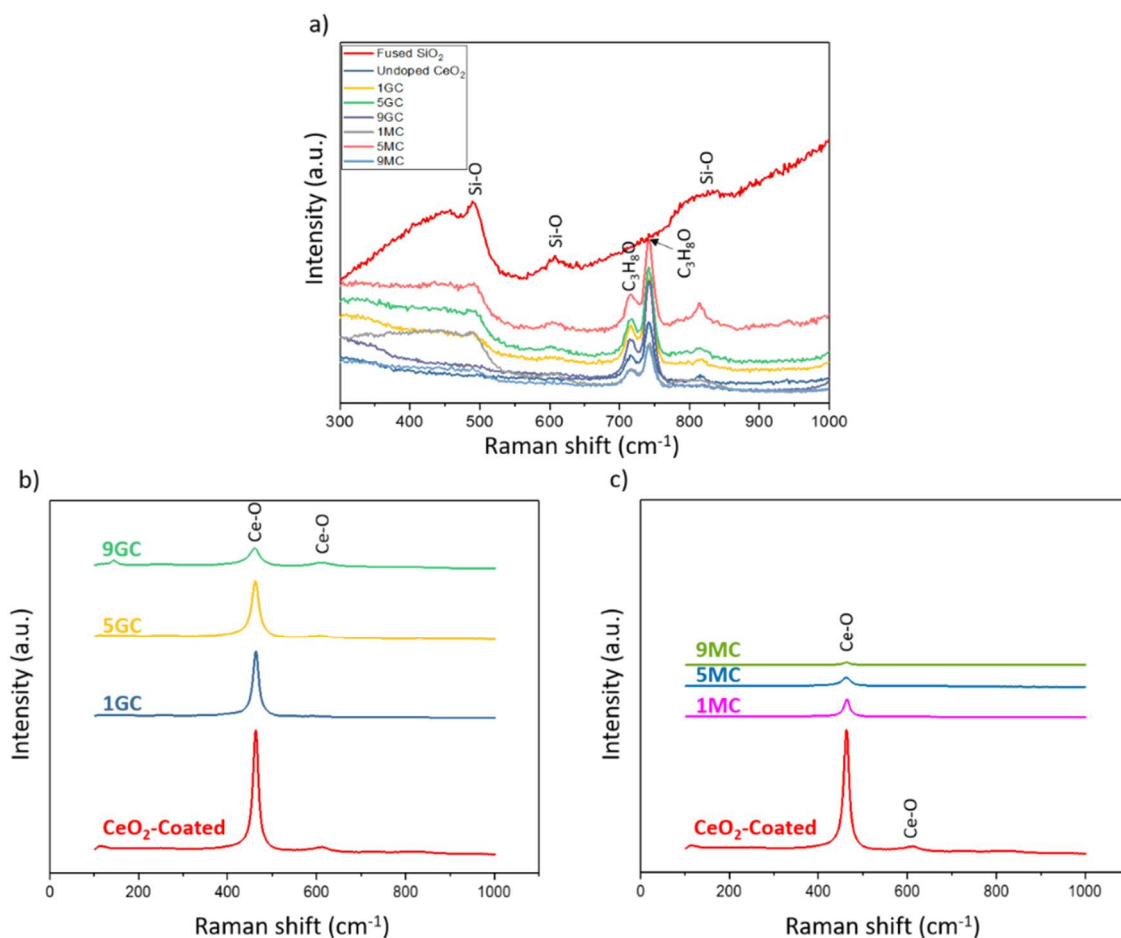


Figure 4.5 Laser Raman microspectra of (a) undoped, Ga-doped, and Mn-doped CeO₂ sol-gel films (unannealed) and fused SiO₂ substrate; (b) Ga-doped CeO₂ coatings, (c) Mn-doped CeO₂ coatings; calcined at 650°C for 2 h (identical peak intensity ranges)

4.2.2 X-ray Diffraction (XRD)

The GAXRD data in **Figure 4.6** indicate that Ga₂O₃ is highly soluble in CeO₂ since no Ga₂O₃ was detected. This is confirmed by the XPS data (Table S6), which show both the presence of Ga and corresponding changes in Ce³⁺/Ce⁴⁺ ratios. The low GAXRD peak intensities (counts not shown) indicate that dissolved Ga₂O₃ destabilised the CeO₂ structure but the increasing intensities with doping indicate that Ga₂O₃ still enhanced the gel → crystalline conversion, probably by acting as a nucleating agent. It is uncertain if the non-detection of Ga₂O₃ resulted from its dissolution or its

precipitation and/or recrystallisation at a level below the limit of detection of the instrument (typically ~ 1 vol% [422]).

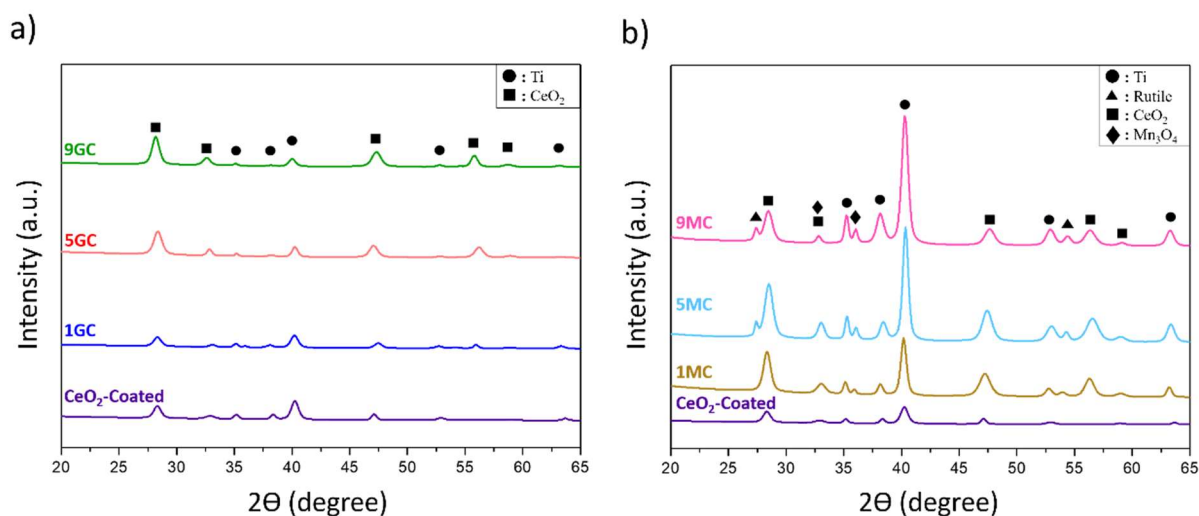


Figure 4.6. GAXRD patterns of: (a) Ga-doped CeO_2 coatings, (b) Mn-doped CeO_2 coatings; coatings calcined at 650°C for 2 h (identical peak intensity ranges except for the uncoated substrate)

In contrast, the solid solubility of Mn in CeO_2 is lower than that of Ga, as evidenced by the precipitation/recrystallisation of Mn_3O_4 with 5MC and 9MC. Similarly, the solid solubility of Mn in CeO_2 is demonstrated by the XPS data (Table S6), which shows both the presence of Mn (at a lower level than for Ga) and corresponding changes in $\text{Ce}^{3+}/\text{Ce}^{4+}$ ratios. However, the higher GAXRD peak intensities for all of the Mn-doped samples compared to the CeO_2 -coated sample is a clear indication that Mn dissolved and enhanced recrystallisation. Further, it appears that this effect was maximised for 5 MC, suggesting saturation solubility in the range 1-5 mol% Mn, with supersaturation and consequent structural destabilisation at 9 mol% Mn. It can be noted that these differential solubilities may reflect not only intrinsic behaviour but they also may reflect the extrinsic effect of precursor viscosity, as shown in **Figure 4.4**, and consequent intimacy of interfacial contact area.

The Gibbs free energies of formation for some potential reactions between film and substrate and for Mn oxide formation are shown in **Figures 4.7a** and **4.7b**, respectively. The former data show that, for the calcination temperature of 650°C, Ga₂O₃ and all of the Mn oxides are predicted to react with the Ti of the substrate. However, the reaction between Ga₂O₃ and Ti would not occur as all of Ga dissolved in the CeO₂. These data also show that the most favourable reaction is between the precipitate Mn₃O₄ and Ti to form MnO and TiO₂ (rutile polymorph). The detection of rutile in the samples with Mn₃O₄ supports this reaction, although MnO appears to be absent or undetectable and rutile could be a product of Ti oxidation. However, **Figure 4.1c** supports the conclusion that MnO should not form. Consequently, if MnO were present but below the level of detection, the calcining conditions of 2 h at 650°C were insufficient to equilibrate the film and substrate. Thermodynamic non-equilibrium is implicit since the thermodynamics data in **Figure 4.7a** also show that CeO₂ and Ti are not compatible.

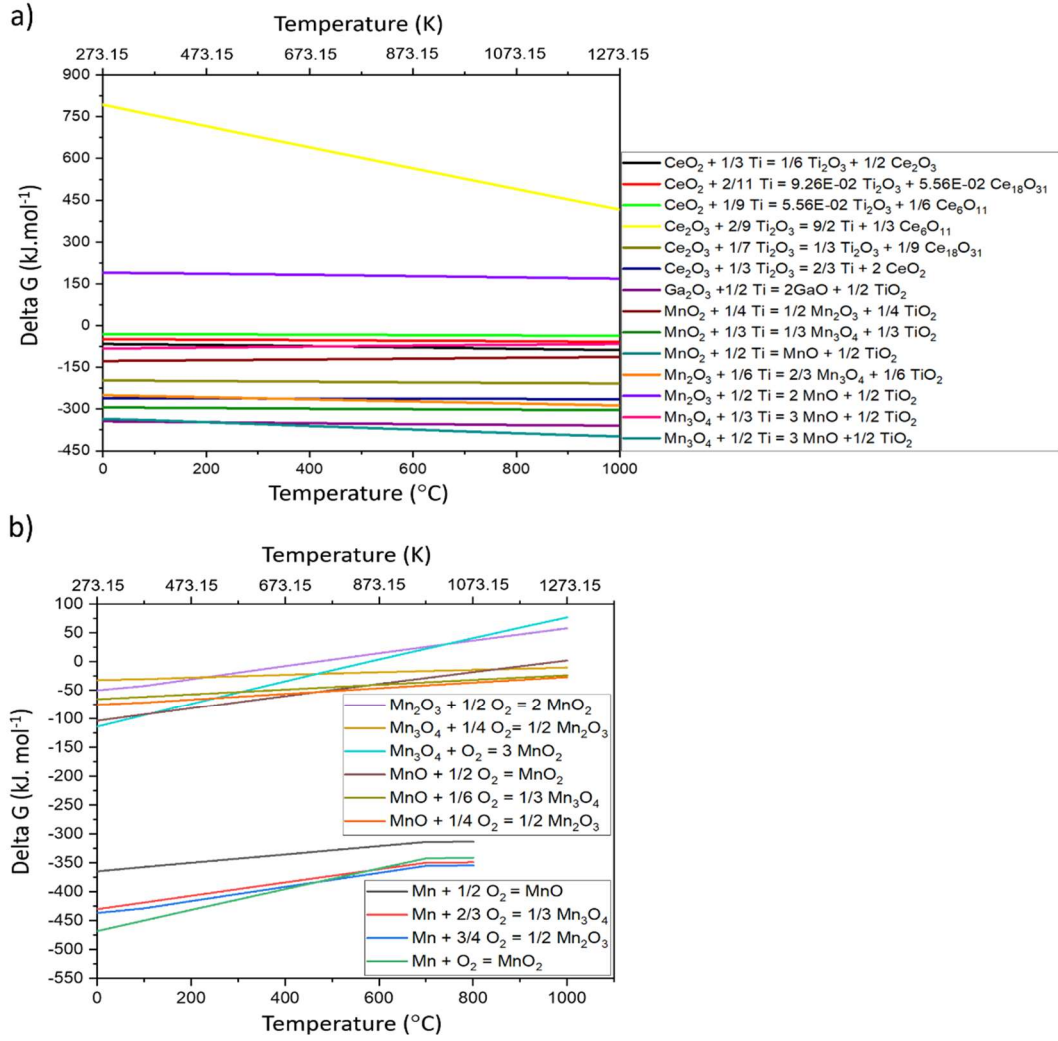


Figure 4.7 Gibbs free energies of formation for (a) possible film-substrate reactions, (b) Mn oxides at various temperatures (TiO_2 is rutile polymorph)

The GAXRD data for the coatings are given in **Table 4.1**. They reveal only slight expansion from both dopants and insignificant changes in the lattice parameter with varying dopant levels. However, the crystallite sizes were significantly different, decreasing in the order undoped > Mn-doped > Ga-doped. The residual strains were conversely correspondent, increasing in the same order. These observations are consistent with low but significant solid solubilities of the dopants. **Figure 4.8** and **Table 4.2** show that both Ce^{4+} (0.111 nm in eightfold coordination) and the central interstice in CeO_2 (0.110 nm, also in eightfold coordination) are very large, while the ionic radii of

Ga and Mn are considerably smaller. The cation and anion sublattices in CeO_2 also are sufficiently large to allow the passage of dopants to reach the central interstice. Despite the apparent ease of interstitial solid solubility, the lattice expansions and the ionic radii data suggest that the solid solubility mechanism is substitutional.

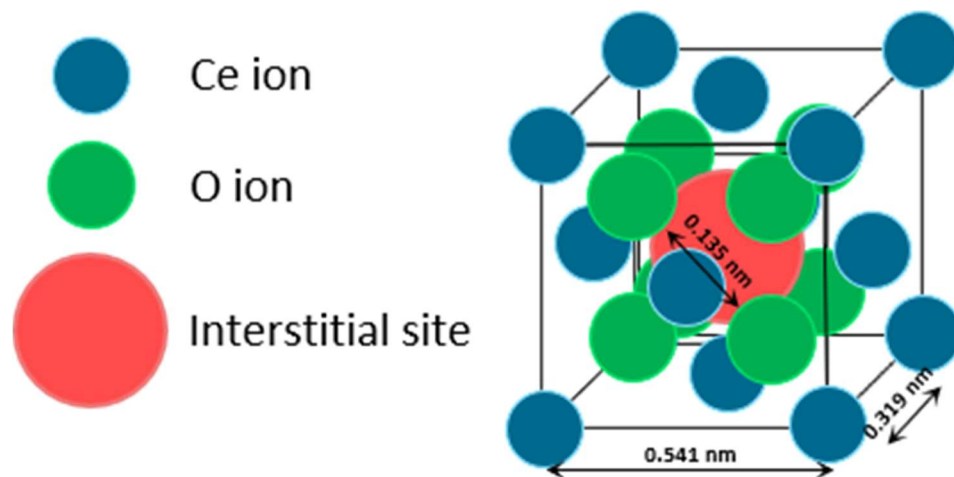


Figure 4.8. Calculated sizes of interstices in CeO_2 ($\text{Ce}_{\text{VIII}}^{4+} = 0.111 \text{ nm}$, $\text{O}_{\text{IV}}^{2-} = 0.124 \text{ nm}$ [423])

Table 4.1. *Crystallographic data for CeO₂ coatings calcined at 650°C for 2 h*

Sample	Lattice Parameter		Unit Cell Volume ^b	True Density ^c	Rietveld Refinement		Scherrer	
	(nm)	GOF ^a			Crystallite	Residual	Crystallite	Residual
<i>a</i>	(nm) ³	(kg/m ³)	Size ^d	Strain ^e	Size ^d	Strain ^e		
			(nm)	(%)	(nm)	(%)		
Ce-Coated	0.5404	3.43	0.1579	7260	10.52	0.311	19.7	0.865
Ga-Doped								
1GC	0.5407	2.59	0.1581	7230	6.61	0.495	19.7	0.870
5GC	0.5408	2.79	0.1582	7220	7.89	0.415	11.4	1.399
9GC	0.5406	2.27	0.1580	7230	7.84	0.417	13.0	1.249
Mn-Doped								
1MC	0.5411	20.8	0.1585	7210	8.12	0.403	13.0	1.242
5MC	0.5412	25.4	0.1585	7230	7.15	0.458	11.4	1.392
9MC	0.5407	26.1	0.1581	7250	6.57	0.498	11.4	1.394

^a GOF: Goodness of fit

^b Calculated from Rietveld refinement [424]

^c Calculated from lattice parameter using Scherrer equation [425]

^d Calculated using Rietveld refinement analysis of GAXRD peaks and Scherrer equation [425] (based on full width at half maximum (FWHM) of (111) peak (FWHM standard = 0.095 [426]))

^e Calculated by difference between experimental and standard lattice parameters

Table 4.2. *Relevant Shannon crystal radii [427]*

Cation	Valence	Spin State	Coordination	Crystal Radius (nm)	Thin Film Contamination		Substrate Contamination	
					Substitutional	Interstitial	Substitutional	Interstitial
					Radius Difference with Ce ⁴⁺ (%) in	Difference with Eightfold	Radius Difference with Ti ⁴⁺ (%) in	Difference with
					Eightfold Coordination	Interstice in CeO ₂ (%)	Twelvefold Coordination	Twelvefold Interstice (%)
Ti	2+	–	VI	0.1	–9.9	– 9.1	– 2.0	+334.8
		–	IV	0.056	–49.5	–49.1	–45.1	+143.5
	3+	–	VI	0.081	–27.0	–26.4	–20.6	+252.2
		--	VIII	(0.956) ^a	–13.9	–13.1	– 6.3	+315.7
		–	V	0.065	–41.4	–40.9	–36.3	+182.6
	4+	–	VI	0.0745	–32.9	–32.3	–27.0	+223.9
		–	VIII	0.088	–20.7	–20.0	–13.7	+282.6
		–	XII	(0.102) ^b	– 8.1	– 7.3	–	+343.5
		–	V	(0.100) ^c	– 9.9	– 9.1	– 2.0	+334.8
Ce	3+	–	VI	0.115	+ 3.6	+ 4.5	+12.7	+400.0
		–	VII	0.121	+ 9.0	+10.0	+18.6	+426.1

Cation	Valence	Spin State	Coordination	Crystal Radius (nm)	Thin Film Contamination		Substrate Contamination			
					Substitutional	Interstitial	Substitutional	Interstitial		
					Radius Difference with Ce ⁴⁺ (%) in	Difference with Eightfold	Radius Difference with Ti ⁴⁺ (%) in	Difference with Twelvefold		
					Eightfold Coordination	Interstice in CeO ₂ (%)	Twelvefold Coordination	Interstice (%)		
	4+	–	VIII	0.1283	+15.6	+16.6	+25.8	+457.8		
		–	IX	0.1336	+20.4	+21.5	+31.0	+480.9		
		–	X	0.139	+25.2	+26.4	+36.3	+504.3		
		–	XII	0.148	+33.3	+34.5	+45.1	+543.5		
		–	V	(0.088) ^c	–20.7	–20.0	–13.7	+282.6		
		–	VI	0.101	– 9.0	– 8.2	– 1.0	+339.1		
		–	VIII	0.111	+ 0.0	+ 0.9	+ 8.8	+382.6		
		–	X	0.121	+ 9.0	+10.0	+18.6	+426.1		
		–	XII	0.128	+15.3	+16.4	+25.5	+456.5		
		–	IV	0.061	–45.0	–44.5	–40.2	+165.2		
		Ga	3+	–	V	0.069	–37.8	–37.3	–32.4	+200.0
				–	VI	0.076	–31.5	–30.9	–25.5	+230.4

Cation	Valence	Spin State	Coordination	Crystal Radius (nm)	Thin Film Contamination		Substrate Contamination	
					Substitutional	Interstitial	Substitutional	Interstitial
					Radius Difference	Difference with	Radius Difference	Difference with
					with Ce ⁴⁺ (%) in	Eightfold	with Ti ⁴⁺ (%) in	Twelvefold
					Eightfold	Interstice in CeO ₂	Twelvefold	Interstice (%)
					Coordination	(%)	Coordination	
Mn	2+	–	VIII	(0.090) ^a	–18.9	–18.2	–11.8	+291.3
			XII	(0.104) ^b	– 6.3	– 5.5	+ 2.0	+352.2
		High	IV	0.08	–27.9	–27.3	–21.6	+247.8
		High	V	0.089	–19.8	–19.1	–12.7	+287.0
		Low	VI	0.081	–27.0	–26.4	–20.6	+252.2
		High	VI	0.097	–12.6	–11.8	– 4.9	+321.7
		High	VII	0.104	– 6.3	– 5.5	+ 2.0	+352.2
		–	VIII	0.11	– 0.9	+ 0.0	+ 7.8	+378.3
		–	XII	(0.126) ^b	+13.5	+14.5	+23.5	+447.8
		–	V	0.072	–35.1	–34.5	–29.4	+213.0
	3+	Low	VI	0.072	–35.1	–34.5	–29.4	+213.0
		High	VI	0.0785	–29.3	–28.6	–23.0	+241.3

Cation	Valence	Spin State	Coordination	Crystal Radius (nm)	Thin Film Contamination		Substrate Contamination	
					Substitutional	Interstitial	Substitutional	Interstitial
					Radius Difference	Difference with	Radius Difference	Difference with
					with Ce ⁴⁺ (%) in	Eightfold	with Ti ⁴⁺ (%) in	Difference with
					Eightfold	Interstice in CeO ₂	Twelvefold	Twelvefold
					Coordination	(%)	Coordination	Interstice (%)
O	2–	–	VIII	(0.089) ^d	–19.8	–19.1	–12.7	+287.0
			XII	(0.103) ^b	– 6.8	– 6.0	+ 1.4	+349.6
			II	0.121	+ 9.0	+10.0	+18.6	+426.1
			III	0.122	+ 9.9	+10.9	+19.6	+430.4
			IV	0.124	+11.7	+12.7	+21.6	+439.1
			VI	0.126	+13.5	+14.5	+23.5	+447.8
Ti	–	–	VIII	0.128	+15.3	+16.4	+25.5	+456.5
			IV	0.023	–	–	–	–
Interstice								
CeO₂	–	–	VIII	0.110	–	–	–	–
Interstice								

^a Radius not available but estimated on basis of assumed constant ratio Ti⁴⁺(VI)/Ti⁴⁺(VIII) = 0.847

^b Radius not available but estimated on basis of assumed constant ratio $\text{Ce}^{4+}(\text{VIII})/\text{Ce}^{4+}(\text{XII}) = 0.867$

^c Radius not available but estimated on basis of assumed constant ratio $\text{Ti}^{4+}(\text{V})/\text{Ti}^{4+}(\text{VI}) = 0.872$

^d Radius not available but estimated on basis of assumed constant ratio $\text{Mn}^{2+}(\text{VI, HS})/\text{Mn}^{2+}(\text{VIII}) = 0.882$

The GAXRD data for the Ti alloy substrate is given in **Figure 4.9** and **Table 4.3**. They reveal that contamination from Ce, Ga, and Mn doping is likely to have occurred, as indicated by the Ti lattice expansions. The crystallite sizes also changed, in this case increasing in the order undoped < Ce-coated < Ga-doped < Mn-doped. The changes in residual strains were significant, increasing in the order Ce-coated < Mn-doped < Ga-doped.

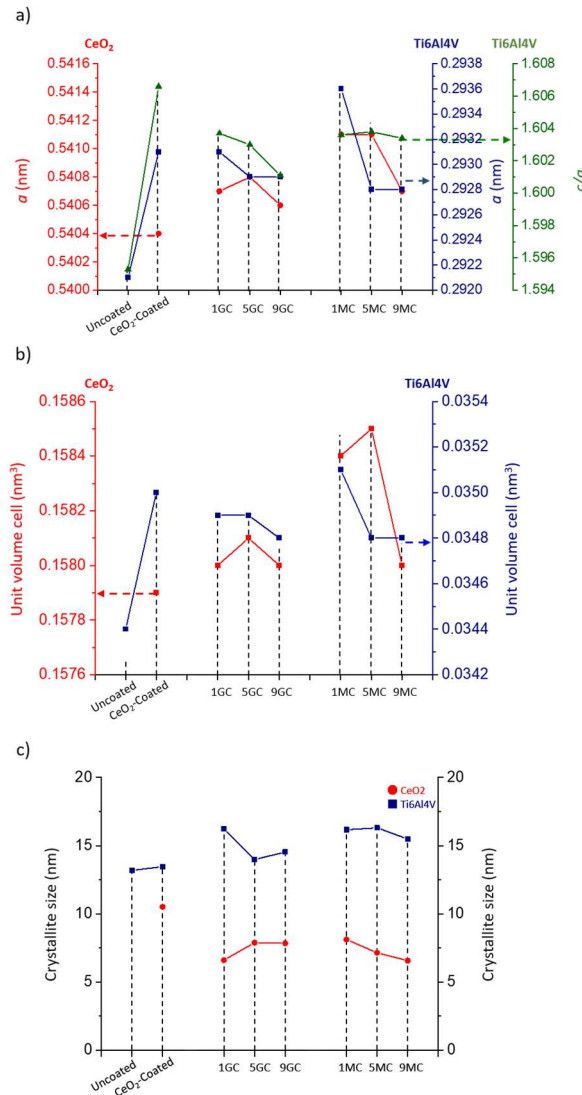


Figure 4.9. Graphical Rietveld analytical data for: (a) lattice parameters, (b) unit cell volumes, (c) crystallite sizes for (left) uncoated and CeO₂-coated substrates, (centre) Ga-doped CeO₂ coatings, (right) Mn-doped CeO₂ coatings, all with corresponding Ti6Al4V data; coatings calcined at 650°C for 2 h

Table 4.3. Crystallographic data for 3D-printed Ti6Al4V after heating at 650°C for 2 h

Sample	Lattice Constants (nm)			GOF ^a	Unit Cell Volume ^b (nm) ³	True Density ^c (kg/m ³)	Rietveld Refinement		Scherrer	
	<i>a, b</i>	<i>c</i>	<i>c/a</i>				Crystallite Size ^d (nm)	Residual Strain ^e (%)	Crystallit e Size ^d (nm)	Residual Strain ^e (%)
Uncoated	0.2921	0.4661	1.5953	0.21	0.0344	4620	13.19	0.248	13.6	0.844
Ce-Coated	0.2931	0.4710	1.6066	0.39	0.0350	4540	13.46	0.243	18.1	0.659
Ga-Doped										
1GC	0.2931	0.4701	1.6037	0.20	0.0349	4550	16.22	0.202	20.3	0.601
5GC	0.2929	0.4696	1.6030	0.20	0.0349	4560	13.98	0.234	18.9	0.637
9GC	0.2929	0.4691	1.6011	0.19	0.0348	4560	14.54	0.225	15.7	0.747
Mn-Doped										
1MC	0.2936	0.4708	1.6036	0.20	0.0351	4520	16.17	0.202	18.9	0.638
5MC	0.2928	0.4696	1.6038	0.20	0.0348	4560	16.31	0.201	18.9	0.638
9MC	0.2928	0.4696	1.6034	0.21	0.0348	4560	15.49	0.211	15.5	0.746

^a GOF: Goodness of fit

^b Calculated from Rietveld refinement [424]

^c Calculated from lattice parameter using Scherrer equation [425]

d Calculated using Rietveld refinement analysis of GAXRD peaks and Scherrer equation [425] (based on full width at half maximum (FWHM) of (111) peak (FWHM standard = 0.095 [426]))

e Calculated by difference between experimental and standard lattice parameters

Table 4.2 shows that the interstice in Ti is very small (0.023 nm), so interstitial solid solubility is highly unlikely. The similar ionic radii in **Table 4.2** indicate that substitution of Ti by Ga^{3+} and Mn^{3+} is very likely, although there would be little lattice strain. However, Ce^{4+} and Mn^{2+} solid solubility would occur with ~25% Ti lattice expansion, which is consistent with Hume-Rothery's size rule for substitutional solid solubility of close-packed metal lattices [428]. Since this states that the dopant radius ionic must have $\leq 15\%$ difference from that of the matrix ionic radius for *substantial* solid solubility, then only limited solid solubility would be expected. Since Ga^{3+} doping caused the greatest lattice strain but its ionic radius is similar to that of Ti^{4+} , then this would result from the combined Ga^{3+} and Ce^{4+} doping, suggesting that the non-identification of Ga_2O_3 precipitates is a result of an enlarged solid solubility homogeneity region for the Ga-Ce solubility in Ti. Thus, the equivalent Mn-Ce doping would be associated with a smaller extent of combined solid solubility and hence less lattice strain. This is consistent with the observation of Mn_3O_4 . The non-correlation with the crystallite sizes is suggested by the GAXRD peak intensities in **Figure 4.6**, where both Ce and Ga doping destabilised the Ti structure while Mn doping enhanced it.

Hume-Rothery's rules for *substantial* substitutional solid solubility in metals [428] also include a crystal structure rule (they should be identical), a valence rule (they should be identical or nearly so), and an electronegativity rule (they should be similar). Limited solubility is supported by the crystal structure rule since α -Ti is hexagonal but Ce and Mn are cubic and Ga is orthorhombic [429]. The valence rule suggests substantial substitutional solid solubility for Ce^{4+} in Ti^{4+} , lower solubilities in Ti^{4+} for Ga^{3+} and Mn^{3+} , and the lowest solubility for Mn^{2+} . Concerning the electronegativity rule, the relevant data are given in **Table 4.4**, which shows that, for the eight scales of electronegativity, there is only one value for Ti, which is similar to those of Ga and Mn (no value for Ce). A similar analysis can be done for Ga and Mn doping of CeO_2 but the limited substitutional solid solubility is sufficiently unambiguous to make this unnecessary.

Table 4.4. *Reported electronegativities of Ti, Ce, Ga, and Mn in different scales*

Scale	Smith	Allred	Allred– Rochow	Little, Jr.	Mulliken	Pauling	Pearson	Sanderson	Nagle
Ref	[430]	[431]	[432]	[433]	[434-436]	[437]	[438]	[439]	[440]
Atom									
Ti	–	–	–	–	–	–	3.45	–	–
Ce	–	–	1.08	1.08	–	1.12	–	–	–
Ga	–	–	–	–	–	–	3.20	–	–
Mn	–	–	–	–	–	–	3.72	–	–
Ion									
Ti ³⁺	1.50	1.38	1.32	1.32	5.20	1.54	40.30	1.09	–
Ti ⁴⁺	1.65	–	–	–	–	–	–	1.50	–
Ce ³⁺	1.15	1.12	–	1.08	–	–	28.48	–	1.05
Ce ⁴⁺	1.50	–	–	–	–	–	–	–	–
Ga ³⁺	1.70	1.81	1.82	–	2.01	1.81	47.00	2.41	1.56
Mn ²⁺	1.50	1.55	1.60	–	–	1.55	24.66	1.66	1.36
Mn ³⁺	1.85	–	–	–	–	–	42.40	2.20	–

4.2.3. X-Ray Photoelectron Spectroscopy (XPS)

XPS measurements were obtained and the data plots are shown in **Figure 4.10**. The numerical data for the Ce/O and normalised Ce⁴⁺/Ce³⁺ ratios are given in **Table 4.5** and plotted in **Figure 4.11**.

The measured dopant levels also are given in **Table 4.5**.

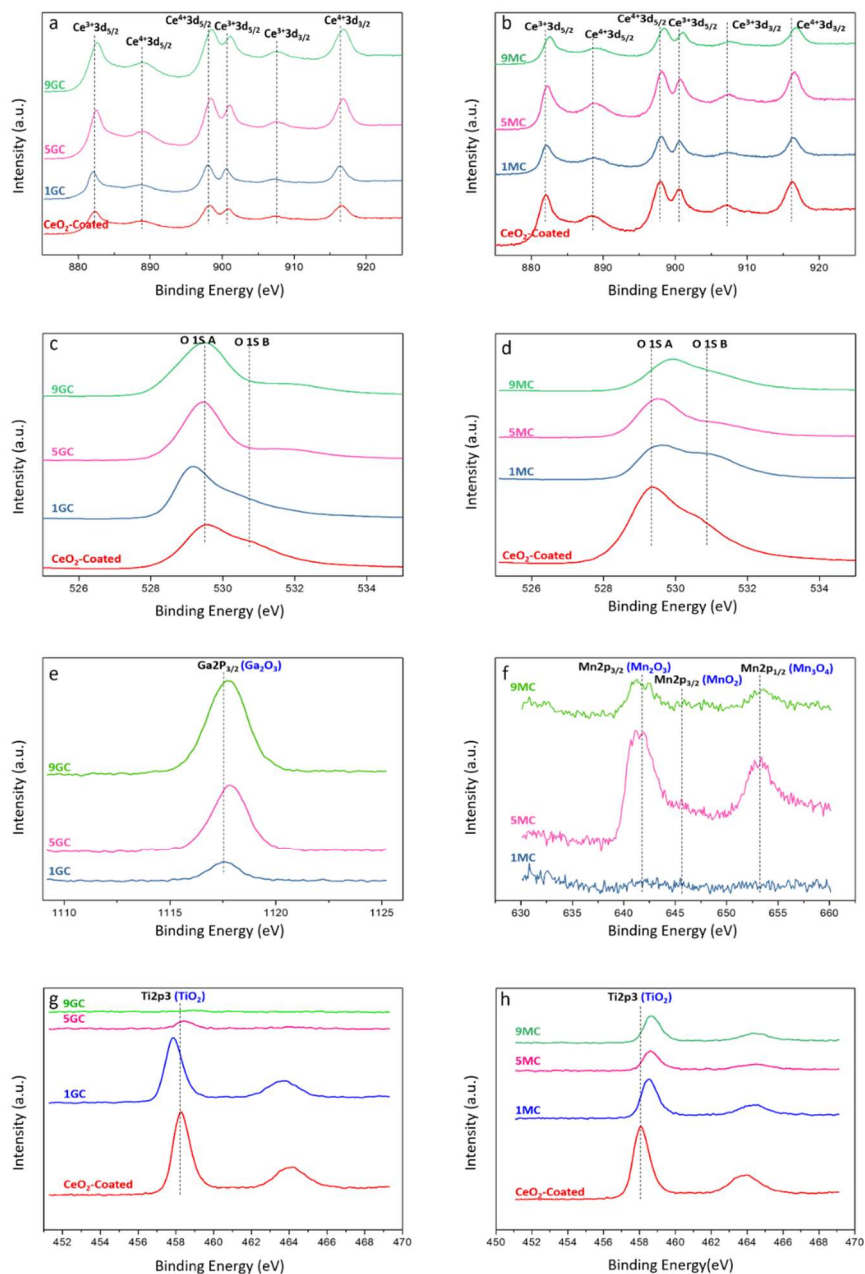


Figure 4.10. XPS spectra: (a) Ce3d for undoped and Ga-doped CeO₂-coated substrates, (b) Ce3d for undoped and Mn-doped CeO₂-coated substrates, (c) O1s for undoped and Ga-doped CeO₂-coated substrates, (d) O1s for undoped and Mn-doped CeO₂-coated substrates, (e) 2P_{3/2} for Ga-doped CeO₂-coated substrates, (f) 2P_{3/2} and 2P_{1/2} for Mn-doped CeO₂-coated substrates, (g) Ti2p₃ for undoped and Ga-doped CeO₂-coated substrates, (h) Ti2p₃ for undoped and Mn-doped CeO₂-coated substrates; coatings calcined at 650°C for 2 h (peak identifications based on data from National Institute of Standards and Technology XPS database [441])

Table 4.5. XPS surface compositions for Ce, Ga, and Mn (at%)

Sample	Ce 3d			Ce O1s	Ce/O	Ga 2p3	Mn 2p3
	% Ce ³⁺	% Ce ⁴⁺	Ce ³⁺ + Ce ⁴⁺				
CeO₂-Coated	17.42	82.58	12.08	87.92	0.14	—	
Ga-Doped							
1GC	21.78	78.22	12.56	86.13	0.15	1.32	—
5GC	20.15	79.85	20.82	74.66	0.28	4.52	—
9GC	18.86	81.14	20.41	73.35	0.28	6.24	—
Mn-Doped							
1MC	23.52	76.48	13.31	86.38	0.15	—	0.31
5MC	19.36	80.64	20.85	75.89	0.27	—	3.25
9MC	22.34	77.66	14.99	83.75	0.18	—	1.26

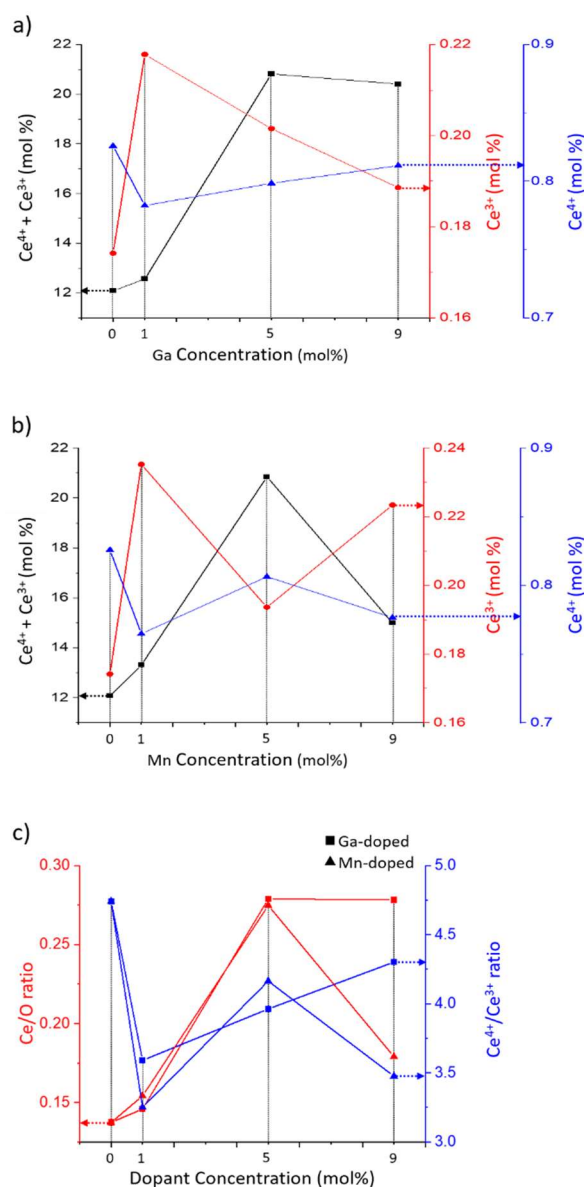


Figure 4.11. Relative XPS data: (a) effects of Ga dopant level on Ce levels, (b) effects of Mn dopant level on Ce levels, (c) effects of Ga and Mn dopant levels on Ce/O and $\text{Ce}^{4+}/\text{Ce}^{3+}$ ratios

Figures 4.10a,b reveal Ga and Mn doping both increased the binding energies and hence the valence of Ce. This would be expected to result in a trend (1 to 9 mol%) of lattice contraction, which is the case for the two highest dopant levels (9GC, 9MC), as shown in **Figures 4a,b** and **Table 4.1**. The irregular O1s data suggest that the lattice disturbance from the initial doping (1GC, 1MC) was inconsistent in its effects as a function of both dopant type and amount.

Figures 4.10e,f show the XPS data for Ga2P_{3/2} as well as Mn2P_{3/2} and Mn2P_{1/2}, respectively. These data show that the valence of the Ga³⁺ precursor was increased fractionally upon heat treatment. However, the valence of the Mn²⁺ increased integrally, resulting in a mixture of Mn³⁺ and Mn⁴⁺, although the Mn₂O₃ peaks are at slightly lower binding energies than reported [100], suggesting a small valence reduction from Mn³⁺. The binding energy match for the Mn₃O₄ peaks suggests the dominance of the Mn²⁺ fraction of this species.

Figures 4.10g,h show that the trend (1-9 mol%) for both dopants was increasing binding energies and hence Ti valence, although it did decrease for 1GC. Since the valences of the dopants increased, then charge compensation is likely to have derived from Ce redox through intervalence charge transfer (IVCT)) with Ti³⁺ (1GC) and Ti⁴⁺ (other samples) [97-99], where integral valence is used for convenience:



Similarly, the valence increases from Ga doping would derive from the same mechanism:



Parenthetically, it is noted that Ga⁴⁺ is not cited for inorganic systems but it is well known in biological systems [442, 443]. Also, the effect of the increasing viscosity and resultant substrate coverage with increasing [Ga³⁺] of the precursor are confirmed by the decreasing XPS peak intensities for the Ga-doped films.

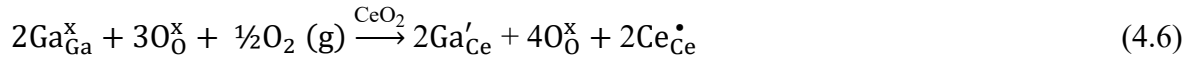
Although there does not appear to be a trend from Mn doping, the valence of the Mn^{2+} precursor increased upon heating treatment, which is consistent with the progressive IVCT reactions:



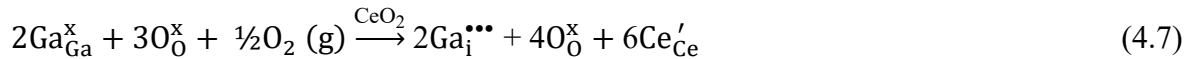
However, these preceding considerations lead to the conclusion that the $[\text{Ce}^{3+}]$ should increase. However, the data in **Figure 4.11** and **Table 4.5** show that the trends are the opposite. The interpretation of this lies in the Kröger-Vink [444] defect equilibria, which are:

Ga Doping

Substitutional Solid Solubility: $\text{Ce}^{3+} \rightarrow \text{Ce}^{4+}$ Redox (Oxidation) Charge Compensation



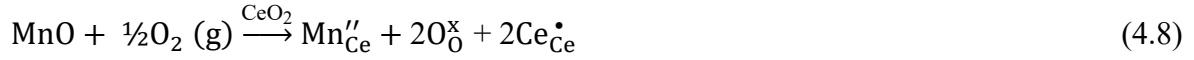
Interstitial Solid Solubility: $\text{Ce}^{4+} \rightarrow \text{Ce}^{3+}$ Redox (Reduction) Charge Compensation



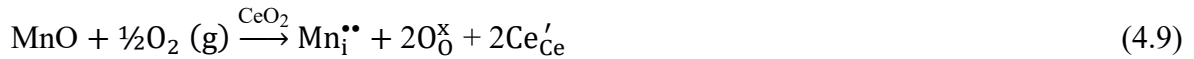
It may be noted that, when Kröger and Vink [423] developed their formalism for defect equilibria, XPS had not been invented, so they were not able to determine that charge compensation also could occur by redox since they did not have access to data confirming changes in valence upon doping.

Mn Doping

Substitutional Solid Solubility: $\text{Ce}^{3+} \rightarrow \text{Ce}^{4+}$ Redox Charge Compensation



Interstitial Solid Solubility: $\text{Ce}^{4+} \rightarrow \text{Ce}^{3+}$ Redox (Reduction) Charge Compensation

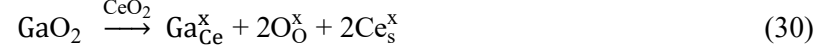


The XPS data show that the $[\text{Ce}^{3+}]$ initially increases and that, in general, there are decreasing trends as a function of dopant level. The initial increase occurs because, at the lowest dopant level, the amount of dopant ions is insufficient to result in homogeneous mixing, which destabilises the structure, thereby creating a non-representative increase in defect concentration [445, 446]. However, at higher dopant levels, the amount of dopant ions is sufficient to achieve homogeneous distributions, thereby revealing the trend in the data as a function of dopant level.

The XPS data can be explained through equations 4.6 and 4.8, which reflect both substitutional solid solubility and *redox* charge compensation, which favour the formation of Ce^{4+} . **Table 4.6** shows that the more conventional *ionic* or *electronic* charge compensation mechanisms are not possible because they cannot affect the $[\text{Ce}^{3+}]$. Further, the opposite effect of IVCT, which favours the formation of Ce^{3+} , is explained by the dominance of the defect equilibria because the latter involves the majority CeO_2 lattice and the former involves the minority dopants.

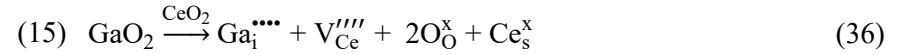
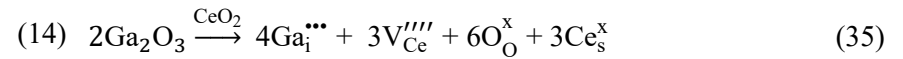
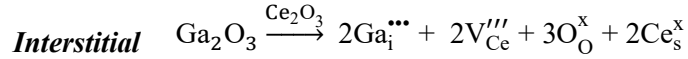
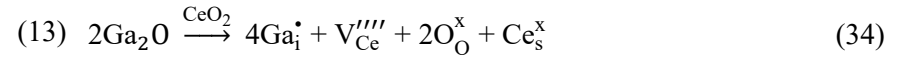
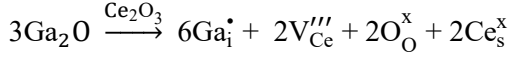
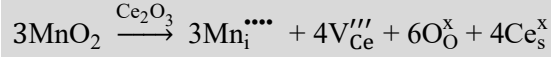
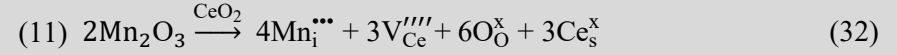
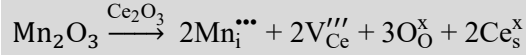
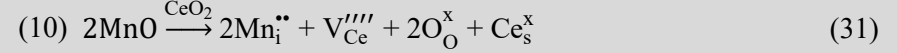
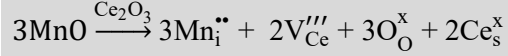
Table 4.6. *Potential defect equilibria for substitutional and interstitial solid solubilities and ionic and electronic charge compensation for both valences of matrix (Ce^{3+} , Ce^{4+}) and three valences of dopants (Mn^{2+} , Mn^{3+} , Mn^{4+}) and (Ga^{+} , Ga^{3+} , Ga^{4+})*

Potential Defect Equilibria			
	Ce^{3+}	Ce^{4+}	
Substitutional Solid Solubility	$2MnO \xrightarrow{Ce_2O_3} 2Mn'_{Ce} + V_O^{\bullet\bullet} + O_O^x + 2Ce_s^x + \frac{1}{2} O_2 (g)$	(1) $2MnO \xrightarrow{CeO_2} 2Mn''_{Ce} + 2V_O^{\bullet\bullet} + 2Ce_s^x + O_2 (g)$	(20)
	$Mn_2O_3 \xrightarrow{Ce_2O_3} 2Mn^x_{Ce} + 3O_O^x + 2Ce_s^x$	(2) $Mn_2O_3 \xrightarrow{CeO_2} 2Mn'_{Ce} + V_O^{\bullet\bullet} + 2O_O^x + 2Ce_s^x + \frac{1}{2} O_2 (g)$	(21)
	$3MnO_2 \xrightarrow{Ce_2O_3} 3Mn^{\bullet}_{Ce} + 6O_O^x + V'''_{Ce} + 3Ce_s^x$	(3) $MnO_2 \xrightarrow{CeO_2} Mn^x_{Ce} + 2O_O^x + Ce_s^x$	(22)
	$Ga_2O_3 \xrightarrow{Ce_2O_3} 2Ga^x_{Ce} + 3O_O^x$	(4) $Ga_2O_3 \xrightarrow{CeO_2} 2Ga'_{Ce} + V_O^{\bullet\bullet} + 2O_O^x + 2Ce_s^x + \frac{1}{2} O_2 (g)$	(23)
	$3GaO_2 \xrightarrow{Ce_2O_3} 3Ga^{\bullet}_{Ce} + 6O_O^x + V'''_{Ce} + Ce_s^x$	(5) $GaO_2 \xrightarrow{CeO_2} Ga^x_{Ce} + 2O_O^x + Ce_s^x$	(24)
	Electronic Charge Compensation	Electronic Charge Compensation	
	$2MnO + \frac{1}{2}O_2 (g) \xrightarrow{Ce_2O_3} 2Mn'_{Ce} + 3O_O^x + 2Ce_s^x + 2h^{\bullet}$	$MnO + \frac{1}{2}O_2 (g) \xrightarrow{CeO_2} Mn''_{Ce} + 2O_O^x + Ce_s^x + 2h^{\bullet}$	(25)
	$Mn_2O_3 \xrightarrow{Ce_2O_3} 2Mn^x_{Ce} + 3O_O^x + 2Ce_s^x$	(6) $Mn_2O_3 + \frac{1}{2} O_2 (g) \xrightarrow{CeO_2} 2Mn'_{Ce} + 4O_O^x + Ce_s^x + 2h^{\bullet}$	(26)
		(7) $MnO_2 \xrightarrow{CeO_2} Mn^x_{Ce} + 2O_O^x + Ce_s^x$	(27)
	$Ga_2O + O_2 (g) \xrightarrow{Ce_2O_3} 2Ga''_{Ce} + 3O_O^x + 2Ce_s^x + 4h^{\bullet}$	(8) $Ga_2O + 1\frac{1}{2}O_2 (g) \xrightarrow{CeO_2} 2Ga'''_{Ce} + 4O_O^x + 2Ce_s^x + 6h^{\bullet}$	(28)
	$Ga_2O_3 \xrightarrow{Ce_2O_3} 2Ga^x_{Ce} + 3O_O^x + 2Ce_s^x$	(9) $Ga_2O_3 + \frac{1}{2} O_2 (g) \xrightarrow{CeO_2} 2Ga'_{Ce} + 4O_O^x + 2Ce_s^x + 2h^{\bullet}$	(29)



Ionic Charge Compensation

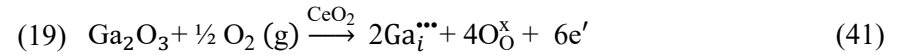
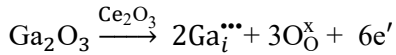
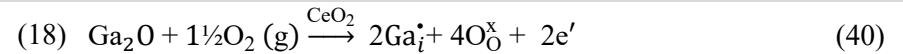
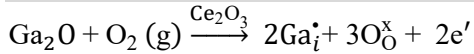
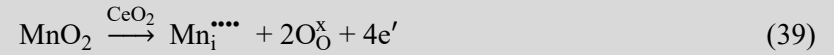
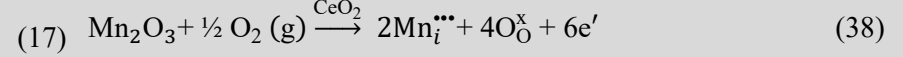
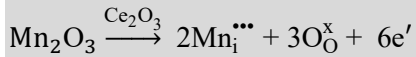
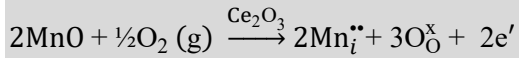
Ionic Charge Compensation



Solubility

Electronic Charge Compensation

Electronic Charge Compensation





Mn_{Ce}'	= Mn^{2+} substituting on Ce^{3+} site	(single negative charge)
Mn_{Ce}''	= Mn^{2+} substituting on Ce^{4+} site	(double negative charge)
Mn_{Ce}^x	= Mn^{4+} substituting on Ce^{4+} site	(no net charge)
$\text{Mn}_{\text{Ce}}^\bullet$	= Mn^{4+} substituting on Ce^{3+} site	(single positive charge)
$\text{Mn}_i^{\bullet\bullet}$	= Mn^{2+} interstitial	(double positive charge)
$\text{Mn}_i^{\bullet\bullet\bullet}$	= Mn^{3+} interstitial	(triple positive charge)
$\text{Mn}_i^{\bullet\bullet\bullet\bullet}$	= Mn^{4+} interstitial	(quadruple positive charge)
Ga_{Ce}'	= Ga^{3+} substituting on Ce^{4+} site	(single negative charge)
Ga_{Ce}''	= Ga^{+} substituting on Ce^{3+} site	(double negative charge)
Ga_{Ce}'''	= Ga^{+} substituting on Ce^{4+} site	(triple negative charge)
Ga_{Ce}^x	= Ga^{3+} substituting on Ce^{3+} site	(no net charge)
$\text{Ga}_{\text{Ce}}^\bullet$	= Ga^{4+} substituting on Ce^{3+} site	(single positive charge)
Ga_i^\bullet	= Ga^{+} interstitial	(single positive charge)
$\text{Ga}_i^{\bullet\bullet\bullet}$	= Ga^{3+} interstitial	(triple positive charge)
$\text{Ga}_i^{\bullet\bullet\bullet\bullet}$	= Ga^{4+} interstitial	(quadruple positive charge)
O_0^x	= Oxygen on lattice oxygen site	(no net charge)
$\text{O}_2(\text{g})$	= Oxygen gas	(no net charge)

Ce_s^x	= Ce migrated to surface	(no net charge)
V_{Ce}'''	= Ce^{3+} vacancy	(triple negative charge)
V_{Ce}''''	= Ce^{4+} vacancy	(quadruple negative charge)
$V_{\text{O}}^{\bullet\bullet}$	= O^{2-} vacancy	(double positive charge)
e'	= Electron	(single negative charge)
h^\bullet	= Electron hole	(single positive charge)

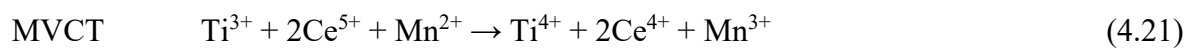
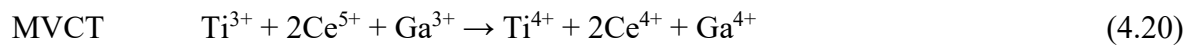
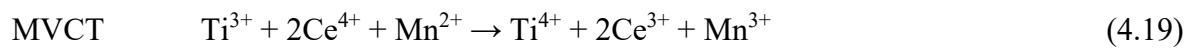
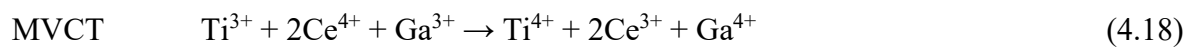
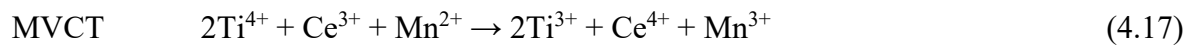
A further important point is that **Table 4.5** shows that the $[\text{Ce}^{3+}]$ values for all samples are inversely proportional to those for both the $[\text{Ga}]$ and $[\text{Mn}]$, which is to say that the dopant concentrations also are directly proportional to the $[\text{Ce}^{4+}]$ values. This is critical because these trends are consistent with Equations 4.6 and 4.8, which support the conclusion of substitutional solid solubility for both dopants.

It is possible that the preceding effects may be altered by the electronegativities of the ions. The relevant electronegativities (**Table 4.4**) for Ga^{3+} (1.70), Mn^{2+} (1.50), Mn^{3+} (1.85) and Mn^{4+} (unknown but >1.85) compared to those of Ce^{4+} (1.50) and Ce^{3+} (1.15) [430] indicate that bringing Ce^{4+} into proximity with Ga or Mn should decrease the valences of Ga and Mn, hence increasing the valence of Ce ($\text{Ce}^{3+} \rightarrow \text{Ce}^{4+}$). This is not the case with minority IVCT for both dopants but it is majority defect equilibria for 5GC, 9GC, and 5MC; it is not the case for 9MC. This latter irregularity suggests the electronegativity does not provide the dominant effect in the resultant valences. Further, since electronegativity is considered to provide the driving force for IVCT [447], then the contradictory data for IVCT suggests that electronegativity provides a minor, if any, role. Ultimately, it is likely that the inflection in the $[\text{Ce}^{3+}]$ with Mn doping is likely to reflect the competing mechanisms of IVCT, defect equilibria, and electronegativity.

In summary:

- The solubility mechanism is substitutional.
- The valence alterations revealed by XPS result from IVCT, which favours $\text{Ce}^{4+} \rightarrow \text{Ce}^{3+}$ reduction; this is a minor effect as it is associated with the dopants.
- The charge compensation mechanism is redox, which results in decreasing $[\text{Ce}^{3+}]$ owing to $\text{Ce}^{3+} \rightarrow \text{Ce}^{4+}$ oxidation; this is a majority effect as it is associated with the CeO_2 matrix.
- Electronegativity has only a small, if any, effect.

Although the preceding discussion referred only to IVCT, which involves only two cations (film matrix and dopant), there is the potential for charge transfer from the third ion present in the system, which is the Ti^{4+} of the substrate. In this case, the interaction of three ions would involve multivalence charge transfer (MVCT) [448]. In effect, the potential role of MVCT represents a fourth factor affecting the valence alterations. A summary of the potential IVCT and MVCT reactions is as follows:



These reactions are summarised in abbreviated form in Figure 4.12.

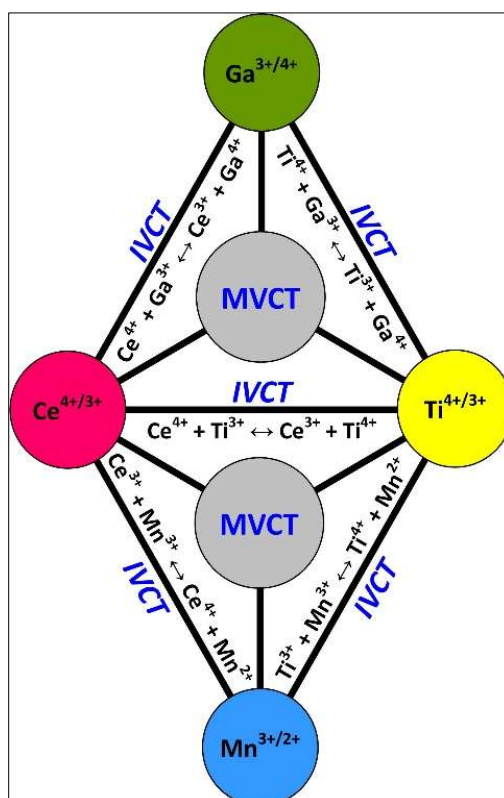


Figure 4.12. Representative IVCT reactions and integrated role of MVCT reactions for Ga-doped and Mn-doped CeO₂ thin films deposited on Ti-based substrates

4.3 Summary and Conclusions

The present work reports the fabrication of CeO₂ thin films (~820 nm thickness), doped with 0-9 mol% Ga or Mn, spin coated on rough 3D-printed Ti6Al4V, followed by calcination at 650°C for 2 h. The films were characterised microstructurally by TEM and FESEM, topographically by 3D laser scanning confocal microscopy, mineralogically by GAXRD, and surface chemically by XPS. The data reveal that three extrinsic factors provided the dominant effects on the resultant data:

Solution Viscosities: The greater viscosity of the Ga-based solution precursor resulted in the deposition of a more continuous surface layer, which effectively reduced the roughness and attenuated the X-ray beam. The lower viscosity of the Mn-based solution precursor filled the irregularities of the rough 3D printed Ti6Al4V substrate, which had the converse effect.

Lattice Contraction: The GAXRD data indicated that both Ga and Mn doping caused lattice contraction. This is consistent with an increase in Ce valence, which contradicts the XPS data.

Intervalence Charge Transfer: The general decrease in $[\text{Ce}^{3+}]$ is consistent the electron exchange between dopant and film matrix ions, where the increasing valence of the dopants were balanced by the decreasing valence of Ce. However, as this effect is associated with the dopants, it is a minority effect.

Substitutional Solid Solution: Hume-Rothery's rules and the GAXRD data are consistent with substitutional solid solubility for both dopants.

Redox Charge Compensation: The defect equilibria for substitutional (or interstitial) solid solubility with ionic or electronic charge compensation cannot explain the changes in $[\text{Ce}^{3+}]$. Therefore, the charge compensation mechanism must be redox. Further, the general decreasing trend in $[\text{Ce}^{3+}]$ is explained only by the defect equilibria for substitutional solid solubility, thus confirming the solid solubility mechanism. Finally, as defect equilibria are for the matrix, this provides a majority effect. Consequently, this explains why the contradictory IVCT, which increases the $[\text{Ce}^{3+}]$, does not provide the dominant effect.

Electronegativity: This factor plays a minor, if any role. However, it plays a more important function in initiating the mechanisms of IVCT.

Multivalence Charge Transfer: The combined electron exchanges between film matrix, dopants, and Ti substrate provides a fourth potential factor affecting the nature of the resultant valences of the ions, in addition to IVCT, defect equilibria, and electronegativity.

5. Results and Discussion – Biological Performance

One of the most common means of addressing issues of bacterial infection and osseointegration is implant modification by the application of a surface coating, which must meet a number of requirements [10]. One of these is the nature of the targeted bacteria and whether they are gram-positive or gram-negative. **Figure 5.1** illustrates the structural differences between these two, where gram-negative bacteria possess an encapsulating outer lipid membrane that acts as an impenetrable and protective cell wall (outer membrane) while the cell wall of gram-positive bacteria does not provide this protection, so they are easier to destroy [449]. A second important difference is the thickness and structure of the cell wall. In gram-positive bacteria, the cell wall consists of a multiple mesh-like layers of a polymeric peptidoglycan layer and it is of thickness 20-80 nm [216]. In gram-negative bacteria, this is comprised of a single less-robust mesh-like peptidoglycan layer of thickness 1.5-10 nm, the outer membrane, and attached lipopolysaccharides.

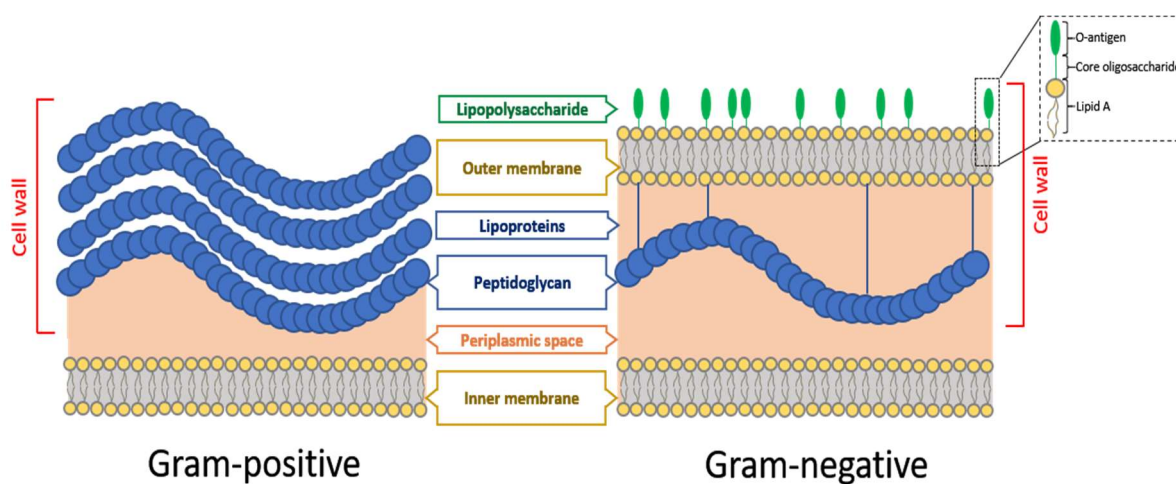


Figure 5.1. Structural differences between the cell walls of gram-positive and gram-negative bacteria

Although bacteria are of both gram-positive and gram-negative types, all bacteria exhibit varying degrees of negative surface charges owing to the double cell membrane or, in the case of the single

cell membrane, the inner membrane plus the negatively charged teichoic acids (phosphate-based carbohydrates) linked to the apposed peptidoglycan [450]. In effect, most bacteria are discouraged from adhering to negatively charged surfaces. In gram-negative bacteria, the lipopolysaccharide layer also contributes to the negative surface charge owing to the uronic acid residue in the lipopolysaccharide O-side chain [451]. The rigidity of this layer stabilises and protects the cell wall, so gram-negative bacteria, such as *E. coli*, are more resistant to penetration than are gram-positive bacteria, such as *S. aureus* [452, 453].

Victor *et al.* [454] examined the gram-reaction and associated surface electrical charge of bacteria by applying an electric current and confirmed that both gram-positive and gram-negative bacteria carry a negative surface charge. They also showed that the electrophoretic velocity and associated surface charge can be altered and even reversed through pH change, regardless of the gram-reaction [455, 456]. However, comparative experimental work on the electrophoretic mobilities of gram-positive *S. aureus* and gram-negative *E. coli* revealed that the surface charge of the former is less negative than that of the latter [452, 453].

5.1 Antibacterial Assays

Figure 5.2 shows the percentage of bacterial reduction in the presence of CeO₂ films with varying Ga-doping (**Figure 5.2a**) and Mn-doping (**Figure 5.2b**) levels, percentage of bacterial adhesion with varying Ga-doping (**Figure 5.2c**) and Mn-doping (**Figure 5.2d**) levels with respect to the uncoated (control) sample against *S. aureus* and *E. coli*. Each point represents the mean number of viable counts for three samples. The error bars give the standard deviations. The survival rates are given in **Figure 5.2e**.

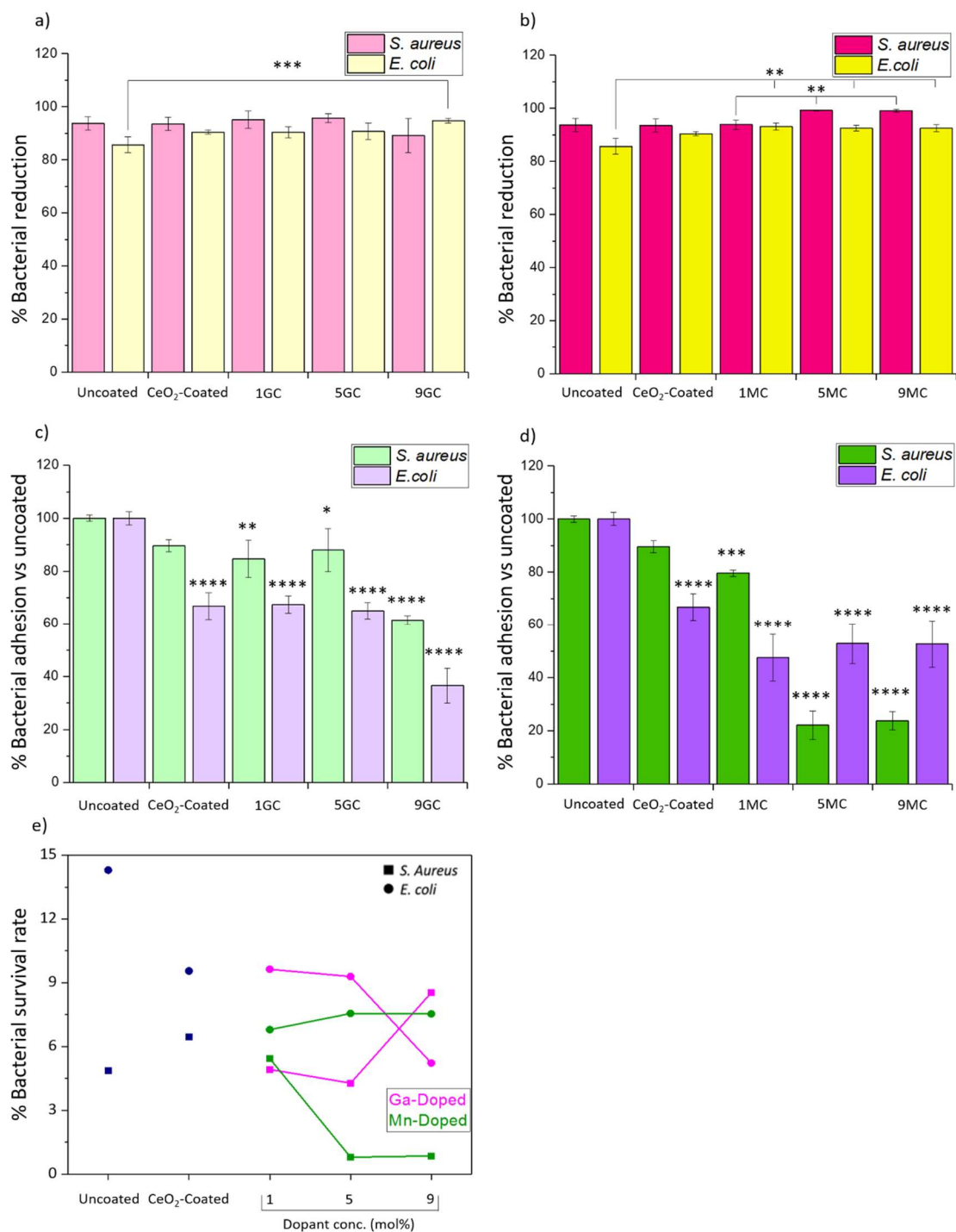


Figure 5.2. *S. aureus* and *E. coli* bacterial reduction: (a) Ga-doped samples, (b) Mn-doped samples, *S. aureus* and *E. coli* bacterial adhesion (relative to control (uncoated sample): (c) Ga-doped samples, (d) Mn-doped samples, (e) *S. aureus* and *E. coli* bacterial survival rates after 24 h incubation (bacterial concentration = CFU/mL; * $p < 0.05$, ** $p < 0.01$, *** $p < 0.001$, and **** $p < 0.0001$)

Figure 5.2a reveals that all the undoped and Ga-doped samples have the antibacterial performances higher than ~86% against both *S. aureus* and *E. coli* but the individual data are not statistically distinguishable. This effectiveness may reflect the chemical similarities between Ga^{3+} and Fe^{3+} and the bacterial inability to differentiate these ions in the relevant metabolic processes [457]. Considering only the average values in **Figure 5.2a**, the following trends are suggested:

- The thin films generally were more effective in killing *S. aureus* than *E. coli*, although 9GC was a clear exception.
- Increasing Ga doping levels generally increased the bactericidal effects for both bacteria, although 9GC again was a clear exception.
- There was little difference in the bactericidal effects against *S. aureus* between the uncoated control and the CeO_2 -coated samples, with 9GC again being an exception.
- There was a greater improvement in bactericidal effects against *E. coli* between the uncoated control and the CeO_2 -coated samples.
- The only statistically significant difference ($p < 0.001$) was the greater bactericidal effect against *E. coli* for 9GC (94.8%) relative to the uncoated control (90.4%).

Figure 5.2b reveals that all the Mn-doped samples exhibit antibacterial performances greater than ~92% against both *S. aureus* and *E. coli* with two statistically distinguishable data pairs. Again, considering just the averages, the following trends are suggested:

- The thin films generally were more effective in killing *S. aureus* than *E. coli*.
- Increasing Mn doping levels generally increased the bactericidal effects for *S. aureus* at significant differences ($p < 0.01$) for both 5MC and 9MC relative to 1MC, although the bactericidal activity against *E. coli* remained unchanged with increasing Mn level.

- There were significant differences ($p < 0.01$) in the bactericidal effects against *E. coli* between the uncoated sample and all of the Mn-doped samples.
- There was a slight improvement in bactericidal effects against *E. coli* for the Mn-doped samples relative to the CeO₂-coated sample.

Figures 5.2c and 5.2d show the percentages of bacteria adhered to the surfaces of the samples relative to that of the uncoated sample. All the samples revealed significant improvements in bactericidal activity against both *S. aureus* and *E. coli* relative to the uncoated sample. Again, considering only the averages, the following trends are suggested:

- Relative to the uncoated sample, the bactericidal activity of the samples against both *S. aureus* and *E. coli* was enhanced, although *E. coli* showed a lower affinity toward the GC-doped samples compared to that of *S. aureus*.
- Increasing the Ga dopant level decreased the bacterial adhesion for both *S. aureus* and *E. coli*; 9GC exhibited the best performances against both bacteria.
- All of the samples revealed statistically significant differences ($p < 0.0001$) relative to the uncoated sample except for the CeO₂-coated sample against *S. aureus* and 1GC ($p < 0.01$) and 5GC ($p < 0.05$) against *S. aureus*.
- The MC-doped samples revealed a trend opposite to that of the GC-doped samples, where the former exhibited superior antibacterial performance against *S. aureus*.
- With increasing MC doping, the bacterial adhesion decreased significantly relative the uncoated sample ($p < 0.0001$), although 1 MC was slightly out of trend ($p < 0.001$).
- With increasing MC doping, the bacterial adhesions showed reverse trends for the two bacteria, where *S. aureus* decreased and *E. coli* increased.

The survival rates of the bacteria, shown in Figure 5.2e, were calculated according to:

$$\frac{CFU_{24\text{ h}}}{CFU_{0\text{ h}}} \times 100 \quad (5.1)$$

where $CFU_{24\text{ h}}$ is the number of colonies of surviving bacteria on the sample after 24 h incubation and $CFU_{0\text{ h}}$ is the number of colonies of bacteria before incubation.

These data allow the following conclusions to be made:

- The data for the uncoated and CeO_2 -coated samples show that, in common with other comparative studies [409, 458, 459], the killing of gram-positive *S. aureus* was more effective than that of gram-negative *E. coli*, suggesting that both the substrate and CeO_2 coating were negatively charged.
- Plakhova *et al.* [460] have shown that the isoelectric point of CeO_2 is at pH 6.3, where more acidic conditions establish a positive surface charge (*viz.*, Ce^{4+}) and more basic conditions establish a negative surface charge (*viz.*, Ce^{3+}).
- The data for the uncoated and CeO_2 -coated samples also show that CeO_2 coating causes the surfaces to become less negatively charged, where the killing of gram-positive *S. aureus* was less effective by the substrate but the killing of gram-negative *E. coli* by the substrate was more effective.
- With Ga doping and gram-positive *S. aureus*: While Ga doping caused both the roughness and $[Ce^{3+}]$ to decrease, the bacterial survival rates relative to the CeO_2 -coated sample were not consistent, decreasing for 1GC and 5GC and increasing for 9GC. This is interpreted in terms of three variables. For 1GC, the roughness data in **Figure 4.3a** indicate that the negatively charged Ti alloy asperities [461] provide the dominant effect. For 5GC, the same data indicate again that the roughness and Ti alloy surface charge are relevant but that the former provides the dominant effect. For 9GC, which exhibited the greatest coverage of the Ti alloy substrate, the significant increase and reversal in trend in bacterial survival rate for gram-positive *S. aureus* are consistent

with the dominant roles of negatively charged Ce^{3+} , where the $[\text{Ce}^{3+}]$ was the lowest value for the doped samples (**Table 4.5**).

- With Ga doping and gram-negative *E. coli*: In comparison to the CeO_2 -coated sample, the bacterial survival rates for the gram-negative *E. coli* were only slightly changed for 1GC and 5GC, suggesting only minor if any effect of roughnesses, $[\text{Ce}^{3+}]$, and Ti alloy asperities. However, for 9GC, the bacterial survival rate for gram-negative *E. coli* was decreased significantly, suggesting that the low roughness and low $[\text{Ce}^{3+}]$ are relevant. In light of the similarities in trends in bacterial survival rates for the Mn-doped samples (discussed subsequently), it is probable that the $[\text{Ce}^{3+}]$ provides the dominant effect.
- With Mn doping and gram-positive *S. aureus*: The bacterial survival rates relative to the CeO_2 -coated sample were decreased significantly. Critically, they correlate closely with both the roughnesses (**Figure 4.3a**) but they exhibit a reverse correlation with $[\text{Ce}^{3+}]$ (**Table 4.5**), where the negative Ce^{3+} surface would be expected to kill gram-positive *S. aureus* but the opposite occurred. Consequently, the direct role of the roughness is indicated. However, Mn_3O_4 was present in increasing amounts with increasing $[\text{Mn}]$ as a precipitate in all three samples. Although this precipitation is a reflection of the defect equilibria, the presence of the precipitates is considered an independent variable that is deleterious to bacterial survival, although this effect is minor.
- With Mn doping and gram-negative *E. coli*: In comparison to the CeO_2 -coated sample, the bacterial survival rates for the gram-negative *E. coli* also were decreased, which indicates that the surface charge through the $[\text{Ce}^{3+}]$ does not provide the dominant effect. The bacterial survival also does not correlate with the roughness (**Figure 4.5a**), so this also is not a dominant effect. In contrast, the slight increase in bacterial survival correlates with the Mn_3O_4 precipitation (**Figure 4.10**), which is consistent with its negative surface charge [462, 463].

The last point is not surprising since both sample roughness and wetting also influence the bacterial response. However, the importance of the role of $\text{Ce}^{4+} \leftrightarrow \text{Ce}^{3+}$ redox and $\text{V}_\text{O}^{\bullet\bullet}$ generation in the formation and elimination of ROS is well known [464]. Hence, the initiation of the mechanism of the killing of *S. aureus* and *E. coli* is suggested by the IVCT process indicated in Equations 4-6 and 19-21, which provides the means by which Ga and Mn doping cause the $\text{Ce}^{3+} \leftrightarrow \text{Ce}^{4+}$ redox, as well as the direct generation of $\text{V}_\text{O}^{\bullet\bullet}$ indicated by Equations 4.7 and 4.13. Perhaps more significantly, these analyses suggest the significant role of the $[\text{Ce}^{3+}]$ in the homogeneous Ga-doped CeO_2 solid solutions and how small changes of as little as 1 at% can exert a very dominant effect on bacterial survival rates. In contrast, for the inhomogeneous Mn-doped samples, all three main factors appear to play roles simultaneously.

In addition to the three discussed variables of roughnesses, $[\text{Ce}^{3+}]$, and Ti alloy asperities, the fourth variable of the $[\text{Ga}]$ or $[\text{Mn}]$ also must be considered. The data in **Figure 5.2e** indicate that there is no clear correlation between bacterial survival rates and dopant concentration. If this were the case, then similar general trends for both gram-positive and gram-negative bacteria, which was not the case. In fact, opposite trends generally were observed. Further, **Table 2.5** shows that both ions are known to exhibit antibacterial activity, so only decreasing trends in survival rates would be expected, again not the case. Consequently, this variable cannot be decoupled from the other three. However, in the case of Ga doping, the effectively mirror images of the trends suggest the critical role of $[\text{Ce}^{3+}]$. In the case of Mn doping, the absence of parallel or mirror image trends is indicative of the contributions of multiple effects, although the $[\text{Mn}]$ does not appear to be dominant.

5.2 Acellular Mineralisation (Apatite Formation)

The outcomes of the investigation of the capacity of the samples to facilitate HA formation *in vitro* by immersion in SBF are revealed in the GAXRD patterns of **Figure 5.3**; these data are summarised

in **Table 5.1**. FESEM images after immersion in SBF for 2 weeks and 1 month are shown in **Figure 5.4**. The main conclusions from these data are as follows:

CeO₂-Coated

The reversal in the major phase from CeO₂ (2 weeks) to α -Ti suggests that, in the absence of HA peaks, (1) amorphous HA preferential precipitates on the α -Ti and/or (2) SBF enhances the precipitation of CeO₂. Although the FESEM images (**Figures 5.4a-d**) confirm the formation of HA, the absence of a hump at $\sim 32^\circ 2\theta$ in the GAXRD data (**Figure 5.3a**) suggests that the former is the case.

Ga-Doped (1GC, 5GC, 9GC)

- 1GC shows attenuation the GAXRD intensities for both CeO₂ and α -Ti, again in the absence of HA peaks. There also is an unidentified peak at $\sim 45^\circ 2\theta$, which does not correspond to any Ce-based or Ti-based phases or Ce titanites. The observation of HA in the FESEM images (**Figures 5.4e and 5.4f**), in conjunction with the GAXRD data, support the view that amorphous HA precipitates on both phases. This indicates that Ga doping at this low level enhances HA precipitation on CeO₂.
- 5GC at only 1 month shows the maximal HA (211) peak only. It is unexpected that no peaks of minor intensity are apparent. Although this could be a result of preferred orientation, the (211) generally does not exhibit this [465]. However, it is known that increasing crystallinity increases the intensity of the (211) while the intensities of the neighbouring strong (112) and (300) peaks decrease [466]. However, it is most likely that the single HA peak observed on these uneven samples is not the (211) peak ($31.8^\circ 2\theta$) but the (300) peak ($32.9^\circ 2\theta$), which is known to occur with little indication of minor peaks [467]. The range of locations of this peak in the present work was $31.50 - 33.03^\circ 2\theta$. As the peak intensities of α -Ti increased but those of CeO₂

decreased, this supports the conclusion that Ga doping enhances HA precipitation on CeO₂. However, the role of time in increasing precipitation is clear. The FESEM images (**Figures 5.4g** and **5.4h**) reveal the precipitation of HA at both 2 weeks and 1 month (at greater levels than for 1GC), so the former would involve amorphous HA and the latter crystalline HA.

- 9GC at both 2 weeks and 1 month shows that the amount of Ga doping is relevant in that increasing [Ga] increases the extent of HA precipitation. The ready precipitation at this [Ga] results in peak intensity decrease for both α -Ti and CeO₂. What appears to be the same unidentified peak at $\sim 45^\circ 2\theta$ is present. The FESEM images (**Figures 5.4i** and **5.4j**) reveal high levels of HA, which confirms the effect of both [Ga] and time in enhancing HA precipitation. However, as with 1GC and 5GC, the extent of coverage of the surface by HA is incomplete.

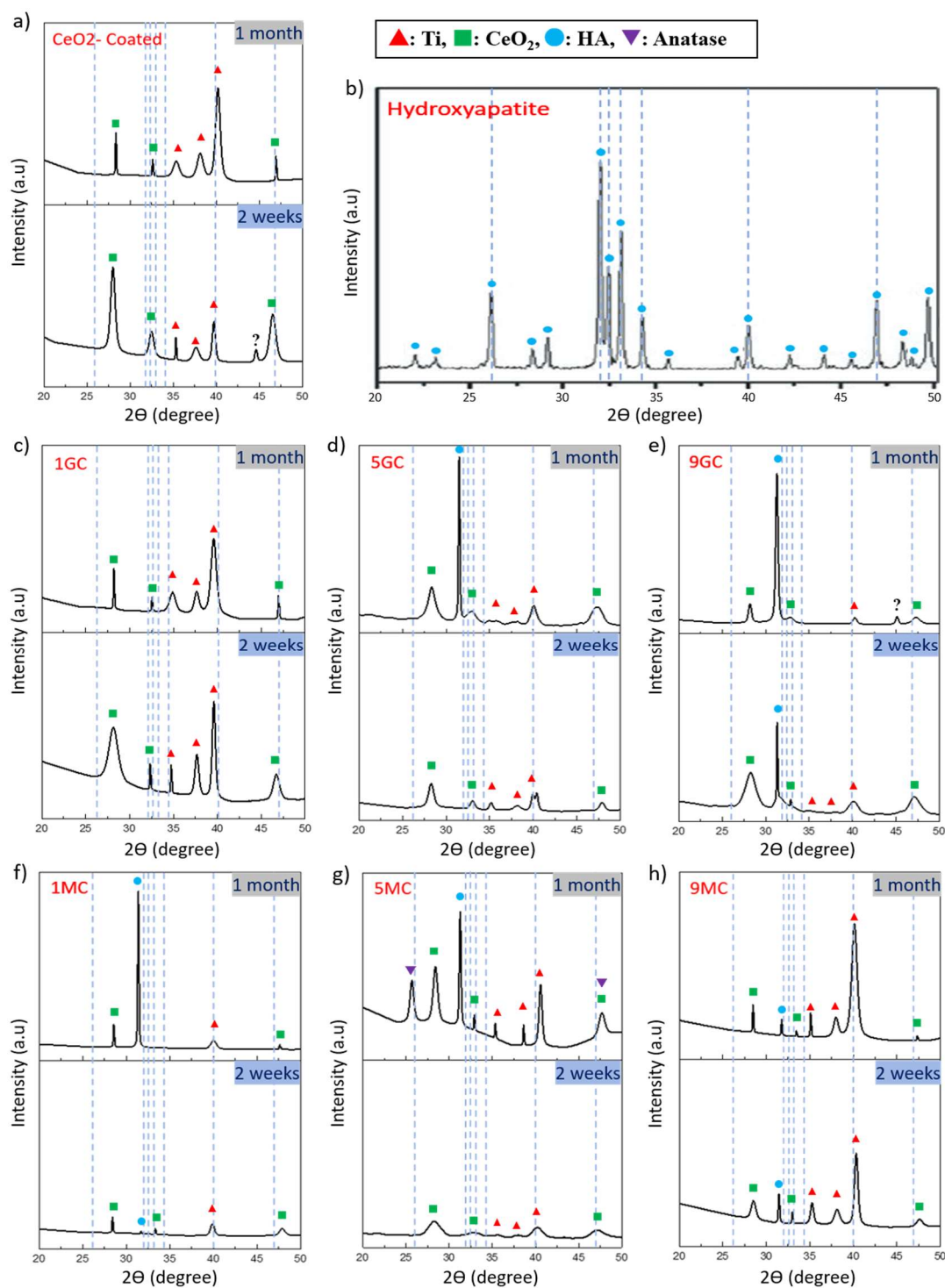


Figure 5.3. GAXRD patterns (intensities scaled identically) of: (a) CeO_2 -coated substrate, (b) HA reference peaks according to ICDD 01-074-0565, (c-e) Ga-doped CeO_2 coatings, (f-h) Mn-doped CeO_2 coatings; calcined at 650°C for 2 h followed by immersion in 200 mL SBF solution for 2 weeks or 1 month

Table 5.1. *Relative proportions of thin film phases following soaking in SBF based on maximal GAXRD peak heights*

Sample	Phase							
	Major		Substantial		Minor		Trace	
	2 weeks	1 month	2 weeks	1 month	2 weeks	1 month	2 weeks	1 month
CeO₂-Coated	CeO ₂	α -Ti	α -Ti	CeO ₂	--	--	Unknown	--
1GC	α -Ti	α -Ti	CeO ₂	CeO ₂	--	--	--	--
5GC	CeO ₂	HA	α -Ti	--	--	CeO ₂ α -Ti	--	--
9GC	HA	HA	--	--	α -Ti	CeO ₂	--	α -Ti Unknown
1MC	CeO ₂ α -Ti	HA	--	--	HA	CeO ₂	--	α -Ti
5MC	CeO ₂ α -Ti	HA	Amorphous	CeO ₂ α -Ti Anatase	--	--	--	--
9MC	α -Ti	α -Ti	--	--	HA CeO ₂	CeO ₂ HA	--	--

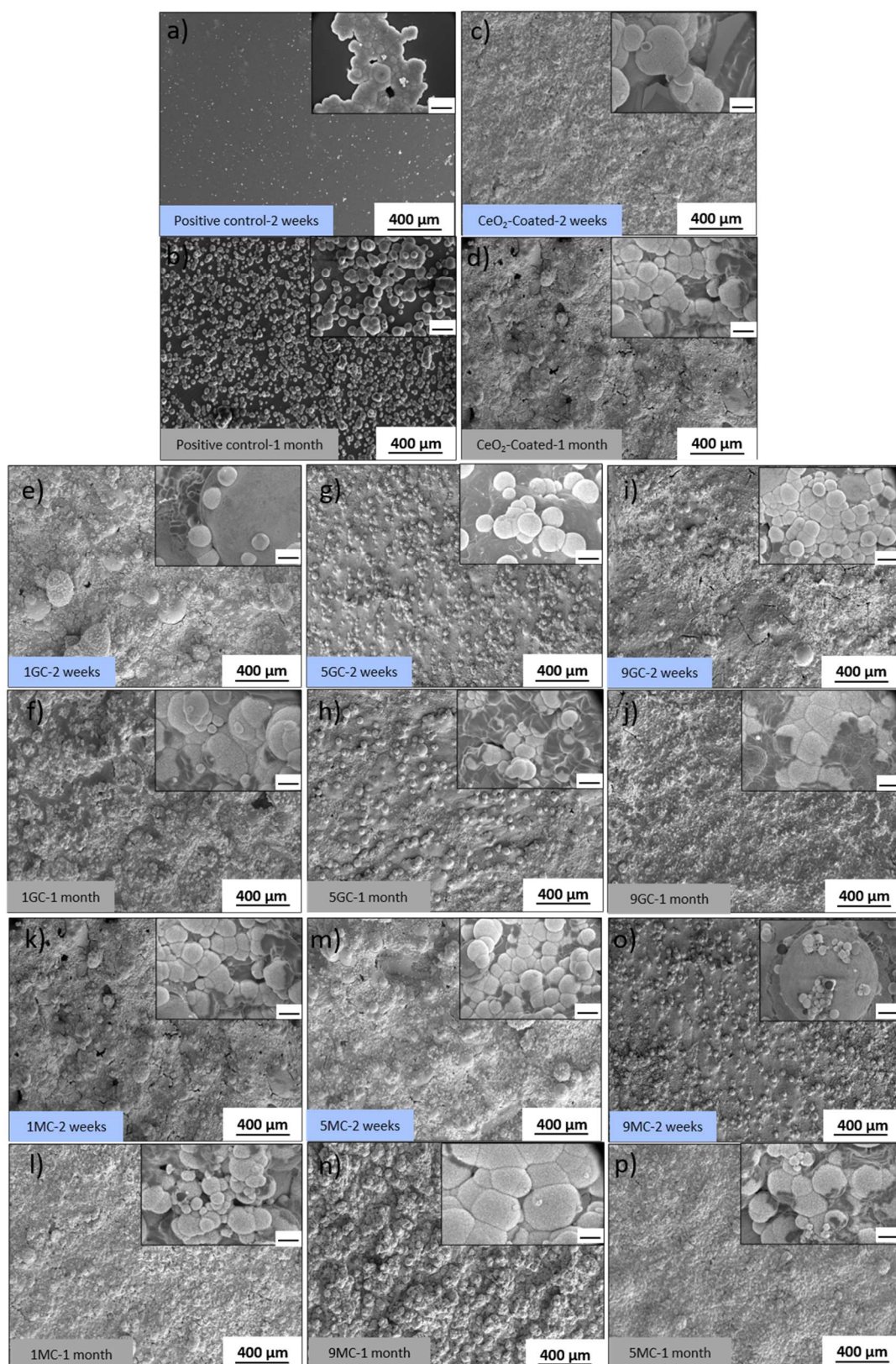


Figure 5.4. FESEM images of HA precipitation after immersion in SBF for 2 weeks or 1 month: (a,b) positive control, (c,d) CeO₂-coated, (e,f) 1GC, (g,h) 5GC, (i,j) 9GC, (k,l) 1MC, (m,n) 5MC, (o,p) 9MC; calcined at 650°C (insets: 10 μm scale bar)

Mn-Doped (1MC, 5MC, 9MC)

- 1MC reveals low GAXRD intensities (**Figure 5.3f**) and the FESEM images show a high level of coverage by HA (**Figure 5.4k**). These data confirm that precipitated HA is amorphous and that time converts it to crystalline. This is a well-known phenomenon, where the amorphous species is amorphous calcium phosphate (ACP) [468-470]
- 5MC at 2 weeks is similar to 1MC at the same time point both in terms of mineralogy (**Figure 5.3g**) and microstructure (**Figure 5.4m**). However, at 1 month, the results are completely different. These data reveal the presence of well crystallised HA and anatase; the GAXRD peak intensities for CeO₂ and α -Ti also are increased. There also is a broad amorphous hump centred under the HA peak. These results are interpreted in terms of attenuation of the GAXRD peak intensities by amorphous HA (**Figure 5.4n**), its increased crystallinity over time (**Figure 5.3g**), and increased exposure of the underlying substrate owing to decreased volume and shrinkage of HA upon recrystallisation. Although the location of the amorphous hump would suggest that it is HA, this is not supported by its absence in all other GAXRD patterns and the decrease in amorphous HA at 1 month. Consequently, this amorphous phase remains unidentified. The cause of formation of anatase also remains unknown. In light of the number of anomalies that are not consistent with other samples, it is concluded that this sample is not representative of the phenomena and that this probably lies in an unknown processing variation.
- 9MC at both 2 weeks and 1 month reveal the negative impact of the [Mn] on the precipitation of HA (**Figure 5.3h**); this is confirmed by the microstructures (**Figures 5.4o** and **5.4p**), which indicate a lower HA distribution density than for 5MC.

The preceding discussion leads to the conclusions that precipitation is enhanced by (1) increasing [Ga], decreasing [Mn] concentration (but not nil [Mn]), and increasing time.

Another factor that may be relevant is the surface roughness, which has been observed before, where the asperities provide high-surface-energy nucleation sites for HA precipitation [471]. However, comparison with the roughness data in **Figure 4.3a** reveals no apparent correlation. Another possible factor investigated in the present work is the $[\text{Ce}^{3+}]$ values, which are shown in **Table 4.5**. These data show that, for the doped samples, increasing [Ga] and [Mn] both decrease $[\text{Ce}^{3+}]$. However, the GAXRD data (**Figures 5.3c-h**) show that increasing [Ga] in these homogeneous solid solutions enhanced HA formation but increasing [Mn] in these inhomogeneous samples had the reverse effect. From this, it is concluded that [Ga] and HA formation were inversely proportional, where the Ce^{3+} acts as a nucleation site, but that this effect was not observed in the Mn-doped samples owing to their inhomogeneity and lower solubility levels, as evidenced by the formation of precipitates.

5.2.1 SBF

The interaction of the films with SBF was investigated by analysing the residual solutions after film immersion for 2 weeks and 1 month. The [Ce], [Ga], and [Mn] are shown in **Figures 5.5a-c**, respectively. These data show that Ce is only slightly soluble in SBF, which has been observed before [472]. Both Ga and Mn show increasing solubilities of the dopant ions with increasing dopant concentrations, which is expected. However, Ga is considerably more soluble, which also has been noted previously [473]. **Figure 5.5b** shows that the solubility of Ga increased significantly with time, which is consistent with the GAXRD data in **Figures 5.3c-e**. That is, increasing coverage by HA over time reduced the free film surface subject to leaching by SBF and the corresponding Ga solubility. The Mn solubility, which has been observed before [474 - 476], is substantially less than that of Ga, decreasing only slightly over time. The GAXRD data for 9MC in **Figure 5.3h** show that crystalline HA is present at a low level and the FESEM data. The probable reason for this is that examination of **Figures 5.3f-h** for 2 weeks immersion shows that the amount of HA was

significant only for 9MC while the converse was the case for 1 month immersion. These trends suggest that the apparently anomalous data in **Figure 5.5c** results from the initial blockage by HA after 2 weeks immersion and deterioration of the HA (from the high [Mn]) after 1 month immersion. **Figure 5.6a** confirms the anomalous nature of 5GC by the observation that the [Ce] for this sample was off-scale.

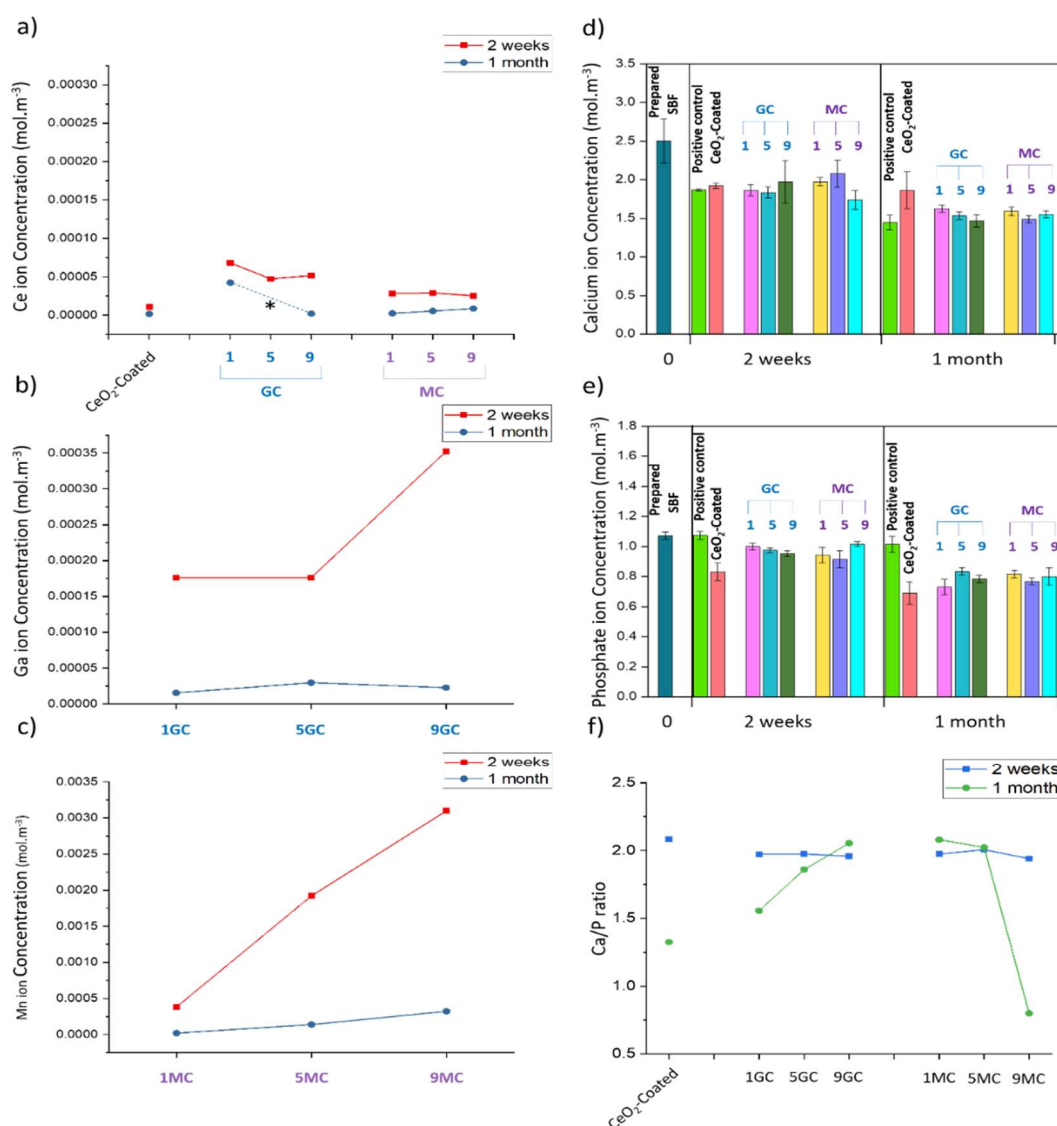


Figure 5.5. ICP-OES results for ionic concentrations of residual SBF after immersion for 2 weeks or 1 month: (a) Ce, (b) Ga, (c) Mn (single-point data) and (d) Ca, (e) P (multiple-point data), (f) Ca/P ratio; calcined at 650°C for 2 h (* for 5GC (a) was off-scale)

Figures 5.5d and **5.5e** contrast the initial [Ca] and [P] with those after immersion for the undoped and doped films; the data for the positive control also are included.

Positive Control

These data appear to be anomalous in that, while the [Ca] exhibited the expected decrease with immersion, the [P] remained effectively unchanged. The positive control was Unigraft, which is a bioactive and resorbable bioglass with principal components Ca, P, and Si. The explanation for this lies in the FESEM images, which show highly agglomerated particles after 2 weeks immersion but individual and slightly agglomerated particles of the same (individual) grain size after 1 month immersion. These images indicate that the resorbable bioglass was deagglomerated over time, suggesting resorption by the SBF. Consequently, there are two competing diffusion mechanisms, where HA formation diffuses Ca and P to the bioglass and bioglass resorption diffuses Ca and P into the SBF. **Figure 5.6** shows the peak-containing section of the GAXRD pattern. Although the indexing is uncertain, there appears to be α -quartz and HA, although these are represented by only single peaks. Three other peaks could not be assigned to any of the common phases that precipitate from silicate glasses [477], form by reaction between the bioglass and SBF [478], or precipitate from SBF [479 - 483].

In the latter case, it has been established that the precipitation of HA from bioglass does not necessarily follow the stoichiometric Ca/P ratio of 1.67 for HA ($\text{Ca}_{10}(\text{PO}_4)_6(\text{OH})_2$). Consequently, the approximately constant [P] is likely to have resulted from the establishment of interfacial chemical equilibrium between P released from the bioglass and its immediate incorporation in the adjacent HA, leaving the [P] of the surrounding SBF unchanged. Since the [Ca] in the residual SBF decreased, this equilibrium would not apply to this ion and so the rate of deposition of Ca was

greater than that of P transfer. It is probable that the commencement stage of deposition of Ca from the SBF initiated the transfer of P from the bioglass. The summary data in **Figure 5.5f** show that the Ca/P varied significantly between time points, which is consistent with the differential Ca deposition (fast) and P transfer (slow) rates.

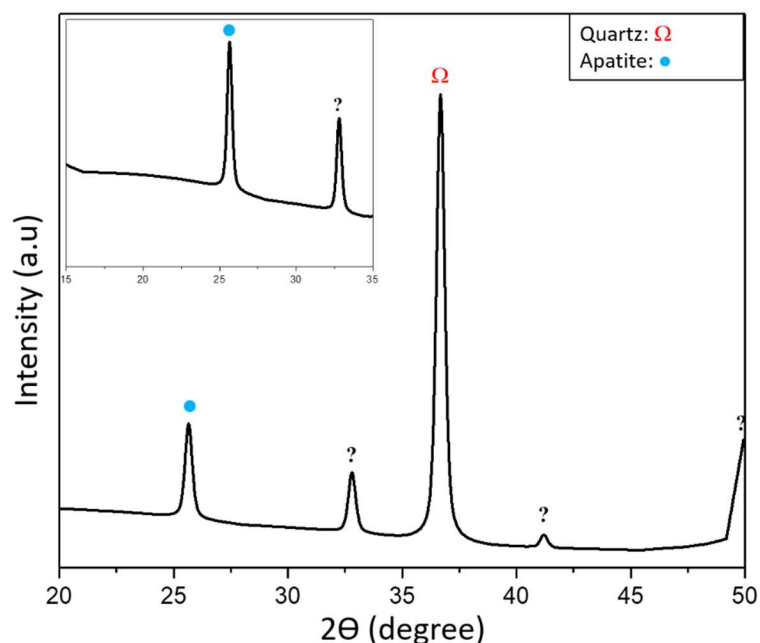


Figure 5.6. GAXRD pattern of positive control after immersion in 200 mL in SBF for 1 month; powder sample placed on glass substrate (inset shows the amorphous hump at $\sim 23^\circ 2\theta$ / 0.387 nm)

CeO₂-Coated

The CeO₂-coated films showed more conventional behaviour, where both the [Ce] and [P] decreased in response to the precipitation of HA. In this case, **Figure 5.5f** reveals that the Ca/P remained constant between time points, thus suggesting a single precipitation mechanism (from SBF), in contrast to the positive control. Comparison of these two sets of data is informative in that both show that, compared to the SBF composition, the Ca/P ratio in the residual SBF increased, meaning that it decreased in the HA. This comparison confirms that the deposition rate of Ca from

SBF is greater than that of transfer of P from the bioglass but that the deposition rate of P from SBF is equivalent to that of Ca.

Ga-Doped (1GC, 5GC, 9GC)

Figures 5.5d and **5.5e** show that, compared to the CeO₂-coated films, the residual [Ca] after 2 weeks immersion was the same but that, after 1 month, the residual [Ca] decreased. At the same time, the residual [P] was higher after 2 weeks but it was approximately unchanged after 1 month. However, **Figure 5.5f** shows that the Ca/P ratio remained approximate constant for 1GC, 5GC, and 9GC at both time points. These data reflect the difference in Ca/P ratios between the CeO₂-coated films and the Ga-doped films; they also show that the HA deposits from SBF in a consistent manner. Ultimately, it is apparent that Ga doping does not affect the Ca/P ratio.

Mn-Doped (1MC, 5MC, 9MC)

The data for the Mn-doped films are essentially the same as those for the Ga-doped samples, with the exception of 9MC after 2 weeks immersion. Here, the residual [Ca] was lower and the residual [P] was higher than those for the CeO₂-coated films. This probably resulted from the low amount of precipitated HA, as indicated in **Figure 5.3h**. Consequently, the reason for this differential is not clear. For both the Ga-doped and Mn-doped films, the Ca/P ratios of the residual SBF were lower than those for the CeO₂-coated films, meaning that they were higher in the HA precipitates. Consequently, it is clear that both dopants effectively increased the Ca/P ratios in the HA films relative to those of the CeO₂-coated films. Although not overt in Figure 5.6f, there appears to be a slight decreasing Ca/P trend with increasing dopant level, thus further supporting this conclusion. The cause of this is unlikely to be the effect of dissolved Ga and Mn because **Figures 5.5b** and **5.5c** reveal that the solubilities of the two ions are considerably different. It is possible that lattice distortion from the dopant dissolution alters the lattice parameters, thus cause lattice strain in the

precipitated HA to be compensated by alteration of the Ca/P ratio. This has been shown to be the case elsewhere [483-486].

5.3 Cell Adhesion and Proliferation Assays

The results of cell adhesion and cell viability, which were assessed *in vitro* by the MTS assay, are shown in **Figure 5.7**; FESEM micrographs at the 4 h and 2 day time points are shown in **Figure 5.8**. The data in **Figure 5.7** reveal the following:

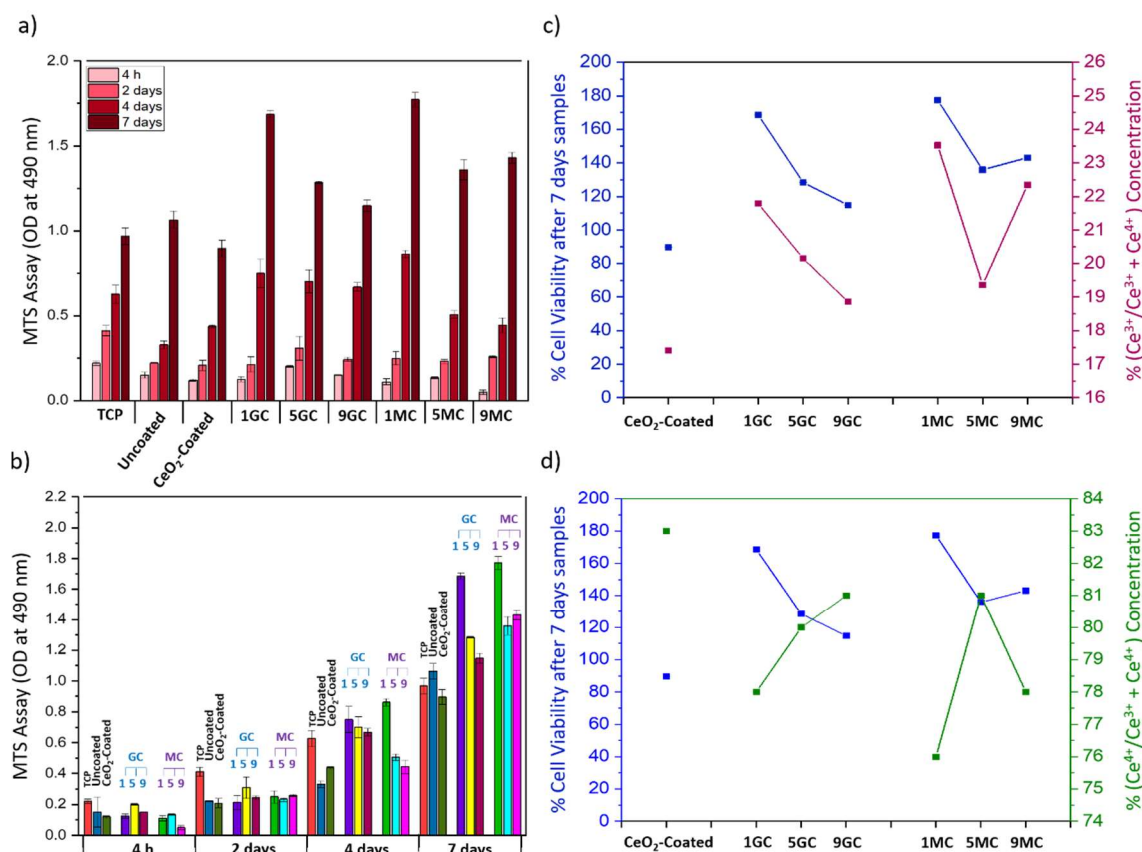


Figure 5.7. (a) and (b) Cell attachment and proliferation of MG-63 cells cultured up to 7 days on: TCP, uncoated, CeO₂-Coated, Ga-doped CeO₂ coated, and Mn-doped CeO₂ coated substrates analysed by the MTS assay (OD at 490 nm), and (c) and (d) effects of dopants on cytotoxicity values (for samples cultured for 7 days) and [Ce] from XPS data.

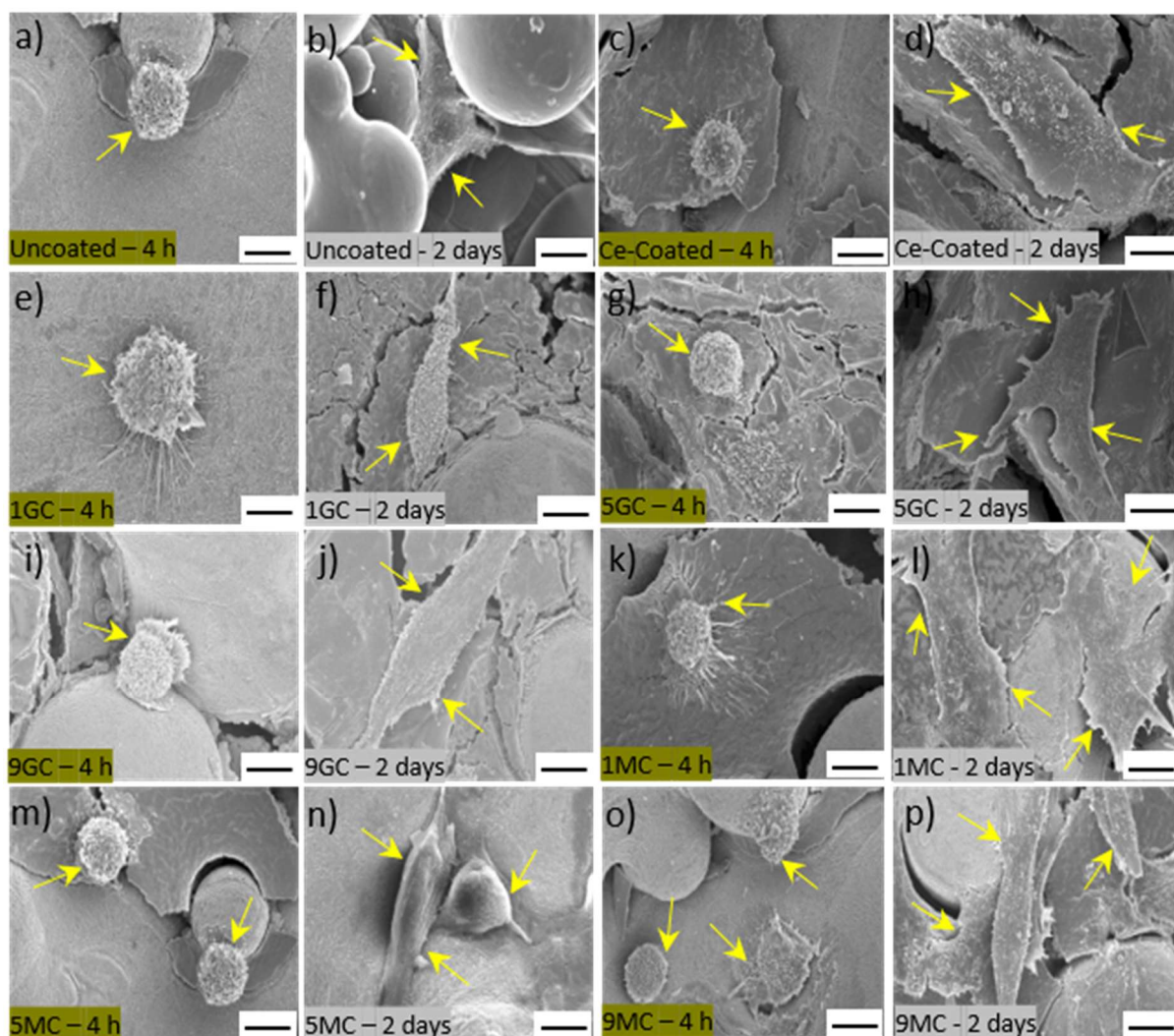


Figure 5.8. FESEM images of cell attachment (4 h) and cell proliferation (2 days) following seeding by MG-63 cells on the substrates for: (a,b) uncoated, (c,d) CeO₂-coated, (e-j) Ga-doped CeO₂-coated, and (k-p) Ga-doped CeO₂-coated substrates (10 μ m scale bar)

Figure 5.7a

- The numbers of cells increased for all of the samples up to 7 days. Of these, 1MC and 1GC reached the highest levels of cell numbers. The relative peak heights show that the dose dependence is the most significant factor and that the type of dopant is secondary. Although other studies confirm the priority of the dose dependence [93, 487-489], there do not appear

to be any other studies allowing comparison with the type of dopant. The probable reason for this is that Mn is a natural component of bone [490] while this is not the case for Ga .

- The CeO₂-coated sample exhibited much lower numbers of cells, even lower than those for TCP and the uncoated sample. Consequently, it is clear that CeO₂ is not favoured by osteoblastic-like cells but that minor amounts of Ga and Mn alter this significantly.
- The dose dependency is emphasised by the different trends for the increasing dopant levels, where Ga decreased regularly while Mn exhibited a minimum. **Table 4.5** reveals the great significance of [Ce³⁺] in that these two trends are duplicated.
- The trend of cell numbers was descending for Ga-doped samples as a result of increasing the [Ga]. However, Mn revealed a little different trend, with the lowest cell numbers at 5 mol % and slightly increased at 9 mol%, which was still lower than that of for 1 mol%.

Figure 5.7b

- 4 h: At the shortest time point, there is little differentiation between samples, with the exception of the statistically significant difference ($p < .001$) between TCP and 9MC, where the latter supports the conclusion of the dose dependency of the growth and associated attachment delay for this biological cation. However, the similarity of the other data support the view that there is a significant chemistry dependence.
- 2 days: The cell growth increased only marginally at this time point, including 9MC. This is unusual in that it is normal for the cell growth to double at this time point [491]. These data emphasise the primacy of the chemistry dependence at the shorter time points during the growth phase.
- 4 days: There are several statistically significant differences:
 - (1) The 1MC (highest) and uncoated (lowest) samples relative to TCP exhibited the greatest difference ($p < .0001$).

- (2) 1GC, 5GC, 9GC, and 1MC were extremely increasing relative to the uncoated and CeO₂-coated samples ($p < .0001$).
- (3) 5MC was very significantly increasing relative to the uncoated sample ($p < .01$).
- (4) The CeO₂-coated sample and 9MC also were very significantly decreasing relative to TCP ($p < .01$).

These data confirm that doping improved the cell proliferation over that of CeO₂. They also confirm the dose dependency of the cell proliferation, which was more significant Mn compared to Ga. This observation indicates that, even though Mn is intrinsic to bone, there is an overdoped point of diminishing returns.

- 7 days: There are several statistically significant differences:

- (1) All of the doped samples were extremely increasing relative to TCP and the CeO₂-coated samples ($p < .0001$).
- (2) 1GC, 5GC and all the Mn-doped samples were extremely increasing relative to the uncoated sample ($p < .0001$).
- (3) The CeO₂-coated sample was very significantly decreasing relative to the uncoated sample ($p < .01$).

All but one of the samples, even the uncoated sample, revealed improvements in cell proliferation. The single exception was the CeO₂-coated sample. Although this showed the least cell proliferation, the OD still increased fivefold over that at 4 h. These data highlight the primary of the dose dependency on cell proliferation rather than the chemistry (which better reflects the cell growth).

Figure 5.7c

- All of the samples exhibited cell viabilities >86%, which are significantly greater than the commonly accepted benchmark of 70% (EN ISO 10993-5: 2009) for acceptable cell viability [492-494].
- The data for $[\text{Ce}^{3+}]$ in **Table 4.5** are repeated here and contrasted with those for cell viability after 7 days. The close parallels are clearly apparent, where both (specific) chemistry dependence and dose dependence are clear.
- The chemistry dependence is revealed by the slightly superior performance of the Mn-doped samples. The dose dependence is revealed by the initial increase (from undoped) and the subsequent decreases with increasing dopant concentration.
- The overall dependency on the $[\text{Ce}^{3+}]$ is revealed by the parallels in the data for cell viability.

Figure 5.7d

- These data for $[\text{Ce}^{4+}]$ show converse trends of those of $[\text{Ce}^{3+}]$ for the reason that these data are normalised to 100% from the respective XPS peak areas.
- These data are presented in order to emphasise the role of ROS generation in reducing the cell viability, as exemplified by, for example:



It is common practice to attribute these effects to the role of $\text{V}_\text{O}^{\bullet\bullet}$ and to equate the $[\text{V}_\text{O}^{\bullet\bullet}]$ with one half the $[\text{Ce}^{3+}]$ [446, 495]. Further, it is implicit that these interpretations assume substitutional solid solubility and ionic charge compensation. However, the present work, using XPS data and defect equilibria, demonstrates that ionic charge compensation is not the case and that redox charge compensation from substitutional solid solubility and IVCT (with perhaps a small influence from

electronegativity) are the main affecting factors. Therefore, the addition of acceptor dopants, such as Mn^{2+} , Mn^{3+} , and Ga^{3+} , cannot generate oxygen vacancies. Instead, they generate Ce^{3+} , which can be determined directly by XPS. The data in **Figure 5.7c** confirm the critical importance of Ce^{3+} as it provides a direct reflection of its dominant influence on the cell viability, where this ion is beneficial.

The images in **Figures 5.8a-p** reveal that all the substrates supported the initial cellular attachment after 4 h, followed by cellular extension and continuous growth during the following 2 days. After 2 days, the cells had become interconnected, as indicated by the elongated lamellipodia, which are common features of MG-63 cells [496].

Importance of $\text{Ce}^{3+} \leftrightarrow \text{Ce}^{4+}$ Redox

The cytoprotective capacity of ceria derives mainly from the continuously reversible $\text{Ce}^{3+} \leftrightarrow \text{Ce}^{4+}$ redox switching, which regulates the ROS level [497]. That is, ceria acts as an antioxidant by scavenging the ROS at basic physiological pH, thereby protecting normal cells, while, ceria acts as a prooxidant by generating ROS at acidic tumour microenvironment (TME) pH, thereby killing cancerous cells [498, 499]. Equation 2.3 illustrates the relevance of the $\text{Ce}^{3+} \leftrightarrow \text{Ce}^{4+}$ equilibria to the generation or scavenging of ROS. A critical consideration is the valence implications of this redox switching [497], where it is known that the $[\text{Ce}^{3+}]$ is higher in basic physiological pH while $[\text{Ce}^{4+}]$ is higher in acidic TME [500].

6. Summary and Conclusions

For the porous films of ceria doped with 1, 5, or 9 mol% Ga or Mn, spin coated on rough Ti6Al4V substrates, **Table 6.1** contrasts the combinations of factors that affect the bacterial survival and cell viabilities.

Table 6.1. *Summative comparison of data*

Sample Parameter	CeO ₂ - Coated	Ga-Doped			Mn-Doped		
		1GC	5GC	9GC	1Mn	5Mn	9Mn
Bacterial Survival (Gram +)	6.4	4.9	4.2	8.5	5.4	0.8	0.9
Bacterial Survival (Gram –)	9.2	9.6	9.2	5.2	6.8	7.5	7.5
Cell Viability	90	169	129	115	177	136	143
Wettability	High	High	Medium	Low	High	High	High
Ra Roughness (μm)	14	17	13	5	25	12	11
[Dopant] from Doping	0	1	5	9	1	5	9
[Dopant] from Precipitation	--	Nil	Nil	Nil	Low	Medium	High
[Dopant] from Viscosity	--	Low	Medium	High	Low	Low	Low
Surface [Ce³⁺] (at%)	17	22	20	19	24	19	22
Subsurface [Ce³⁺] (at%)	26	26	13	14	31	17	24

With increasing [Ga], the increasing viscosity led to greater continuity of the film as a coating; with increasing [Mn], a reverse but reduced effect was observed, so the substrate asperities remained discrete projections above all of the films. Consequently, the dopant concentrations to which the bacteria and cells were exposed were a function of the dopant concentration (from doping), the area

of exposed film surrounding the projecting asperities (from viscosity), and oxide precipitation (from precipitation). For Ga doping, the first two trends were in parallel (precipitation was absent) but, for Mn doping, the increasing trends from doping and precipitation did not match the constancy of film exposure resulting from the lower viscosity relative to that of for Ga doping.

The final variables examined were surface and subsurface $[\text{Ce}^{3+}]$. For Ga doping, the trend for the surface $[\text{Ce}^{3+}]$ was the reverse of that expected from the dopant concentration, indicating that this parameter is controlled by Ce redox and IVCT (Equation 4.3). For Mn doping, the trend revealed a minimum in $[\text{Ce}^{3+}]$, suggesting differential effects, which result from overdoping and the introduction of a second solubility mechanism. Further contributions could derive from IVCT between film and substrate and/or surface broken bonds vs lattice bonds. For both Ga doping and Mn doping, the subsurface $[\text{Ce}^{3+}]$ reflects the competition between surface broken bonds vs lattice bonds and the interaction between the film and substrate.

Bacterial Survival Rates

All of the films exhibited superior bactericidal activity against *S. aureus* (gram-positive) compared to that against *E. coli* (gram-negative). As stated, this suggests that the surface charge of all of the films is negative, which indicates the dominant effect on the bacteria of Ce^{3+} over that of Ce^{4+} , despite the fact that $[\text{Ce}^{4+}] > [\text{Ce}^{3+}]$ (**Table 6.1**). Further, the bactericidal activity of Mn generally was superior to that of Ga.

The bacterial survival rates depend on the combined effects of the variables roughness, $[\text{Ce}^{3+}]$, Ti alloy surface charge from the asperities, and dopant concentration. For the homogeneous solid solutions 1GC and 5GC, the effects of both roughness and Ti alloy surface charge dominated while 9GC was dominated by the low $[\text{Ce}^{3+}]$ owing to the greater coverage of the Ti alloy substrate. For

the inhomogeneous Mn-doped samples and gram-positive *S. aureus*, the dominant effects of roughness and negatively charged Mn_3O_4 were apparent. For gram-negative *E. coli*, the only notable effect was that of the low roughness and low $[\text{Ce}^{3+}]$ for 9MC.

Acellular Mineralisation

The results for HA formation were distinctive, yielding Ca/P ratios in the general range ~ 1.6 - 2.1 . Following soaking in SBF for 2 weeks or 1 month, no HA formation on the CeO_2 -coated samples was observed. In contrast, the presence of the homogeneous Ga-doped CeO_2 solid solution enhanced HA formation considerably, where it was clear that the $[\text{Ga}]$ was proportional to the extent of HA formation. In contrast, the Mn-doped samples showed the reverse trend. These differences are attributed to the role of $[\text{Ce}^{3+}]$, where the extent of HA formation on the homogeneous Ga-doped solid solutions is inversely proportional to the $[\text{Ce}^{3+}]$, which may act as a nucleation site. This effect was reversed for the inhomogeneous Mn-doped samples.

Cell Viability

The direct relation between cell attachment and proliferation and the $[\text{Ce}^{3+}]$ was overt, where both undoped and doped samples exhibited direct correlations between these factors. Further, the bioactivity increased in the order CeO_2 -coated < Ga-doped < Mn-doped. The interpretation of these data is distinctive in light of the fact that the defect equilibria indicate the absence of a role for oxygen vacancies. As stated previously, essentially all of the reports of the effects of Ce redox on cell interactions attribute the resultant effects to oxygen vacancies, the formation of which is assumed to result from $\text{Ce}^{4+} \rightarrow \text{Ce}^{3+}$ reduction and charge compensation. In the present work, this assumption has been shown to be unjustified, leading to the conclusion that the dominant effect derives of the surface $[\text{Ce}^{3+}]$.

Ceria has recently shown cytoprotective capacity, which derives from continuously reversible $\text{Ce}^{4+} \leftrightarrow \text{Ce}^{3+}$ redox switching. Its properties are altered readily through its considerable capacity for solid solution formation. However, the state of understanding of the associated mechanisms are not well understood. The present work addresses these issues through a doping study using two therapeutic ions, Ga (as proxy for Fe) and Mn (as enzymatic systems regulator). All the samples exhibited the bactericidal effect as well as bone cell adhesion and proliferation owing to the dominant effect of Ce^{3+} in alteration the surface charge. The most important finding of the present work is that the widely assumption of oxygen vacancy effect is unjustified, and the dominant effect derives from the surface $[\text{Ce}^{3+}]$.

The objectives of the present work were threefold: (a) to use Ga or Mn doping to alter the nature of CeO_2 thin films deposited on Ti6Al4V biomedical-grade 3D printed substrates, (b) to examine the effects of the doping on the physical properties of the films, and (c) to examine the effects of the doping on the biological properties of the films.

The outcomes of the present work highlight a number of new findings that are of relevance to orthopaedic implants. First, the solubility mechanisms of Ga and Mn in CeO_2 have been deduced. Second, the simultaneous examination of these two dopants, as opposed to the more typical examination of a single dopant, allows the decoupling of many of the associated phenomena. Third, data analysis that combines XPS data with defect equilibria is revealed to be a powerful tool to determine solid solubility mechanisms, charge compensation mechanisms, the formation of different defect types, and their roles in the performance of materials. Fourth, the anomalous data (5MC vs 9MC) clarify the potential for a change in solid solubility mechanism and the resultant charge compensation mechanism as a function of dopant level. Fifth, the bacterial survival rates, acellular mineralisation, and cell viability are strongly dependent on the $[\text{Ce}^{3+}]$ rather than the

widely accepted $[V_O^{\bullet\bullet}]$. Sixth, the cytotoxicity derives from formation of ROS, which results directly from $Ce^{3+} \rightarrow Ce^{4+}$ oxidation rather than the widely accepted role of catalytic activation by the $V_O^{\bullet\bullet}$. The present work highlights a number of conclusions that can be made on the basis of the data analysis. First, the solubility mechanisms of Ga and Mn in CeO_2 have been considered. Second, the simultaneous examination of these two dopants, as opposed to the more typical examination of a single dopant, allows the decoupling of many of the phenomena. Third, data analysis that combines XPS data with defect equilibria is shown to be a powerful tool to determine solid solubility mechanisms, charge compensation mechanisms, the formation of different defect types, and their roles in the performance of materials. Fourth, anomalous data (5MC vs 9 MC) elucidate the potential for a change in solubility mechanism and resultant charge compensation mechanisms as a function of dopant level. Fifth, the bacterial survival rates, acellular mineralisation, and cell viability are strongly dependent on the $[Ce^{3+}]$, not the $[V_O^{\bullet\bullet}]$. Sixth, cytotoxicity derives from formation of reactive oxygen species (ROS), which results from $Ce^{3+} \rightarrow Ce^{4+}$.

6.1 Research Recommendation

The cellular responses and antibacterial performances of biomedical Ti6Al4V alloy coated with CeO₂ doped by Ga or Mn was investigated using cell viability testing and the colony-forming unit method, respectively. These studies highlight the conclusion that these doped coatings can enhance the bioactivity of the implant significantly relative to that of undoped CeO₂. However, in order to determine the effects of surface chemistry on protein adsorption, it is necessary to undertake protein depletion serum studies. Further, other relevant information potentially assays. Also, although there is an infinite variety of chemical, structural, mineralogical, and microstructural features, systematic studies of any of these may lead to other useful conclusions concerning the applicability of such materials. Finally, in addition to the preceding *in vitro* approaches, similar strategies could be applied to *in vivo* approaches, particularly in terms of histomorphometric analyses for morphological analyses of tissues and immunohistological staining for analyses of the activities of osteogenic cells

References

1. Whitlow, J., Paul, A., and Polini, A., Bioactive materials: definitions and application in tissue engineering and regeneration therapy. *Biocompatible Glasses: From Bone Regeneration to Cancer Treatment*. pp 1-17 (2016).
2. Ratner, B. D. and Bryant, S. J., Biomaterials: where we have been and where we are going. *J. Annual Review of Biomedical Engineering*,. **6**, pp 41-75 (2004).
3. Hench, L. L. and Thompson, I., Twenty-first century challenges for biomaterials. *J. Royal Society Interface*,. **7**(4) pp S379-91 (2010).
4. M. Kaur, K. Singh, Review on titanium and titanium based alloys as biomaterials for orthopaedic applications, *Mater Sci Eng C Mater Biol Appl*, 102 (2019) 844-862.
5. Singh, J. N., et al., Effect of surface roughness on titanium medical implants. *J. Nanostructured Materials and their Applications* , Springer Singapore, Singapore (2021).
6. Gianfreda, F., et al., Microscopic characterization of bioactivate implant surfaces: increasing wettability using salts and dry technology. *J. Materials*, 14(10), pp 2608, (2021).
7. Nobles, K. P., et al., Surface modifications to enhance osseointegration–Resulting material properties and biological responses. *J. Biomedical Materials Research*, **109**, pp 1909 - 1923, (2021)
8. Zareidoost, et al., , The relationship of surface roughness and cell response of chemical surface modification of titanium. *J. Materials Science: Materials in Medicine*, **23**, pp 1479-1488, (2012).
9. Pesode, P., and Barve, S., Surface modification of titanium and titanium alloy by plasma electrolytic oxidation process for biomedical applications: A review. *J. Materials Today: Proceedings*, **46**(1), pp 594-602, (2021).
10. Raphel, J., et al., Multifunctional coatings to simultaneously promote osseointegration and prevent infection of orthopaedic implants. *J. Biomaterials*,. **84**, pp 301-314 (2016).
11. Nouri, A., and Wen, C., Introduction to surface coating and modification for metallic biomaterials. *J. Surface Coating and Modification of Metallic Biomaterials*, pp. 3-60 (2015).
12. Garg, H., et al., Implant surface modifications: A review, *Journal of Clinical and Diagnostic Research*, **6**, pp 319-324 (2012).
13. Khong, Y. J., et al., Effect of plasma treatment on metal oxide p–n thin film diodes fabricated at room temperature. *J. Advanced Materials Interfaces*, **8**(10), (2021).
14. Guo, T., Orchestrating soft tissue integration at the transmucosal region of titanium implants. *J. Acta Biomaterialia*, **124**, pp 33-49 (2021).
15. Torres-Avila, I. P., et al., Surface modification of the Ti-6Al-4V alloy by anodic Oxidation and its effect on osteoarticular cell proliferation. *J. Coatings*, **10**(5), pp 491, (2021).
16. Lin, C.Y.W., et al., Effect of Fe doping on TiO₂ films prepared by spin coating, *J. Ceramics International*, **38**, pp 3943-3946 (2012).
17. Doran, N., et al., Photocatalytic antimicrobial films on fluorinated contact lens polymers, *Materials Letters*, **212**, pp 134-138 (2018).
18. Shokri, N., et al., Enhanced corrosion protection of NiTi orthopedic implants by highly crystalline hydroxyapatite deposited by spin coating: The importance of pre-treatment. *J. Materials Chemistry and Physics*, **259**, pp 124041, (2021).
19. Benharrat, L., et al., Preparation and characterization of luminescent YPO₄: Eu³⁺ thin films using sol gel spin coating method, *J. Thin Solid Films*, **694** (2020).

20. Azadani, R. N., et al., Sol-gel: Uncomplicated, routine and affordable synthesis procedure for utilization of composites in drug delivery. *J. Composites and Compounds*, **3**(6), pp 57-70 (2021).
21. Kılınç, A.Ç., et al., Characterization of eggshell-derived hydroxyapatite on Ti6Al4V metal substrate coated by sol–gel method. *J. Australian Ceramic Society*, **57**, pp 47–53 (2021).
22. Abbas, A., et al., Atomic layer deposited TiO₂ films on an equiatomic NiTi shape memory alloy for biomedical applications. *J. Alloys and Compounds*, **886**, pp 161282 (2021)..
23. Ahmadi, R., et al., *In vitro* study: Evaluation of mechanical behavior, corrosion resistance, antibacterial properties and biocompatibility of HAp/TiO₂/Ag coating on Ti6Al4V/TiO₂ substrate. *J. Surfaces and Interfaces*, **24**, pp 101072.
24. Jing, Z., et al., Corrosion, wear and biocompatibility of hydroxyapatite bio-functionally graded coating on titanium alloy surface prepared by laser cladding. *J. Ceramics International*, **47**(17), pp 24641-24651.
25. Sartori, M., et al., Nanostructure and biomimetics orchestrate mesenchymal stromal cell differentiation: An *in vitro* bioactivity study on new coatings for orthopedic applications. *J. Materials Science and Engineering: C*, **123**, pp 112031.
26. Gu, H., et al., Bioactivity and biocompatibility of porous gradient bioceramic coating prepared *via* laser cladding process. *J. Surface and Coatings Technology*, **426**, pp 127800.
27. Hodásová, L., et al., 3D-Printed Polymer-Infiltrated Ceramic Network with Biocompatible Adhesive to Potentiate Dental Implant Applications. *J. Materials*, **14**(19), pp 5513.
28. Wang, B., et al., Surface modification of titanium implants by silk fibroin/Ag co-functionalized strontium titanate nanotubes for inhibition of bacterial-associated infection and enhancement of *in vivo* osseointegration. *J. Surface and Coatings Technology*, **405**, pp 126700, (2021).
29. Qingge, W., et al., Nanostructured titanium alloys surface modification technology for antibacterial and osteogenic properties. *J. Current Nanoscience*, **17**(19), pp 175-193(2021).
30. Zhu, G., et al., Advances in implant surface modifications to improve osseointegration. *J. Materials Advances*, **2**, pp 6901-6927, (2021).
31. Stich, T., et al., Implant-bone-interface: Reviewing the impact of titanium surface modifications on osteogenic processes *in vitro* and *in vivo*. *J. Bioengineering & Translational Medicine*, **7**(1), pp e10239, (2022).
32. Saldarriaga, I. C., et al., *In vitro* and *in vivo* comparisons of staphylococcal biofilm formation on a cross-linked poly(ethylene glycol)-based polymer coating, *J. Acta Biomaterial*, **6**, pp1119-1124, (2010).
33. Chen, S., et al., Synthesis of hierarchical and flower-like TiO₂ nanowire microspheres as biocompatible cell carriers. *J. Materials Science and Engineering: C*, **126**, pp 112118, (2021).
34. Qadir, M., et al., Surface characterization and biocompatibility of hydroxyapatite coating on anodized TiO₂ nanotubes via PVD magnetron sputtering. *J. American Chemical Society*, **37**(16), pp 4984-4996, (2021).
35. Hayles, A., et al., Hydrothermally etched titanium: a review on a promising mechano-bactericidal surface for implant applications. *J. Materials Today Chemistry*, **22**, pp 100622, (2021).

36. Kreller, T., et al., Biomimetic calcium phosphate coatings for bioactivation of titanium implant surfaces: Methodological approach and *in vitro* evaluation of biocompatibility. *J. Materials*, **14**(13), pp 3516, (2021).
37. Crouzier, T., et al., Layer-by-layer films as a biomimetic reservoir for rhBMP-2 delivery: controlled differentiation of myoblasts to osteoblasts, *J. Small*, **5**, pp 598-608, (2009).
38. Lohberger, B., et al., Surface modifications of titanium aluminium vanadium improve biocompatibility and osteogenic differentiation potential. *J. Materials*, **14**(6), pp 1574, (2021).
39. Atkinson, I., et al., Preparation and biocompatibility of poly methyl methacrylate (PMMA)-mesoporous bioactive glass (MBG) composite scaffolds. *J. Gels*, **7**(4), pp 180, (2021).
40. Li, H., et al., Nutrient alloying elements in biodegradable metals: a review. *J. Materials Chemistry B*, **9**, pp 9806-9825, (2021).
41. Che, J., et al., Effects of Mn-doping on the structure and *in vitro* degradation of β -tricalcium phosphate. *J. Ceramics International*, **47**(16), pp 22994-23000, (2021).
42. Pajares-Chamarro, N., et al., Silver-doped bioactive glass particles for *in vivo* bone tissue regeneration and enhanced methicillin-resistant *Staphylococcus aureus* (MRSA) inhibition. *J. Materials Science and Engineering: C*, **120**, pp 111693, (2021).
43. Maher, S., et al., Advancing of 3D-Printed titanium implants with combined antibacterial protection using ultrasharp nanostructured surface and gallium-releasing agents. *J. ACS Biomaterials Science & Engineering*, **8**(1), pp 314-327, (2022).
44. De Santis, S., et al., A Simple cerium coating strategy for titanium oxide nanotubes' bioactivity enhancement. *J. Nanomaterials*, **11**(2), pp 445, (2021).
45. Bordbar-Khiabani, A., et al., Surface functionalization of anodized tantalum with Mn_3O_4 nanoparticles for effective corrosion protection in simulated inflammatory condition. *J. Ceramics International*, **48**(3), pp 3148-3156, (2022).
46. Li, K., et al., Effect of powder size on strength and corrosion behavior of $\text{Mg}_{66}\text{Zn}_{30}\text{Ca}_4$ bulk metallic glass. *J. Alloys and Compounds*, **897**, pp 163219, (2022).
47. Zoccali, C., et al., Antibacterial hydrogel coating in joint mega-prosthesis: results of a comparative series. *J. Orthopaedic Surgery & Traumatology*, **31**(8), pp 1647-1655, (2021).
48. X. Li, J. Qiu, X. Liu, Antibacterial Property and Biocompatibility of Polypyrrole Films Treated by Oxygen Plasma Immersion Ion Implantation, *Advanced Materials Interfaces*, **7** (2020).
49. Batool, F., et al., Modulation of immune-inflammatory responses through surface modifications of biomaterials to promote bone healing and regeneration. *J. Tissue Engineering*, **12**, (2021).
50. Ma, Y., et al., Size-Dependent cytotoxicity and reactive oxygen species of cerium oxide nanoparticles in human retinal pigment epithelia cells. *J. Nanomedicine*, **16**, pp 5333-5341, (2021).
51. Meng, L., et al., Bioactive rare earth-based inorganic-organic hybrid biomaterials for wound healing and repair. *J. Applied Materials Today*, **26**, pp 101304.
52. Kurtuldu, F., et al., Cerium and gallium containing mesoporous bioactive glass nanoparticles for bone regeneration: Bioactivity, biocompatibility and antibacterial activity. *J. Materials Science and Engineering: C*, **124**, pp 112050 (2021).
53. Zambon, A., et al., Cerium containing bioactive glasses: A review. *J. ACS Biomaterials Science & Engineering*, **7**(9), pp4388-4401, (2021).

54. Muthusamy, S., et al., Hydroxyapatite nanophases augmented with selenium and manganese ions for bone regeneration: Physiochemical, microstructural and biological characterization. *J. Materials Science and Engineering: C*, **126**, pp 112149, (2021).
55. Zhang, B. G., et al., Bioactive coatings for orthopaedic implants-recent trends in development of implant coatings. *J. Molecular Sciences*, **15**(7), pp 11878-11921 (2014).
56. Gritina, A. G., Biomaterial-centered infection: microbial adhesion versus tissue integration. *J. Science*, **237**(4822), pp 1588-1595 (1987).
57. Valstar, E. R., et al., The use of roentgen stereophotogrammetry to study micromotion of orthopaedic implants. *J. Photogrammetry & Remote Sensing*, **56**, pp 376-389 (2002).
58. Friis, E., Mechanical Testing of Orthopaedic Implants. *Biomaterials*. (2017).
59. Sundfeldt, M., et al., Aseptic loosening, not only a question of wear: a review of different theories. *J. Acta Orthopaedica*, **77**(2), pp 177-197 (2006).
60. Tobin, E. J., Recent coating developments for combination devices in orthopedic and dental applications: A literature review. *J. Advance Drug Delivery Reviews*, **112**, pp 88-100 (2017).
61. Navarro, M., et al., Biomaterials in orthopaedics. *J. Royal Society Interface*, **5**(27), pp 1137-1158 (2008).
62. Kartush, J. M., et al., Early Gold Weight Eyelid Implantation for Facial Paralysis. *J. Otolaryngology-Head and Neck Surgery*, **103**(6), pp 1016-1023 (1990).
63. May, M., Gold weight and wire spring implants as alternatives to tarsorrhaphy. *Archives of Otolaryngology-Head & Neck Surgery*. **113**(6), pp 656-660 (1987).
64. Hench, L. L. and Thompson, I., Twenty-first century challenges for biomaterials. *J. Royal Society Interface*, **7**(4), pp S379-S391(2010).
65. Simon, J. P., and Fabry, G., An overview of implant materials. *J. Acta othopaedica Belgical*, **57**(1), pp 1-5 (1991).
66. Burke, G. L., The corrosion of metals in tissues; and an introduction to tantalum. *J. Canadaian Medical Association*, **43**(2), pp 125-128 (1940).
67. Wang, N., et al., Study on the anticorrosion, biocompatibility, and osteoinductivity of tantalum decorated with tantalum oxide nanotube array films. *J. ACS Applield Materials Interfaces*, **4**(9), pp 4516-4123 (2012).
68. Lu, T., et al., Enhanced osteointegration on tantalum-implanted polyetheretherketone surface with bone-like elastic modulus. *J. Biomaterials*, **51**, pp 173-183 (2015).
69. Balla, V. K., et al., Porous tantalum structures for bone implants: fabrication, mechanical and *in vitro* biological properties. *J. Acta Biomaterialia*, **6**(8), pp 3349-359 (2010).
70. Hermenau, S., et al., The Biochemistry of spinal implants, *The Comprehensive Treatment of the Aging Spine*, pp 459-465 (2011).
71. Allum, S. R., et al., The impact of loads on standard diameter, small diameter and mini implants: a comparative laboratory study. *J. Clinical Oral Implants Research*, **19**(6): pp 553-559 (2008).
72. M. Davarpanah, H.M., J.F. Celletti, R. Lazzara, Small-diameter implants: idications and contraindications. *J. Esthetic Dentisty*, **12**, pp 186-194 (2000).
73. Zinsli, B., et al., Clinical evaluation of small-diameter ITI implants: A prospective study. *International J. Oral Maxillofacial Implants*, **19**(1), pp 92-99 (2004).
74. Chiapasco, M., et al., Titanium-zirconium alloy narrow-diameter implants (Straumann Roxolid((R))) for the rehabilitation of horizontally deficient edentulous ridges: prospective study on 18 consecutive patients. *J. Clinical Oral Implants Research*, **23**(10), pp 1136-1141 (2012).

75. Li, Y., et al., Cytotoxicity of titanium and titanium alloying Elements. J. Dental Research, **89**(5), pp 493-497 (2010).
76. Song, Y., et al., Cytotoxicity of alloying elements and experimental titanium alloys by WST-1 and agar overlaytests. J. Dental Materials, **30**(9): pp 977-983 (2014).
77. Radha, R. and Sreekanth, D., Insight of magnesium alloys and composites for orthopedic implant applications – a review. J. Magnesium and Alloys, **5**(3), pp 286-312 (2017)..
78. Whitlow, J., Paul, A., and Polini, A., Bioactive materials: definitions and application in tissue engineering and regeneration therapy. Biocompatible Glasses: From Bone Regeneration to Cancer Treatment. pp 1-17 (2016).
79. Jonge, L. T., et al., Organic-inorganic surface modifications for titanium implant surfaces. J. Pharmaceutical Research, **25**(10), pp 2357-2369 (2008).
80. Fathi, M. H. and Doostmohammadi, A., Bioactive glass nanopowder and bioglass coating for biocompatibility improvement of metallic implant. J. Materials Processing Technology, **209**(3), pp 1385-1391 (2009).
81. Heidenau, F., et al., A novel antibacterial titania coating: Metal ion toxicity and *in vitro* surface colonization. J. Materials Science-Materials in Medicine, **16**(10), pp 883-888 (2005).
82. Morimoto, T., et al., The bone morphogenetic protein-2/7 heterodimer is a stronger inducer of bone regeneration than the individual homodimers in a rat spinal fusion model. J. Spine, **15**(6), pp 1379-1390 (2015).
83. Kaito, T., et al., BMP-2/7 heterodimer strongly induces bone regeneration in the absence of increased soft tissue inflammation .J. Spine, **18**(1), pp 139-146 (2017).
84. Wang, W. and Poh, C. K., Titanium Alloys in Orthopaedics, Titanium Alloys - Advances in Properties, (2013).
85. Alam, M. I., et al., Evaluation of ceramics composed of different hydroxyapatite to tricalcium phosphate ratios as carriers for rhBMP-2. J. Biomaterials, **22**(12), pp 1643-1651 (2001).
86. Liu, Y., et al., BMP-2 liberated from biomimetic implant coatings induces and sustains direct ossification in an ectopic rat model. J. Bone, **36**(5): pp 745-757 (2005).
87. Papat, K.C., et al., Influence of engineered titania nanotubular surfaces on bone cells. J. Biomaterials, **28**(21), pp 3188-3197 (2007).
88. Piazza, V., et al., Key Oxidation Parameters that Influence Photo-Induced Properties and Applications of Anodic Titanium Oxides. J. The Electrochemical Society, **163**(2), pp H119-H127 (2015).
89. Shah, F. A., et al., Laser surface modification and the tissue–implant interface, Laser Surface Modification of Biomaterials. pp 253-280, (2016).
90. Grafahrend, D., et al., Degradable polyester scaffolds with controlled surface chemistry combining minimal protein adsorption with specific bioactivation. J. Nature Materials, **10**(1), pp 67-73 (2011).
91. Ma, K., et al., Osteogenetic property of a biodegradable three-dimensional macroporous hydrogel coating on titanium implants fabricated via EPD. J. Biomedical Materials, **9**(1), pp 1-10 (2014).
92. Poth, N., et al., Biodegradable chitosan nanoparticle coatings on titanium for the delivery of BMP-2. J. Biomolecules, **5**(1), pp 3-19 (2015).
93. Bonifacio, M. A., et al., Gallium-modified chitosan/poly(acrylic acid) bilayer coatings for improved titanium implant performances. J. Carbohydrate Polymers, **166**, pp 348-357 (2017).

94. Holzapfel, B. M., et al., How smart do biomaterials need to be? A translational science and clinical point of view. *J. Advanced Drug Delivery Reviews*, **65**(4), pp 581-603 (2013).
95. Heaney, R. P., et al., Bone., *Encyclopaedia Britannica*, (2019).
96. Florencio-Silva, R., et al., Biology of Bone Tissue: Structure, Function, and Factors That Influence Bone Cells. *J. Biomed Research International*, **2015**, pp 1-17 (2015).
97. Bae, Y. J. and Kim, M. H., Manganese Supplementation Improves Mineral Density of the Spine and Femur and Serum Osteocalcin in Rats. *J. Biological Trace Element Research*, **124**(1), pp 28-34 (2008).
98. Franz-Odenaal, T.A., B.K. Hall, and P.E. Witten, Buried alive: how osteoblasts become osteocytes. *Development Dynamics*, **235**(1), pp 176-190 (2006).
99. Knothe Tate, M.L., Whither flows the fluid in bone?" An osteocyte's perspective. *J. Biomechanics*, **36**(10), pp 1409-1424 (2003).
100. al., J.F.e., Functions of cells and human body, (2014).
101. Lisa, A. P., Orthopedic implant coating for imroved osseointegration and prevention of biofilm formation. Dissertation, (2014).
102. Wein, M. N., Bone Lining Cells: Normal Physiology and Role in Response to Anabolic Osteoporosis Treatments. *J. Current Molecular Biology Reports*, **3**(2), pp 79-84 (2017).
103. Charles, J. F. and Aliprantis, A. O., Osteoclasts: more than 'bone eaters'. *J. Trends Molecular Medicine*, **20**(8), pp 449-59 (2014).
104. Chaudhry, G. R., at al., Osteogenic cells derived from emryonic stem cells produced bone nodules in three-dimensional scaffolds. *J. Biomedicine and Biotechnology*, **4**, pp 203-210 (2004).
105. Fujimoto, S., et al., Clinical application of wave intensity for the treatment of essential hypertension. *J. Heart Vessels*, **19**(1), pp 19-22 (2004).
106. Awan, S. U., et al., Ferromagnetism in Li doped ZnO nanoparticles: The role of interstitial Li. *J. Applied Physics*, **112**(10), pp 1-10 (2012).
107. Green, J., et al., Cell-matrix interaction in bone: type I collagen modulates signal transduction in osteoblast-like cells. *J. Physiology cell biology*, **268**(5), pp C1090-C1103 (1995).
108. Weiner, S., et al., Lamellar bone: Structure-function relations. *Journal of Structural Biology*, **126**(3), pp 241-255 (1999).
109. Clarke, B., Normal bone anatomy and physiology. *J. American Society of Nephrology*, **3**(3) pp S131-S139 (2008).
110. Kumar, B. N. A. and Mattoo, S. K, Organ transplant and the psychiatrist: An overview. *J. Indian Medical Research*, **141**(4) pp 408-416.
111. Reddi, A.H. and Reddi, A., Bone morphogenetic proteins (BMPs): from morphogens to metabologens. *J. Cytokine Growth Factor Reviews*, **20**(5-6), pp 341-342 (2009).
112. Urist, M. R. and Strates, B. S., The classic: Bone morphogenetic protein. *J. Clinical Orthopaedics and Related Research*, **50**(6), pp 1392-1406 (1971).
113. Chen, D., et al., Bone morphogenetic proteins. *J. Growth Factors*, **22**(4), pp 233-241 (2004).
114. Urist, M.R., Bone: Formation by autoinduction science. *J. Science*, **150**(3698), pp 893-899 (1965).
115. Atsuta, Y. and Takahashi, Y., Early formation of the Mullerian duct is regulated by sequential actions of BMP/Pax2 and FGF/Lim1 signaling. *J. Development*,. **143**(19), pp 3549-3559 (2016).
116. Miyazaki, M., et al., A porcine collagen-derived matrix as a carrier for recombinant human bone morphogenetic protein-2 enhances spinal fusion in rats. *J. Spine*, **9**(1): pp 22-30 (2009).

117. Bessa, P. C., et al, Bone morphogenetic proteins in tissue engineering: the road from laboratory to clinic, part II (BMP delivery). *J. Tissue Engineering and Regenerative Medicine*, **2**(2-3), pp 81-96 (2008).
118. Groeneveld, E. H. and Burger E. H., Bone morphogenetic proteins in human bone regeneration. *J. Endocrinology*, **142**(1), pp 9-21 (2000).
119. Greenfield, E. M., et al., Does endotoxin contribute to aseptic loosening of orthopedic implants? *J. Biomedical Materials Research Part B: Applied Biomaterials*, **72B**(1), pp179-185 (2005).
120. Zimmerli, W., et al., Pathogenesis of foreign body infection: description and characteristics of an animal model. *J. Infectious Diseases*, **146**(4), pp 487-97 (1982).
121. Arciola, C. R., et al., Biofilm formation in Staphylococcus implant infections. A review of molecular mechanisms and implications for biofilm-resistant materials. *J. Biomaterials*, **33**(26), pp 5967-5982 (2012).
122. Heim, C. E., et al., IL-12 promotes myeloid-derived suppressor cell recruitment and bacterial persistence during Staphylococcus aureus orthopedic implant infection. *J. Immunology*. **194**(8), pp 3861-3872 (2015).
123. Cremet, L., et al., Pathogenic potential of Escherichia coli clinical strains from orthopedic implant infections towards human osteoblastic cells. *J. Pathogens and Disease*, **73**(8), pp ftv065 (2015).
124. Arciola, C. R., et al., Implant infections: adhesion, biofilm formation and immune evasion. *J. Nature Review Microbiology*, **16**(7), pp 397-409 (2018).
125. Chouirfa, H., et al., Review of titanium surface modification techniques and coatings for antibacterial applications. *J. Acta Biomaterialia*. **83**, pp 37-54 (2019).
126. Kumar, G. and Narayan, B., Osseointegrated Titanium Implants: Requirements for Ensuring a Long-Lasting, Direct Bone-to-Implant Anchorage in Man, *Classic Papers in Orthopaedics*, pp 507-509 (2014).
127. Goodman, S. B., The effects of micromotion and particulate materials on tissue differentiation: Bone chamber studies in rabbits. *J. Acta Orthopaedica Scandinavica*, **65**(sup258): pp 1-43 (2009).
128. Amstutz H. C., et al., Mechanism and clinical significance of wear debris-induced osteolysis. *J. Clinical Orthopaedics and Related Research*, **207**, pp 7-18 (1992).
129. Fournier, E., et al., Superelastic Orthopedic Implant Coatings. *J. Materials Engineering and Performance*, **23**(7), pp 2464-2470 (2014).
130. Kröger, H., et al., Bone density at the proximal femur after total hip arthroplasty. *J. Clinical Orthopaedics and Related Research*, **352**, pp 66-74 (1998).
131. Ryan, G., et al., Fabrication methods of porous metals for use in orthopaedic applications. *J. Biomaterials*, **27**(13), pp 2651-70 (2006).
132. Von See, C., et al., Bone augmentation after soft-tissue expansion using hydrogel expanders: effects on microcirculation and osseointegration. *J. Clinical Oral Implants Research*, **21**(8), pp 842-847 (2010).
133. Srouji, S., et al., Mandibular defect repair by TGF-beta and IGF-1 released from a biodegradable osteoconductive hydrogel. *J. Craniomaxillofacial Surgery*, **33**(2), pp 79-84 (2005).
134. Saito, N., et al., A biodegradable polymer as a cytokine delivery system for inducing bone formation. *J. Nature Biotechnology*, **19**, pp 332-335 (2001).
135. Habibovic, P., et al., Biomimetic Hydroxyapatite Coating on Metal Implants. *J. American Ceramic Society*, **85**, pp 517-22 (2002).
136. Norhidayu, D., et al., Development of Zinc doped Hydroxyapatite for bone implant applications, *ICCBT*, **24**, pp 257-270 (2008).

137. Fielding, G. A., et al., Antibacterial and biological characteristics of silver containing and strontium doped plasma sprayed hydroxyapatite coatings. *J. Acta Biomaterialia*, **8**(8), pp 3144-3152 (2012).
138. Gloria, A., et al., Magnetic poly(epsilon-caprolactone)/iron-doped hydroxyapatite nanocomposite substrates for advanced bone tissue engineering. *J. Royal Society Interface*, **10**(80), pp 20120833 (2013).
139. Wang, Y., et al., *In vitro* study on the degradation of lithium-doped hydroxyapatite for bone tissue engineering scaffold. *J. Material Science and Engineering C*, **66**, pp 185-192 (2016).
140. He, J., et al., Collagen-infiltrated porous hydroxyapatite coating and its osteogenic properties: *in vitro* and *in vivo* study. *J. Biomedical Materials Research A*, **100**(7), pp 1706-1715 (2012).
141. Shah, N. J., et al., Osteophilic multilayer coatings for accelerated bone tissue growth. *J. Advanced Materials*, **24**(11), pp 1445-1450 (2012).
142. Harrison, N., et al., Preclinical trial of a novel surface architecture for improved primary fixation of cementless orthopaedic implants. *J. Clinical Biomechanics (Bristol, Avon)*, **29**(8), pp 861-8 (2014).
143. Harrison, N., et al., Preclinical trial of a novel surface architecture for improved primary fixation of cementless orthopaedic implants. *J. Clinical Biomechanics (Bristol, Avon)*, **29**(8), pp 861-8 (2014).
144. Lan, G., et al., Promoting Bone Mesenchymal Stem Cells and Inhibiting Bacterial Adhesion of Acid-Etched Nanostructured Titanium by Ultraviolet Functionalization. *J. Materials Science & Technology*, **31**(2), pp 182-190 (2015).
145. Richert, L., et al., Surface Nanopatterning to Control Cell Growth. *J. Advanced Materials*, **20**(8), pp 1488-1492 (2008).
146. Hall, D. J., et al., Nanoscale surface modification by anodic oxidation increased bone ingrowth and reduced fibrous tissue in the porous coating of titanium-alloy femoral hip arthroplasty implants. *J. Biomedical Materials Research B Applied Biomaterials*, **105**(2), pp 283-290 (2017).
147. Huang, Y., et al., The construction of hierarchical structure on Ti substrate with superior osteogenic activity and intrinsic antibacterial capability. *J. Scientific Reports*, **4**, pp 6172 (2014).
148. Zhao, G., et al., High surface energy enhances cell response to titanium substrate microstructure. *J. Biomedical Materials Research A*, **74**(1), pp 49-58 (2005).
149. Cattini, A., et al., Suspension plasma sprayed bioactive glass coatings: Effects of processing on microstructure, mechanical properties and in-vitro behaviour. *J. Surface and Coatings Technology*, **220**, pp 52-59 (2013).
150. Patel, K. D., et al., Chitosan–nanobioactive glass electrophoretic coatings with bone regenerative and drug delivering potential. *J. Materials Chemistry*, **22**(47), pp 24945-24956 (2012).
151. Ordikhani, F. and Simchi, A., Long-term antibiotic delivery by chitosan-based composite coatings with bone regenerative potential. *J. Applied Surface Science*, **317**, pp 56-66 (2014).
152. Pishbin, F., et al., Single-step electrochemical deposition of antimicrobial orthopaedic coatings based on a bioactive glass/chitosan/nano-silver composite system. *J. Acta Biomaterialia*, **9**(7), pp 7469-7479 (2013).
153. Das, I., et al., Porous SiO₂ nanofiber grafted novel bioactive glass-ceramic coating: A structural scaffold for uniform apatite precipitation and oriented cell proliferation on inert implant. *J. Materials Science Engineering C*, **62**, pp 206-14 (2016).

154. Baino, F., et al., Bioactive glass coatings fabricated by laser cladding on ceramic acetabular cups: a proof-of-concept study. *J. Materials Science*, **52**(15), pp 9115-9128 (2017).
155. Tarafder, S., et al., Microwave-sintered 3D printed tricalcium phosphate scaffolds for bone tissue engineering. *J. Tissue Engineering and Regenerative Medicine*, **7**(8), pp 631-641 (2013).
156. Tarafder, S., et al., 3D printed tricalcium phosphate scaffolds: Effect of SrO and MgO doping on *in vivo* osteogenesis in a rat distal femoral defect model. *J. Biomaterials Science*, **1**(12), pp 1250-1259 (2013).
157. Maher, S., et al., 3D Printed titanium implants with nano-engineered surface titania nanotubes for localized drug delivery in Chemesa. *Chemeca*, pp 65-76 (2016).
158. Xue, C., et al., A highly efficient, low-toxic, wide-spectrum antibacterial coating designed for 3D printed implants with tailorable release properties. *J. Materials Chemistry B*, **5**(22), pp 4128-4136 (2017).
159. Chen, W., et al., Antibacterial and osteogenic properties of silver-containing hydroxyapatite coatings produced using a sol gel process. *J. Biomedical Materials Research A*, **82**(4), pp 899-906 (2007).
160. Kazemzadeh-Narbat, M., et al., Drug release and bone growth studies of antimicrobial peptide-loaded calcium phosphate coating on titanium. *J. Biomedical Materials Research B*, **100**(5), pp 1344-52 (2012).
161. Uskokovic, V., et al., Osteogenic and antimicrobial nanoparticulate calcium phosphate and poly-(D,L-lactide-co-glycolide) powders for the treatment of osteomyelitis. *J. Materials Science Engineering C*, **33**(6), pp 3362-3373 (2013).
162. Annabi, N., et al., 25th Anniversary Article: Rational Design and Applications of Hydrogels in Regenerative Medicine. *J. Advanced Materials*, **26**(1), pp 85-124 (2014).
163. Shi, Z. L., et al., Surface Functionalization of Titanium with Carboxymethyl Chitosan and Immobilized Bone Morphogenetic Protein-2 for Enhanced Osseointegration. *J. Biomacromolecules*, **10**(6), pp 1603-1611 (2009).
164. Martino, M. M., et al., Extracellular matrix-inspired growth factor delivery systems for bone regeneration. *J. Advance Drug Delivery Review*, **94**, pp 41-52 (2015).
165. Cotrim, A. P. and Baum, B. J., Gene therapy: some history, applications, problems, and prospects. *J. Toxicologic Pathology*, **36**(1), pp 97-103 (2008).
166. Ramseier, C. A., et al., Gene therapeutics for periodontal regenerative medicine. *J. Dental Clinical*, **50**(2), pp 245-63, (2006).
167. Talarico, D. et al., Protection of mice against tumor growth by immunization with an oncogene-encoded growth factor. *J. Proceeding of the National Academy of Sciences*, **87**(11), pp 4222-4225 (1990).
168. Elangovan, S., et al., The enhancement of bone regeneration by gene activated matrix encoding for platelet derived growth factor. *J. Biomaterials*, **35**(2), pp 737-747 (2014).
169. Mishra, R., et al., Growth factor dose tuning for bone progenitor cell proliferation and differentiation on resorbable poly(propylene fumarate) scaffolds. *J. Tissue Engineering Part C*, **22**(9), pp 904-913 (2016).
170. Otsuru, S., et al., Bone marrow-derived osteoblast progenitor cells in circulating blood contribute to ectopic bone formation in mice. *J. Biochemical and Biophysical Research Communications*, **354**(2), pp 453-458 (2007).
171. Higashino, K., et al., Stromal cell-derived factor-1 potentiates bone morphogenetic protein-2 induced bone formation. *J. Tissue Engineering Part A*, **17**(3-4), pp 523-530 (2011).

172. Hwang, H. D., et al., Sequential treatment with SDF-1 and BMP-2 potentiates bone formation in calvarial defects. *J. Tissue Engineering Part A*, **21**(13-14), pp 2125-2135 (2015).
173. Raphael, J., et al., Engineered protein coatings to improve the osseointegration of dental and orthopaedic implants. *J. Biomaterials*, **83**, pp 269-82 (2016).
174. Liu, Y., et al., Role of implants surface modification in osseointegration: A systematic review. *J. Biomedical Materials Research A*, **108**(3), pp 470-484 (2020).
175. Harrison, N., et al., Micromotion and friction evaluation of a novel surface architecture for improved primary fixation of cementless orthopaedic implants. *J. Mechanical Behavior of Biomedical Materials*, **21**, pp 37-46 (2013).
176. LeGeros, R. Z., Properties of Osteoconductive Biomaterials: Calcium Phosphates. *J. Clinical Orthopaedics and Related Research*, **395**, pp 81-98 (2002).
177. Jones, J. R., Review of bioactive glass: From Hench to hybrids. *J. Acta Biomaterialia*, **9**(1), pp 4457-4486 (2013).
178. Sollazzo, V., et al., Zirconium oxide coating improves implant osseointegration *in vivo*. *J. Dental Materials*, **24**(3), pp 357-361 (2008).
179. Bessa, P. C., et al., Bone morphogenetic proteins in tissue engineering: the road from laboratory to clinic, part II (BMP delivery). *J. Tissue Engineering and Regenerative Medicine*, **2**(2-3), pp 81-96 (2008).
180. Salou, L., et al., Enhanced osseointegration of titanium implants with nanostructured surfaces: an experimental study in rabbits. *J. Acta Biomaterialia*, **11**, pp 494-502 (2015).
181. Jemat, A., et al., Surface modifications and their effects on titanium dental implants. *J. Biomedical Research International*, **2015**, pp 791725 (2015).
182. Hindy, A., et al., *In vitro* biological outcome of laser application for modification or processing of titanium dental implants. *J. Lasers Medical Science*, **32**(5), pp 1197-1206 (2017).
183. Tang, Z., et al., Porous tantalum coatings prepared by vacuum plasma spraying enhance bmscs osteogenic differentiation and bone regeneration *in vitro* and *in vivo*. *J. Social Psychiatry*, **8**(6), pp e66263 (2013).
184. Feddes, B., et al., Initial deposition of calcium phosphate ceramic on polyethylene and polydimethylsiloxane by rf magnetron sputtering deposition: the interface chemistry. *J. Biomaterials*, **25**(4), pp 633-639 (2004).
185. Adams, C. S., et al., Controlled release of vancomycin from thin sol-gel films on implant surfaces successfully controls osteomyelitis. *J. Orthopaedics Research*, **27**(6), pp 701-709 (2009).
186. Yao, Y. T., et al., Effects of acid-alkali treatment on bioactivity and osteoinduction of porous titanium: An *in vitro* study. *J. Material Science Engineering C*, **94**, pp 200-210 (2019).
187. Li, X., et al., Tantalum coating on porous Ti6Al4V scaffold using chemical vapor deposition and preliminary biological evaluation. *J. Material Science Engineering C*, **33**(5), pp 2987-2994 (2013).
188. Lewallen, E. A., et al., Biological strategies for improved osseointegration and osteoinduction of porous metal orthopedic implants. *J. Tissue Engineering Part B Reviews*, **21**(2), pp 218-230 (2015).
189. Heng, B.C., et al., Effect of cell-seeding density on the proliferation and gene expression profile of human umbilical vein endothelial cells within ex vivo culture. *J. Cytotherapy*, **13**(5), pp 606-617 (2011).
190. Zhao, L., et al., Antibacterial coatings on titanium implants. *J. Biomedical Materials Research B*, **91**(1), pp 470-80 (2009).

191. Parsons, I. M., et al., What is the role of joint replacement surgery? *J. Best Practice and Research Clinical Rheumatology*, **18**(4), pp. 557-572 (2004).
192. Graves, S., and Turner, C., Hip, knee and shoulder arthroplasty annual report, Australian Orthopaedic Association National Joint Registry, 20th annual report (2019).
193. Kurtz, S., et al., Projections of primary and revision hip and knee arthroplasty in the United States from 2005 to 2030. *J. Bone Joint Surgeries*, **89**(4), pp 780-785 (2007).
194. Oussedik, S., et al., Defining peri-prosthetic infection: do we have a worable gold standard? *J. Bone and Joint Surgery*, **94**, pp 1455-1456 (2012).
195. Anagnostakos, K. et al., Classification of hip joint infections. *J. Medical Sciences*, **6**, pp 227-233 (2009).
196. Kargupta, R., et al., Coatings and surface modifications imparting antimicrobial activity to orthopedic implants. *J. Nanomedicine and Nanobiotechnology*, **6**(5), pp 475-495 (2014).
197. Trampuz, A. and Widmer, A. F., Infections associated with orthopedic implants. *J. Infectious Diseases*, **19**(4), pp 349-356 (2006).
198. Moran, E., et al., The diagnosis and management of prosthetic joint infections. *J. Antimicrobial Chemotherapy*, **65** (3) ppiii45-iii54 (2010).
199. Darouiche, R. O., Treatment of infections associated with surgical implants. *J. Medicine*, **350**, pp 1422-1429 (2004).
200. Harris, L. G., et al., Staphylococcus aureus adhesion to titanium oxide surfaces coated with non-functionalized and peptide-functionalized poly(L-lysine)-grafted-poly(ethylene glycol) copolymers. *J. Biomaterials*, **25**(18), pp 4135-4148 (2004).
201. Shi, Z. et al., Titanium with surface-grafted dextran and immobilized bone morphogenetic protein-2 for inhibition of bacterial adhesion and enhancement of osteoblast functions. *J. Tissue Engineering Part A*, **15**, pp 417-426 (2007).
202. Klok, H. A. and Genzer, J., Expanding the polymer mechanochemistry toolbox through surface-initiated polymerization. *J. ACS Macro Letters*, **4**(6), pp 636-639 (2015).
203. Buzzacchera, I., et al., Polymer Brush-Functionalized Chitosan Hydrogels as Antifouling Implant Coatings. *Biomacromolecules*, **18**(6), pp 1983-1992 (2017).
204. Zhao, L., et al., Antibacterial nano-structured titania coating incorporated with silver nanoparticles. *J. Biomaterials*, **32**(24), pp 5706-5716 (2011).
205. Gristina, A. G., Biomaterial-centered infection: microbial adhesion versus tissue integration. *Science*, **237**, pp 1588-1595 (1987).
206. Peng, Z., et al., Dual effects and mechanism of TiO₂ nanotube arrays in reducing bacterial colonization and enhancing C3H10T1/2 cell adhesion. *J. Nanomedicine*, **8**, pp 3093-3105 (2013).
207. Izquierdo-Barba, I., et al., Nanocolumnar coatings with selective behavior towards osteoblast and Staphylococcus aureus proliferation. *J. Acta Biomaterialia*, **15**: p. 20-28 (2015).
208. Cao, H., et al., Electron storage mediated dark antibacterial action of bound silver nanoparticles: smaller is not always better. *J. Acta Biomaterialia*, **9**(2), pp 5100-5110 (2013).
209. Qiao, S., et al., Ag-plasma modification enhances bone apposition around titanium dental implants: an animal study in Labrador dogs. *J. Nanomedicine*, **10**, pp 653-654 (2015).
210. Jin, G., et al., Synergistic effects of dual Zn/Ag ion implantation in osteogenic activity and antibacterial ability of titanium. *J. Biomaterials*, **35**(27), pp 7699-7713 (2014).

211. Huang, R., et al., Enhanced osteoblast functions and bactericidal effect of Ca and Ag dual-ion implanted surface layers on nanograined titanium alloys. *J. Materials Chemistry B*, **2**(28) pp 4531-4543 (2014).
212. Sharp, R., A review of the applications of chitin and its derivatives in agriculture to modify plant-microbial interactions and improve crop yields. *J. Agronomy*, **3**(4): p. 757-793 (2013).
213. Rabea, E. I., et al., Chitosan as antimicrobial agent: Applications and mode of action. *the American Chemical Society*, **4**(3) pp1457-1465 (2003).
214. Dash, M., et al., Chitosan—A versatile semi-synthetic polymer in biomedical applications. *J. Progress in Polymer Science*, **36**(8), pp 981-1014 (2011).
215. Chua, P. H., et al., Surface functionalization of titanium with hyaluronic acid/chitosan polyelectrolyte multilayers and RGD for promoting osteoblast functions and inhibiting bacterial adhesion. *J. Biomaterials*, **29**(10), pp 1412-1421 (2008).
216. Zheng, D., et al., Assessment of stability of surface anchors for antibacterial coatings and immobilized growth factors on titanium. *J. Colloid and Interface Science*, **406**, pp 238-246 (2013).
217. Zhao, L., et al., Surface functionalization of titanium substrates with chitosan-lauric acid conjugate to enhance osteoblasts functions and inhibit bacteria adhesion. *J. Colloids and Surface B*, **119**, pp 115-125 (2014).
218. Mattioli-Belmonte, M., et al., Characterization and cytocompatibility of an antibiotic/chitosan/cyclodextrins nanocoating on titanium implants. *J. Carbohydrate Polymers*, **110**, pp 173-182 (2014).
219. Ordikhani, F., et al., Characterization and antibacterial performance of electrodeposited chitosan-vancomycin composite coatings for prevention of implant-associated infections. *J. Materials Science Engineering C*, **41**, pp 240-248 (2014).
220. Song, J., et al., Electrophoretic Deposition of Chitosan Coatings Modified with Gelatin Nanospheres To Tune the Release of Antibiotics. *J. ACS Applied Material Interfaces*, **8**(22), pp 13785-13792 (2016).
221. Cometa, S., et al., Silver-loaded chitosan coating as an integrated approach to face titanium implant-associated infections: analytical characterization and biological activity. *J. Analytical and Bioanalytical Chemistry*, **409**(30), pp 7211-7221 (2017).
222. Antoci, V., Jr., et al., The inhibition of *Staphylococcus epidermidis* biofilm formation by vancomycin-modified titanium alloy and implications for the treatment of periprosthetic infection. *J. Biomaterials*, **29**(35), pp 4684-4690 (2008).
223. Antoci, V., Jr., et al., Vancomycin covalently bonded to titanium alloy prevents bacterial colonization. *J. Orthopaedics Research*, **25**(7), pp 858-866 (2007).
224. Hickok, N.J. and Shapiro, I.M., Immobilized antibiotics to prevent orthopaedic implant infections. *Adv Drug Deliv Rev*, **64**(12), pp 1165-1176 (2012).
225. Zimmerli, W., Clinical presentation and treatment of orthopaedic implant-associated infection. *J. Internal Medicine*, **276**(2), pp 111-119 (2014).
226. Asharani, P. V., et al., Cytotoxicity and genotoxicity of silver nanoparticles in human cells. *J. ACS Nano*, **3**, pp 279-290 (2009).
227. Agarwal, A., et al., Surfaces modified with nanometer-thick silver-impregnated polymeric films that kill bacteria but support growth of mammalian cells. *J. Biomaterials*, **31**(4), pp 680-690 (2010).
228. Liu, Y., et al., The antimicrobial and osteoinductive properties of silver nanoparticle/poly (DL-lactic-co-glycolic acid)-coated stainless steel. *J. Biomaterials*, **33**(34), pp 8745-8756 (2012).
229. Gao, A., et al., The effects of titania nanotubes with embedded silver oxide nanoparticles on bacteria and osteoblasts. *J. Biomaterials*, **35**(13), pp 4223-4235 (2014).

230. Tilmaciu, C. M., et al., *In vitro* and *in vivo* characterization of antibacterial activity and biocompatibility: a study on silver-containing phosphonate monolayers on titanium. *J. Acta Biomaterialia*, **15**, pp 266-277 (2015).
231. Surmeneva, M. A., et al., Incorporation of silver nanoparticles into magnetron-sputtered calcium phosphate layers on titanium as an antibacterial coating. *J. Colloids Surface*, **156**, pp 104-113 (2017).
232. Marambio-Jones, C. and Hoek, E. M. V., A review of the antibacterial effects of silver nanomaterials and potential implications for human health and the environment. *J. Nanoparticle Research*, **12**(5), pp 1531-1551 (2010).
233. Barrioni, B. R., et al., The Evolution, Control, and Effects of the Compositions of Bioactive Glasses on Their Properties and Applications, *Biocompatible Glasses*, pp 85-117 (2016).
234. Hu, H., et al., Antibacterial activity and increased bone marrow stem cell functions of Zn-incorporated TiO₂ coatings on titanium. *J. Acta Biomaterialia*, **8**(2), pp 904-915 (2012).
235. Svensson, S., et al., Osseointegration of titanium with an antimicrobial nanostructured noble metal coating. *J. Nanomedicine*, **9**(7), pp 1048-1056 (2013).
236. Bejarano, J., et al., Sol-gel synthesis and *in vitro* bioactivity of copper and zinc-doped silicate bioactive glasses and glass-ceramics. *J. Biomedical Materials*, **10**(2), pp 025001 (2015).
237. Valappil, S. P., et al., Controlled delivery of antimicrobial gallium ions from phosphate-based glasses. *J. Acta Biomaterialia*, **5**(4), pp 1198-1210 (2009).
238. Karakoti, A. S., et al., Nanocerium as Antioxidant: Synthesis and Biomedical Applications. *J. Minerals*, **60**(3), pp 33-37 (2008).
239. Bracer, L., et al., Decrease of Staphylococcal adhesion on surgical stainless steel after Si ion implantation. *J. Applied Surface Science*, **310**, pp 36-41 (2014).
240. Hardes, J., et al., The influence of elementary silver versus titanium on osteoblasts behaviour *in vitro* using human osteosarcoma cell lines. *J. Sarcoma*, **2007**, pp 26539 (2007).
241. Brohede, U., et al., Multifunctional implant coatings providing possibilities for fast antibiotics loading with subsequent slow release. *Journal of Materials Science: J. Materials in Medicine*, **20**(9), pp 1859-1867 (2009).
242. Conrad, J. R., et al., Plasma source ion-implantation technique for surface modification of materials. *J. Applied Physics*, **62**(11), pp 4591-4596 (1987).
243. Cao, H., et al., Electron storage mediated dark antibacterial action of bound silver nanoparticles: Smaller is not always better. *J. Acta Biomaterialia*, **9**(2), pp 5100-5110 (2013).
244. Amiri, S. and Rahimi, A., Hybrid nanocomposite coating by sol-gel method: a review. *J. Iranian Polymer*, **25**(6), pp 559-577 (2016).
245. Eliaz, N. and Metoki, N., Calcium Phosphate Bioceramics: A Review of Their History, Structure, Properties, Coating Technologies and Biomedical Applications. *J. Materials*, **10**(4), pp 334 (2017).
246. Hareesh, K., et al., Antibacterial properties of Au doped polycarbonate synthesized by gamma radiation assisted diffusion method. *J. Radiation Physics and Chemistry*, **112**, pp 97-103 (2015).
247. Chawengkijwanich, C. and Hayata, Y., Development of TiO₂ powder-coated food packaging film and its ability to inactivate *Escherichia coli* *in vitro* and in actual tests. *J. Food Microbiology*, **123**(3), pp 288-292 (2008).
248. Bjursten, L. M., et al., Titanium dioxide nanotubes enhance bone bonding *in vivo*. *J. Biomedical Material Research A*, **92**(3), pp 1218-1224 (2010).

249. Randeniya, L. K., et al., Thin-film nanocomposites of diamond-like carbon and titanium oxide; Osteoblast adhesion and surface properties. *J. Diamond and Related Materials*, **19**(4), pp 329-335 (2010).
250. Gamage, J. and Zhang, Z., Applications of Photocatalytic Disinfection. *International J. Photoenergy*, **2010**, pp 1-11 (2010).
251. Kawano, T., et al., Blue-violet laser modification of titania treated titanium: antibacterial and osteo-inductive effects. *J. Plos One*, **8**(12), pp e84327 (2013).
252. Brown, E. M. and Macleod, R. J., Extracellular calcium sensing and extracellular calcium signaling. *J. Physiological reviews*, **81**(1), pp 239-297 (2001).
253. Lu, T., et al., Enhanced osteogenic activity of poly ether ether ketone using calcium plasma immersion ion implantation. *J. Colloids Surface B*, **142**, pp 192-198 (2016).
254. Wolf, F. I. and Cittadini, A., Chemistry and biochemistry of magnesium. *J. Molecular aspects of medicine*, **24**, pp 3-9 (2003).
255. Zreiqat, H., et al., Mechanisms of magnesium-stimulated adhesion of osteoblastic cells to commonly used orthopaedic implants. *J. Biomedical Material Research*, **62**(2), pp 175-184 (2002).
256. Park, S.-H., et al., Immobilization of silver nanoparticle-decorated silica particles on polyamide thin film composite membranes for antibacterial properties. *J. Membrane Science*, **499**, pp 80-91 (2016).
257. Manikandan, R., et al., Biosynthesis of silver nanoparticles using aqueous extract of *Phyllanthus acidus* L. fruits and characterization of its anti-inflammatory effect against H₂O₂ exposed rat peritoneal macrophages. *J. Process Biochemistry*, **55**, pp 172-181 (2017).
258. Liu, Y. J., et al., Magnesium and zinc borate enhance osteoblastic differentiation of stem cells from human exfoliated deciduous teeth *in vitro*. *J. Biomaterial Applications*, **32**(6), pp 765-774 (2018).
259. Sun, H., et al., Zinc oxide/vanadium pentoxide heterostructures with enhanced day-night antibacterial activities. *J. Colloid and Interface Science*, **547**, pp 40-49 (2019).
260. Shao, D., et al., Macrophage polarization by plasma sprayed ceria coatings on titanium-based implants: Cerium valence state matters. *J. Applied Surface Science*, **504** pp 144170 (2020).
261. Aminuddin, N. I., et al., Human fetal osteoblast cell response to self-assembled nanostructures on YSZ-(110) single crystal substrates. *J. Materials and Design*, **94**, pp 274-279 (2016).
262. Li, K., et al., Cerium Oxide-Incorporated Calcium Silicate Coating Protects MC3T3-E1 Osteoblastic Cells from H₂O₂-Induced Oxidative Stress. *J. Biological Trace Element Research*, **174**(1), pp 198-207 (2016).
263. Li, X., et al., Surface treatments on titanium implants via nanostructured ceria for antibacterial and anti-inflammatory capabilities. *J. Acta Biomaterials*, **94**, pp 627-643 (2019).
264. Moongraksathum, B. and Chen, Y. W., Anatase TiO₂ co-doped with silver and ceria for antibacterial application. *J. Catalysis Today*, **310**, pp 68-74 (2018).
265. Khadar, Y. A. S., et al., Hydrothermal Synthesis of Gadolinium (Gd) Doped Cerium Oxide (CeO₂) Nanoparticles: Characterization and Antibacterial Activity. *J. Chemistry*, **33**(5), pp 2405-2411 (2017).
266. Gomez-Cerezo, N., et al., The response of pre-osteoblasts and osteoclasts to gallium containing mesoporous bioactive glasses. *J. Acta Biomaterials*, **76**, pp 333-343 (2018).
267. Pourshahrestani, S., et al., Gallium-containing mesoporous bioactive glass with potent hemostatic activity and antibacterial efficacy. *J. Materials Chemistry B*, **4**(1), pp 71-86 (2016).

268. Rahimnejad Yazdi, A., et al., The impact of gallium content on degradation, bioactivity, and antibacterial potency of zinc borate bioactive glass. *J. Biomedical Material Research B*, **106**(1), pp 367-376 (2018).
269. Zhao, Q. M., et al., Enhanced osteogenic activity and antibacterial ability of manganese–titanium dioxide microporous coating on titanium surfaces. *J. Nanotoxicology*, **14**(3) pp 289-309 (2019).
270. Barrioni, B. R., et al., Sol–gel-derived manganese-releasing bioactive glass as a therapeutic approach for bone tissue engineering. *J. Materials Science*, **52**(15), pp 8904-8927 (2017).
271. Mesaros, A., et al., Towards understanding the enhancement of antibacterial activity in manganese doped ZnO nanoparticles. *J. Applied Surface Science*, **471**, pp 960-972 (2019).
272. Anwar, Y., Antibacterial and lead ions adsorption characteristics of chitosan-manganese dioxide bionanocomposite. *J. Biological Macromolecules*, **111**, pp 1140-1145 (2018).
273. Chitambar, C. R. and Narasimhan, J., Targeting iron-dependent DNA synthesis with gallium and transferrin-gallium. *J. Pathobiology*, **59**(1), pp 3-10 (1991).
274. Shannon, R. D. and Prewitt, C.T., Effective ionic radii in oxides and fluorides. *J. Acta Crystallographica Section B*, **25**(5), pp 925-946 (1969).
275. Burns, R. G., Mineralogical applications of crystal field theory (1970).
276. Bernstein, L. R., Mechanisms of therapeutic activity for gallium. *J. Pharmacological Reviews*, **50**(4), pp 665-682 (1998).
277. Inoue, T. et al., Bactericidal activity of Manganese and Iodide ions against *Staphylococcus aureus*: A possible treatment for acute atopic dermatitis. *J. Acta Dermato Venereologica*, **79**, pp 360-362 (1999).
278. Warrell, R. P. et al., Gallium Nitrate for advanced Paget disease of bone: effectiveness and dose-response analysis. *J. Annals of Internal Medicine*, **113**, pp 847-851 (1990).
279. XXu, Z., et al., Antimicrobial effect of gallium nitrate against bacteria encountered in burn wound infections. *J. Research Advances*, **7**(82), pp 52266-52273 (2017).
280. Dong, J., et al., Gallium-doped titania nanotubes elicit anti-bacterial efficacy *in vivo* against *Escherichia coli* and *Staphylococcus aureus* biofilm. *J. Materialia*, **5** pp 100209 (2019).
281. Gómez-Cerezo, N., et al., The response of pre-osteoblasts and osteoclasts to gallium containing mesoporous bioactive glasses. *J. Acta Biomaterialia*, **76**, pp 333-343 (2018).
282. Guidon, P. T., et al., Gallium nitrate regulates rat osteoblast expression of osteocalcin protein and mRNA levels. *J. Bone and Mineral Research*, **8**(1), pp 103-112 (1993).
283. Jannen-Dechent, W. and Ketteler, M., Magnesium basics. *J. Clinical Kidney*, **5**(Suppl 1), pp i3-i14 (2012).
284. Oweson, C. and Hernroth, B., A comparative study on the influence of manganese on the bactericidal response of marine invertebrates. *J. Fish and Shellfish Immunology*, **27**(3), pp 500-507 (2009).
285. Atif, M., et al., Manganese-Doped Cerium Oxide Nanocomposite Induced Photodynamic Therapy in MCF-7 Cancer Cells and Antibacterial Activity. *J. BioMedical Research International*, **2019**, pp 7156828 (2019).
286. Lüthen, F., et al., Influence of manganese ions on cellular behavior of human osteoblasts *in vitro*. *J. Biomolecular Engineering*, **24**(5), pp 531-536 (2007).
287. Santamaria, A. B. and Sulsky, S. I., Risk Assessment of an Essential Element: Manganese. *J. Toxicology and Environmental Health A*, **73**(2-3), pp 128-155 (2010).

288. Pandey, A., et al., Enhanced Tribological and Bacterial Resistance of Carbon Nanotube with Ceria- and Silver-Incorporated Hydroxyapatite Biocoating. *J. Nanomaterials*, **8**(6), pp 363 (2018).
289. Vuong, J. and Hellmich, C., Bone fibrillogenesis and mineralization: quantitative analysis and implications for tissue elasticity. *J. Theoretical Biology*, **287**, pp 115-130 (2011).
290. Marchi, J., *Biocompatible Glasses : From Bone Regeneration to Cancer Treatment*, evaluation, control, and effects of the compositions of bioactive glasses on their properties and applications, (2016).
291. Vassie, J. A., et al., Endocytosis of cerium oxide nanoparticles and modulation of reactive oxygen species in human ovarian and colon cancer cells. *J. Acta Biomaterialia*, **50**, pp 127-141 (2017).
292. Capdevila-Cortada, M., et al., Reactivity descriptors for ceria in catalysis. *J. Applied Catalysis B*, **197**, pp 299-312 (2016).
293. Lakshimi, R. V, et al., Ceria nanoparticles vis-à-vis cerium nitrate as corrosion inhibitors for silica-alumina hybrid sol-gel coating. *J. Applied Surface Science*, **393**, pp 397-404 (2017).
294. Xie, S., et al., Ceria and ceria-based nanostructured materials for photoenergy applications. *J. Nano Energy*, **34**, pp 313-337 (2017).
295. Melnik, J., et al., Ceria and copper/ceria functional coatings for electrochemical applications: Materials preparation and characterization. *J. Power Sources*, **195**(8), pp 2189-2195 (2010).
296. Wu, H., et al., Ceria nanocrystals decorated mesoporous silica nanoparticle based ROS-scavenging tissue adhesive for highly efficient regenerative wound healing. *J. Biomaterials*, **151**, pp 66-77 (2017).
297. Xue, M., et al., Enhanced superhydrophilicity and thermal stability of ITO surface with patterned ceria coatings. *J. Applied Surface Science*, **329**, pp 11-16 (2015).
298. Peedikakkandy, L., et al., Preparation of spherical ceria coated silica nanoparticle abrasives for CMP application. *J. Applied Surface Science*, **357**, pp 1306-1312 (2015).
299. Logothetidis, S., et al., Dielectric properties and electronic transitions of porous and nanostructured cerium oxide films. *J. Materials Science and Engineering B*, **109**(1-3), pp 69-73 (2004).
300. Suda, S., Nanocomposite glass abrasives. *J. Ceramic Society of Japan*, **122**(1424), pp 244-249 (2014).
301. Nagaraju, P., et al., Structural, morphological, optical and gas sensing properties of nanocrystalline ceria thin films. *J. Materials Today*, **3**(10), pp 4009-4018 (2016).
302. Zhang, S., et al., Nanostructured composite films of ceria nanoparticles with anti-UV and scratch protection properties constructed using a layer-by-layer strategy. *J. Applied Surface Science*, **382**, pp 316-322 (2016).
303. Gao, Y., et al., Cerium oxide nanoparticles in cancer. *J. Oncology Targets and Therapy*, **7**, pp 835-840 (2014).
304. Xiao, Y. F., et al., Cerium oxide nanoparticles inhibit the migration and proliferation of gastric cancer by increasing DHX15 expression. *J. Nanomedicine*, **11**, pp 3023-3034 (2016).
305. Tian, Z., et al., Highly sensitive and robust peroxidase-like activity of porous nanorods of ceria and their application for breast cancer detection. *J. Biomaterials*, **59**, pp 116-124 (2015).
306. Das, J., et al., Nanoceria-mediated delivery of doxorubicin enhances the anti-tumour efficiency in ovarian cancer cells via apoptosis. *J. Scientific Reports*, **7**(1), pp 9513 (2017).

307. Ece Alpaslan, H. Y., et al., Dextran coated cerium oxide nanoparticles for inhibiting bone cancer cell functions, *Biomaterials science: processing, properties, and applications V.* (2015).
308. Altmann, B., et al., Assessment of Novel Long-Lasting ceria-stabilized zirconia-based ceramics with different surface topographies as implant materials. *J. Advanced Functional Materials*, **27**(40), pp 1702512 (2017).
309. He, L., et al., Recent advances of cerium oxide nanoparticles in synthesis, luminescence and biomedical studies: a review. *J. Rare Earths*, **33**(8), pp 791-799 (2015).
310. You, M., et al., The Effects of Cerium valence states at cerium oxide coatings on the responses of bone mesenchymal stem cells and macrophages. *J. Biological Trace Element Research*, **179**(2), pp 259-270 (2017).
311. Murugan, R., et al., Pure and alkaline metal ion (Mg, Ca, Sr, Ba) doped cerium oxide nanostructures for photo degradation of methylene blue. *J. Materials Research Bulletin*, **97**, pp 319-325 (2018).
312. Hummers, W. S. and Offeman, R. E., Preparation of Graphitic Oxide. *J. American Chemical Society*, **80**(6), pp 1339-1339 (1958).
313. Channei, D., et al., Influence of graphene oxide on photocatalytic enhancement of cerium dioxide. *J. Materials Letters*, **209**, pp 43-47 (2017).
314. Yavo, N., et al., Relaxation and saturation of electrostriction in 10 mol% Gd-doped ceria ceramics. *J. Acta Materialia*, **144**, pp 411-418 (2017).
315. Lee, H.-C., et al., Ionic conductivity and relaxations of In-doped GDC (gadolinium doped ceria) ceramics. *J. Ceramics International*, **43**(15), pp 11792-11798 (2017).
316. Fuentes, R. and Baker, R., Synthesis and properties of Gadolinium-doped ceria solid solutions for IT-SOFC electrolytes. *J. Hydrogen Energy*, **33**(13), pp 3480-3484 (2008).
317. Wattanathana, W., et al., Samarium doped ceria (SDC) synthesized by a metal triethanolamine complex decomposition method: Characterization and an ionic conductivity study. *J. Ceramics International*, **43**(13), pp 9823-9830 (2017).
318. Mandapaka, R. and Madras, G., Aluminium and rhodium co-doped ceria for water gas shift reaction and CO oxidation. *J. Molecular Catalysis*, **451**, pp 4-12, (2017).
319. Mandapaka, R. and Madras, G., Zinc and platinum co-doped ceria for WGS and CO oxidation. *J. Applied Catalysis B*, **211**, pp 137-147 (2017).
320. Zhao, Q., et al., The Effect of the Presence of Ceria on the Character of TiO₂ Mesoporous Films Used as Pt Catalyst Support for Methanol Combustion at Low Temperature. *J. Combustion Science and Technology*, **188**(2), pp 306-314 (2016).
321. Huang, H., et al., Effects of Mn-doped ceria oxygen-storage material on oxidation activity of diesel soot. *J. Research Advances*, **7**(12), pp 7406-7412 (2017).
322. Yabe, S., Cerium oxide for sunscreen cosmetics. *J. Solid State Chemistry*, **171**(1-2), pp 7-11 (2003).
323. Akbari, A., et al., Zinc-doped cerium oxide nanoparticles: Sol-gel synthesis, characterization, and investigation of their *in vitro* cytotoxicity effects. *J. Molecular Structure*, **1149**, pp 771-776 (2017).
324. Li, K., et al., Incorporation of cerium oxide into hydroxyapatite coating regulates osteogenic activity of mesenchymal stem cell and macrophage polarization. *J. Biomaterial Applications*, **31**(7), pp 1062-1076 (2017).
325. Yuan, Q., et al., Synthesis and characterization of Cerium-doped hydroxyapatite/polylactic acid composite coatings on metal substrates. *J. Materials Chemistry and Physics*, **182**, pp 365-371 (2016).
326. Li, K., et al., The Effects of Cerium Oxide Incorporation in Calcium Silicate Coating on Bone Mesenchymal Stem Cell and Macrophage Responses. *J. Biological Trace Element Research*, **177**(1), pp 148-158 (2017).

327. Gopinathan, E., et al., Optical, surface analysis and antibacterial activity of ZnO–CuO doped cerium oxide nanoparticles. *J. Light and Electron Optics*, **126**(24) pp 5830-5835. 2015.
328. Clark, A., et al., Titanium-doped cerium oxide nanoparticles protect cells from hydrogen peroxide-induced apoptosis. *J. Nanopart Research*, **15**(12), pp 2126 (2013).
329. Gionco, C., et al., Cerium-Doped Zirconium Dioxide, a Visible-Light-Sensitive Photoactive Material of Third Generation. *J. Physical Chemistry Letters*, **5**(3), pp 447-451 (2014).
330. Goh, Y.-F., et al., In-vitro characterization of antibacterial bioactive glass containing ceria. *J. Ceramics International*, **40**(1, Part A), pp 729-737 (2014).
331. Li, H., et al., The Advances of Ceria Nanoparticles for Biomedical Applications in Orthopaedics. *J. Nanomedicine*, **15**, pp 7199-7214 (2020).
332. Alpaslan, E., et al., pH-Controlled Cerium Oxide Nanoparticle Inhibition of Both Gram-Positive and Gram-Negative Bacteria Growth. *J. Scientific Reports*, **7**: pp 45859. (2017).
333. Pelletier, D. A., et al., Effects of engineered cerium oxide nanoparticles on bacterial growth and viability. *J. Applied Environmental Microbiology*, **76**(24), pp 7981-7989 (2010).
334. Asati, A., et al., Oxidase-like activity of polymer-coated Cerium oxide nanoparticles. *J. Angewandte Chemie*, **48**(13), pp 2308-2312 (2009).
335. Roduner, E., Size matters: why nanomaterials are different. *J. Chemical Society Review*, **35**(7), pp 583-592 (2006).
336. Schubert, D., et al., Cerium and yttrium oxide nanoparticles are neuroprotective. *J. Biochemical Biophysical Research Communications*, **342**(1), pp 86-91 (2006).
337. Li, X., et al., Surface treatments on titanium implants via nanostructured ceria for antibacterial and anti-inflammatory capabilities. *J. Acta Biomaterialia*, **94**, pp 627-643 (2019).
338. He, X., et al., Changing exposure media can reverse the cytotoxicity of ceria nanoparticles for *Escherichia coli*. *J. Nanotoxicology*, **6**(3), pp 233-240 (2012).
339. Xie, C., et al., *Bacillus subtilis* causes dissolution of ceria nanoparticles at the nano-bio interface. *J. Environmental science: Nano*, **6**(1), pp 216-223 (2019).
340. Chen, W. F., et al., Impact of morphology and collagen-functionalization on the redox equilibria of nanoceria for cancer therapies. *J. Materials Science and Engineering C*, pp 111663 (2020).
341. Mehmood, R., et al., pH-responsive morphology-controlled redox behavior and cellular uptake of nanoceria in fibrosarcoma. *J. Biomaterials Science and Engineering*, **4**(3), pp 1064-1072 (2018).
342. Romer, I., et al., Impact of particle size, oxidation state and capping agent of different cerium dioxide nanoparticles on the phosphate-induced transformations at different pH and concentration. *J. Plos One*, **14**(6), pp e0217483 (2019).
343. Habib, I. Y., et al., Dynamic Light Scattering and Zeta Potential Studies of Ceria Nanoparticles. *J. Solid State Phenomena*, **278**, pp 112-120 (2018).
344. Huang, Y., et al., Nanoenzymes: classification, catalytic mechanisms, activity regulation, and applications. *J. Chemical Reviews*, **119**(6), pp 4357-4412 (2019).
345. Patil, S., et al., Protein adsorption and cellular uptake of cerium oxide nanoparticles as a function of zeta potential. *J. Biomaterials*, **28**(31), pp 4600-4607 (2007).
346. Zhang, M., et al., Antibacterial mechanism and activity of cerium oxide nanoparticles. *J. Science China Materials*, **62**(11), pp 1727-1739 (2019).
347. Xu, Y., et al., Design strategies for ceria nanomaterials: untangling key mechanistic concepts. *J. Materials Horizons*, **8**(1), pp 102-123 (2021).

348. Yu, W., et al., Rapid evaluation of oxygen vacancies-enhanced photogeneration of the superoxide radical in nano-TiO₂ suspensions. *J. Research Advances*, **10**(49), pp 29082-29089 (2020).
349. Nosaka, Y. and Nosaka, A.Y., Generation and Detection of Reactive Oxygen Species in Photocatalysis. *J. Chemical Reviews*, **117**(17), pp 11302-11336 (2017).
350. Ferreira, C. A., et al., Scavenging of reactive oxygen and nitrogen species with nanomaterials. *J. Nano Research*, **11**(10), pp 4955-4984 (2018).
351. Thakur, N., et al., Synthesis and biomedical applications of nanoceria, a redox active nanoparticle. *J. Nanobiotechnology* **17**(1), pp 84 (2019).
352. Reygaert, W. C., An overview of the antimicrobial resistance mechanisms of bacteria. *J. AIMS Microbiology*, **4**(3), pp 482-501 (2018).
353. Popova, N. R., et al., Ceria-Containing Hybrid Multilayered Microcapsules for Enhanced Cellular Internalisation with High Radioprotection Efficiency. *J. Molecules*, **25**(13), pp 2957 (2020).
354. Ribet, D. and Cossart P., How bacterial pathogens colonize their hosts and invade deeper tissues. *J. Microbes and Infections*, **17**(3), pp 173-83 (2015).
355. Santos, C. L., et al. Nanomaterials with Antimicrobial Properties, Applications in Health Sciences. (2013).
356. Aruguete, D. M., et al., Antimicrobial nanotechnology: its potential for the effective management of microbial drug resistance and implications for research needs in microbial nanotoxicology. *J. Environmental Science*, **15**(1), pp 93-102 (2013).
357. Zeyons, O. I., et al., Direct and indirect CeO₂ nanoparticles toxicity for *Escherichia coli* and *Synechocystis*. *J. Nanotoxicology*, **3**(4), pp 284-295 (2009).
358. Li, Y., et al., Mechanism of Photogenerated Reactive Oxygen Species and Correlation with the Antibacterial Properties of Engineered Metal-Oxide Nanoparticles. *J. ACS Nano*, **6**(6), pp 5164-5173 (2012).
359. Qi, M., et al., Cerium and Its Oxidant-Based Nanomaterials for Antibacterial Applications: A State-of-the-Art Review. *J. Frontiers in Materials*, **7**(213) (2020).
360. Chen, Z., et al., A Multinuclear Metal Complex Based DNase-Mimetic Artificial Enzyme: Matrix Cleavage for Combating Bacterial Biofilms. *J. Angewandte Chemie*, **55**(36), pp 10732-10736 (2016).
361. Antoine Thill, O.Z., Olivier Spalla, Frankck Chauvat, Jerome Rose, Melanie Auffan, and Anne Marie Flank Cytotoxicity of CeO₂ nanoparticles for *Escherichia Coli*. physico-chemical insight of the cytotoxicity mechanism. *J. Environtal Science and Technology*, **40**, pp 6151-6156 (2006).
362. Wang, Q., et al., Inhibited growth of *Pseudomonas aeruginosa* by dextran- and polyacrylic acid-coated ceria nanoparticles. *J. Nanomedicine* **8** pp 3395-3399 (2013).
363. Kasinathan, K., et al., Photodegradation of organic pollutants RhB dye using UV simulated sunlight on ceria based TiO₂ nanomaterials for antibacterial applications. *J. Scientific Reports*, **6** pp 38064 (2016).
364. Surendra, T. V. and Roopan, S. M., Photocatalytic and antibacterial properties of phytosynthesized CeO₂ NPs using *Moringa oleifera* peel extract. *J. Photochemical and Photobiology B*, **161**, pp 122-128 (2016).
365. Zhang, J., et al., Effect of cerium ion on the proliferation, differentiation and mineralization function of primary mouse osteoblasts *in vitro*. *J. Rare Earths*, **28**(1), pp 138-142 (2010).
366. Salinas, A. J., et al., Substitutions of cerium, gallium and zinc in ordered mesoporous bioactive glasses. *J. Acta Biomaterialia*, **7**(9), pp 3452-3458 (2011).

367. Zhang, J. and Zhu, Y., Synthesis and characterization of CeO₂-incorporated mesoporous calcium-silicate materials. *J. Microporous and Mesoporous Materials*, **197**, pp 244-251 (2014).
368. Ying Hu, Y. D., Huan Jiang, Guang-Shui Jiang, Cerium promotes bone marrow stromal cell migration and osteogenic differentiation via smad1/5/8 signaling pathway. *J. Clinical and Experimental Pathology*, **7**(8) pp 5369-5378 (2014).
369. Ball, J. P., et al., Biocompatibility evaluation of porous ceria foams for orthopedic tissue engineering. *J. Biomedical Material Research A*, **103**(1), pp 8-15 (2015).
370. Froes, F. H., Titanium Alloys: Properties and applications, in *Encyclopedia of materials: Science and technology* (2015).
371. Lai, Y. S., et al., The effect of graft strength on knee laxity and graft in-situ forces after posterior cruciate ligament reconstruction. *J. Plos One*, **10**(5), pp e0127293 (2015).
372. Young Rho, J. et al., Young's Modulus of trabecular and cortical bone material: ultrasonic and microtensile measurements. *J. Biomechanics*, **26**(2), pp 111-119 (1993).
373. Boyer, R., et al., *ASM International: Materials Properties Handbook - Titanium Alloys*. ASM International.
374. Jameson, J. R., Characterization of bone material properties and microstructure in osteogenesis imperfecta/brittle bone disease. Marquette University, (2009),
375. Soares, P. B., et al., Measurement of elastic modulus and Vickers hardness of surround bone implant using dynamic microindentation--parameters definition. *J. Brazilian Dental*, **25**(5), pp 385-390 (2014).
376. Wachtel, E. and Lubomirsky, I., The elastic modulus of pure and doped ceria. *J. Scripta Materialia*, **65**(2), pp 112-117 (2011).
377. Morgan, L. M., et al., Protecting ceria nanocatalysts-The role of sacrificial barriers. *J. Applied Material Interfaces*, **10**(38), pp 32510-32515 (2018).
378. Gommeringer, A., et al., Ytria Ceria Co-Stabilized Zirconia Reinforced with Alumina and Strontium Hexaaluminate. *J. Applied Sciences*, **9**(4), pp 729 (2019).
379. Roa, J. J., et al., Study of the mechanical properties of CeO₂ layers with the nanoindentation technique. *J. Thin Solid Films*, **518**(1), pp227-232 (2009).
380. Cherneva, S et al., Investigation of mechanical properties of mono-and multi-layer alumina and ceria films using finite element modeling and nanoindentation experiments. *J. Engineering Materials and technology transactions*, **141**(1), pp 011006-1-011006-10 (2019).
381. Patel, S. B., Structural and mechanical study of CeO₂/TiO₂ mixed metal oxide thin films, in *Physics and nanotechnology*..Murdoch University, (2018).
382. Wang, Y., et al., The effect of oxygen vacancy concentration on the elastic modulus of fluorite-structured oxides. *J. Solid State Ionics*, **178**(1-2), pp 53-58. (2007).
383. Amra, M., et al., Mechanical Properties and Corrosion Behavior of CeO₂ and SiC Incorporated Al5083 Alloy Surface Composites. *J. Materials Engineering and Performance*, **24**(8), pp 3169-3179 (2015).
384. Lichinchi, M., et al., Simulation of Berkovich nanoindentation experiments on thin films using finite element method. *J. Thin Solid Films*, **312**(1-2), pp 240-248 (1998).
385. Shcherbakov, A. B., et al., Nanocrystalline ceria based materials—Perspectives for biomedical application. *J. Biophysics* **56**(6), pp 987-1004 (2012).
386. Priyadarshini. B et al., Preparation and characterization of sol-gel derived Ce⁴⁺ doped hydroxyapatite and its *in vitro* biological evaluations for orthopedic applications. *J. Materials and Design*, **119**, pp 446-455 (2017).
387. Lincks, J., et al., Response of MG63 osteoblast-like cells to titanium and titanium alloy is dependent on surface roughness and composition. *J. Biomaterials*, **19**(23), pp 2219 (1998).

388. Shapira, L. and Halabi, A., Behavior of two osteoblast-like cell lines cultured on machined or rough titanium surfaces. *J. Clinical Oral Implants Research*, **20**(1), pp 50-55 (2009).
389. Kokubo, T. and Takadama, H., How useful is SBF in predicting *in vivo* bone bioactivity? *J. Biomaterials*, **27**(15), pp 2907-2915 (2006).
390. Kokubo, T. and Yamaguchi, S., Novel bioactive materials developed by simulated body fluid evaluation: Surface-modified Ti metal and its alloys. *J. Acta Biomaterialia*, **44**, pp 16-30 (2016).
391. Monteiro, C., et al., Prevention of urinary catheter-associated infections by coating antimicrobial peptides from crowberry endophytes. *J. Scientific Reports*, **9**(1), pp 10753 (2019).
392. Wang P, et al., Limitations of MTT and MTS-based assays for measurement of antiproliferative activity of green tea polyphenols. *PloS one*, **5**(4), pp e10202, (2010).
393. Mehmood, R., et al., Engineering oxygen vacancies through construction of morphology maps for bio-responsive nanocerium for osteosarcoma therapy. *J. Crystal Engineering Comments*, **20**(11), pp 1536-1545 (2018).
394. Wu, H., et al., Hydroxyl radical scavenging by cerium oxide nanoparticles improves Arabidopsis salinity tolerance by enhancing leaf mesophyll potassium retention. *J. Environmental Science*, **5**(7), pp 1567-1583 (2018).
395. Heckert, E. G., et al., The role of cerium redox state in the SOD mimetic activity of nanocerium. *J. Biomaterials*, **29**(18), pp 2705-2709 (2008).
396. Gil, D., et al., Antioxidant Activity of SOD and Catalase Conjugated with Nanocrystalline Ceria. *J. Bioengineering*, **4**(1) pp 18 (2017).
397. Corsi, F., et al., Not Only Redox: The Multifaceted Activity of Cerium Oxide Nanoparticles in Cancer Prevention and Therapy. *J. Frontier Oncology*, **8**: pp 309 (2018).
398. Wang, X., et al., Nanozymes in bionanotechnology: from sensing to therapeutics and beyond. *J. Inorganic Chemistry Frontiers*, **3**(1), pp 41-60 (2016).
399. Wang, B., et al., Fast ionic conduction in semiconductor CeO₂- δ electrolyte fuel cells. *J. Asia Materials*, **11**(1) (2019).
400. Chen, W. F., et al., Effect of intervalence charge transfer on photocatalytic performance of cobalt- and vanadium-codoped TiO₂ thin films. *J. Hydrogen Energy*, **40**(46), pp 16215-16229 (2015).
401. Asadian, M., The influence of atmosphere on oxides crystal growth. (2012).
402. Kang, Y. B. and Jung, I. H., Thermodynamic modeling of oxide phases in the Mn-O System. *J. Metallurgical and Materials Transactions E*, **3**(3), pp 156-170 (2016).
403. Grundy, A. N., et al., Assessment of the Mn-O system. *J. Basic and Applied Research: Section I*, **24**, pp21-39 (2002).
404. Kang, Y. B. and Jung I. H., Thermodynamic modeling of oxide phases in the Fe-Mn-O system. *J. Physics and Chemistry of Solids*, **98**: p. 237-246 (2016).
405. Barany, S., et al., Electrokinetic properties and stability of cerium dioxide suspensions. *J. Research Advances*, **6**(73), pp 69343-69351 (2016).
406. Zeyons, O., et al., Direct and indirect CeO₂ nanoparticles toxicity for *Escherichia coli* and *Synechocystis*. *J. Nanotoxicology*, **3**(4), pp 284-295 (2009).
407. Dickson, J.S. and Koohmaraie, M., Cell surface charge characteristics and their relationship to bacterial attachment to meat surfaces. *J. Applied and Environmental Microbiology*, **55**(4), pp 832 (1989).
408. Ong, K. et al., The role of reactive oxygen species in the antimicrobial activity of pyochelin. *J. Advanced Research*, **8**(4), pp 393-398 (2017).

409. Arumugam, A., et al., Synthesis of cerium oxide nanoparticles using *Gloriosa superba* L. leaf extract and their structural, optical and antibacterial properties. *J. Material Science Engineering C*, **49**, pp 408-415 (2015).
410. Properties and selection: Nonferrous alloys and special purpose materials, ASM Handbook Committee, in *Metals Handbook*. Vol. 2, (1978).
411. Hideko H., et al., Thermal expansion of Gd-doped ceria and reduced ceria. *J. Solid state ionics*, **132**, pp 227-233 (2000).
412. R. Korner, et al., Phase transformations in reduced ceria: determination by thermal expansion measurements. *J. Solid state chemistry*, **78**, pp 136-147 (1989).
413. Jiang, S. S. and Zhang, K. F. Study on controlling thermal expansion coefficient of ZrO₂-TiO₂ ceramic die for superplastic blow-forming high accuracy Ti-6Al-4V component. *J. Materials and Design*, **30**(9), pp 3904-3907 (2009).
414. Welsch, G., et al., *Material Properties Handbook: Titanium Alloys*. 1994.
415. Balakrishnan, G., et al., High temperature x-ray diffraction studies of zirconia thin films prepared by reactive pulsed laser deposition. *J. Crystal Research and Technology*, **47**(4), pp 415-422 (2012).
416. Hu, S., et al., Strain control of giant magnetic anisotropy in metallic perovskite SrCoO₃-delta thin films. *J. Applied Material Interfaces*, **10**(26), pp 22348-22355 (2018).
417. Khang, D., et al., The role of nanometer and sub-micron surface features on vascular and bone cell adhesion on titanium. *J. Biomaterials*, **29**(8), pp 970-83 (2008).
418. Krishna Alla, R., et al., Surface roughness of implants: a review. *J. Biomaterials and Artificial Organs*, **25**(3), pp 112-118 (2011).
419. Schierano, G., et al., An alumina toughened zirconia composite for dental implant application: *in vivo* animal results. *J. Biomedical Research*, **2015**, pp 157360 (2015).
420. Goodman, S. B., et al., The future of biologic coatings for orthopaedic implants. *J. Biomaterials*, **34**(13), pp 3174-3183 (2013).
421. Schwartz, J. H., *Skeleton Keys: an introduction to human skeletal morphology, development and analysis*. Oxford University, (2007).
422. Mehmood, R., et al., Surface, Subsurface, and Bulk Oxygen Vacancies Quantified by Decoupling and Deconvolution of *t Surface Roughness of Implants: A Review* the Defect Structure of Redox-Active Nanoceria. *J. Inorganic Chemistry*, **58**(9), pp 6016-6027 (2019).
423. Xu, Y., et al., Design strategies for ceria nanomaterials: untangling key mechanistic concepts. *J. Materials Horizons*, **8**(1), pp 102-123 (2020).
424. Thompson, P., et al., Rietveld refinement of Debye-Scherrer synchrotron X-ray data from Al₂O₃. *J. Applied Crystallography*, **20**(2), pp 79-83 (1987).
425. Holzwarth, U. and Gibson, N. ,The Scherrer equation versus the 'Debye-Scherrer equation'. *J. Nature Nanotechnology*, **6**(9), pp 534-534 (2011).
426. Holzwarth, U. and Gibson, N. ,The Scherrer equation versus the 'Debye-Scherrer equation'. *J. Nature Nanotechnology*, **6**(9), pp 534-534 (2011).
427. Shannon, R. D. and Prewitt, C. T., Effective ionic radii in oxides and fluorides. *J. Acta Crystallographica B*, **25**(5), pp 925-946 (1969).
428. Chen, W. F., et al., Effect of doping on the properties and photocatalytic performance of titania thin films on glass substrates: Single-ion doping with Cobalt or Molybdenum. *J. Materials Chemistry and Physics*, **205**, pp 334-346 (2018).
429. Pearson, W. B., *A handbook of lattice spacings and structures of metals and alloys*. J. Acta Crystallographica, **12**(2), pp 174-174 (1959).
430. Smith, D. W., Electronegativity in two dimensions: Reassessment and resolution of the Pearson-Pauling paradox. *J. Chemical Education*, **67**(11), pp 911-914 (1990).

431. Allred, A. L., Electronegativity Values from Thermochemical Data. *J. Inorganic and Nuclear Chemistry*, **17**(3-4), pp 215-221 (1961).
432. Allred, A. L. and Rochow, E. G., A scale of electronegativity based on electrostatic force. *J. Inorganic and Nuclear Chemistry*, **5**(4), pp 264-268 (1958).
433. Little, E. J. and Jones, M. M. A complete table of electronegativities. *J. Chemical Education*, **37**(5) pp 231 (1960).
434. Bratsch, S. G., Revised mulliken electronegativities: I. calculation and conversion to pauling units. *J. Chemical Education*, **65**(1) pp 34 (1988).
435. Mulliken, R. S., A new electroaffinity scale; together with data on valence states and on valence ionization potentials and electron affinities. *J. Chemical Physics*, **2**(11), pp 782-793 (1934).
436. Mulliken, R. S., Electronic Structures of Molecules XI. Electroaffinity, Molecular Orbitals and Dipole Moments. *J. Chemical Physics*, **3**(9), pp 573-585 (1935).
437. Huheey, J. et al., *Inorganic Chemistry: Principles of Structure and Reactivity* (1993), HarperCollins College Publishers.
438. Pearson, R. G., Absolute electronegativity and hardness: application to inorganic chemistry. *J. Inorganic Chemistry*, **27**(4), pp 734-740 (1988).
439. Sanderson, R. T., Principles of electronegativity Part I. General nature. *J. Chemical Education*, **65**(2), pp 112 (1988).
440. Nagle, J. K., Atomic polarizability and electronegativity. *J. American Chemical Society*, **112**(12), pp 4741-4747 (1990).
441. Naumkin, A. V., et al., NIST X-ray Photoelectron Spectroscopy Database (2012). <https://srdata.nist.gov/xps/Default.aspx>.
442. Yamaguchi, S., et al., Two-in-One biointerfaces-antimicrobial and bioactive nanoporous gallium titanate layers for titanium implants. *J. Nanomaterials*, **7**(8) pp 229 (2017).
443. Goss, C. H., et al., Gallium disrupts bacterial iron metabolism and has therapeutic effects in mice and humans with lung infections. *J. Science translational medicine*, **10**(460), pp eaat7520 (2018).
444. Kröger, F. A. and Vink, H. J. Relations between the concentrations of imperfections in solids. *J. physics and chemistry of solids*, **5**(3), pp 208-223 (1958).
445. Jiang, Y., et al., Enhanced photocatalytic performance of nanostructured TiO₂ thin films through combined effects of polymer conjugation and Mo-doping. *J. Materials Science*, **54**(7), pp 5266-5279 (2019).
446. Bahmanrokh, G., et al., Band gap engineering of Ce-doped anatase TiO₂ through solid solubility mechanisms and new defect equilibria formalism. *J. Nanoscale*, **12**(8), pp 4916-4934 (2020).
447. Chen, W. F., et al., Effects of precipitation, liquid formation, and intervalence charge transfer on the properties and photocatalytic performance of cobalt- or vanadium-doped TiO₂ thin films. *J. Hydrogen Energy*, **41**(42), pp 19025-19056 (2016).
448. Ren, H., et al., Multivalence Charge transfer in doped and codoped photocatalytic TiO₂. *J. Inorganic Chemistry*, **55**(16), pp 8071-8081 (2016).
449. Koch, A. L., *The bacteria: their origin, structure, function and antibiosis*. (2006), Springer.
450. Gottenbos, B., et al., Antimicrobial effects of positively charged surfaces on adhering Gram-positive and Gram-negative bacteria. *J. Antimicrobial Chemotherapy*, **48**(1), pp 7-13 (2001).
451. Langley, S. and Beveridge, T. J., Effect of O-Side-Chain-Lipopolysaccharide Chemistry on Metal Binding. *J. Applied Environmental Microbiology*, **65**(2), pp 489-498 (1999).

452. Sonohara, R., et al., Difference in surface properties between *Escherichia coli* and *Staphylococcus aureus* as revealed by electrophoretic mobility measurements. *J. Biophysics Chemistry*, **55**(3), pp 273-277 (1995).
453. Slavin, Y. N., et al., Metal nanoparticles: understanding the mechanisms behind antibacterial activity. *J. Nanobiotechnology*, **15**(1), pp 65 (2017).
454. Burke, V. and Gibson, F. O., The Gram Reaction and the Electric Charge of Bacteria. *J. Bacteriology*, **26**(2), pp 211-214 (1933).
455. Stearn, E. W. and Stearn, A. E., A study of the chemical differentiation of bacteria. *J. Bacteriology*, **10**(1), pp 13-23 (1925).
456. Stearn, E. W. and Stearn, A. E. The Chemical Mechanism of Bacterial Behavior: II. A New Theory of the Gram Reaction. *J. Bacteriology*, **9**(5), pp 479-489 (1924).
457. Valappil, S. P., et al., Antimicrobial Gallium-Doped Phosphate-Based Glasses. *J. Advanced Functional Materials*, **18**(5), pp 732-741 (2008).
458. Unnithan, A. R., et al., Nanoceria doped electrospun antibacterial composite mats for potential biomedical applications. *J. Ceramics International*, **40**(8), pp 12003-12012 (2014).
459. Qi, M., et al., Cerium and Its Oxidant-Based Nanomaterials for Antibacterial Applications: A State-of-the-Art Review. *J. Frontiers in Materials*, **7**(213) pp 1-26 (2020).
460. Plakhova, T. V., et al., Solubility of Nanocrystalline Cerium Dioxide: Experimental Data and Thermodynamic Modeling. *J. Physical Chemistry C*, **120**(39), pp 22615-22626 (2016).
461. Ferraris, S., et al., Zeta Potential Measurements on Solid Surfaces for *in Vitro* Biomaterials Testing: Surface Charge, Reactivity Upon Contact With Fluids and Protein Absorption. *J. Frontiers in Bioengineering and Biotechnology*, **37**(5), pp 231 (2018).
462. Yavuz, E., et al., Nanosized spongelike Mn_3O_4 as an adsorbent for preconcentration by vortex assisted solid phase extraction of copper and lead in various food and herb samples. *J. Food Chemistry*, **194**, pp 463-469 (2016).
463. Lee, Y. H., et al., Methylamine Treated Mn_3O_4 Nanoparticles as a Highly Efficient Water Oxidation Catalyst under Neutral Condition. *J. Catalysis*, **11**(6), pp 1665-1672 (2019).
464. Corsi, F., et al., Not Only Redox: The Multifaceted Activity of Cerium Oxide Nanoparticles in Cancer Prevention and Therapy. *Frontiers in Oncology*, **8**(309) (2018).
465. Asimeng, B. O., et al., Influence of preferred orientation on the bioactivity of hydroxyapatite: a potential tooth repair and implant surface coating material. *J. Cerâmica*, **66**, pp 340-346(2020).
466. Rincón-López, J. A., et al., Synthesis, Characterization and *in vitro* Study of Synthetic and Bovine-Derived Hydroxyapatite Ceramics: A Comparison. *J. Materials*, **11**(3) pp 333 (2018).
467. Zhuang, Z., et al., Ultrastructural Observation of Hydroxyapatite Ceramics with Preferred Orientation to a-plane Using High-resolution Transmission Electron Microscopy. *J. Procedia Engineering*, **36**, pp 121-127 (2012).
468. Yu, Y., et al., Contrasting *in vitro* Apatite Growth from Bioactive Glass Surfaces with that of Spontaneous Precipitation. *J. Materials*, **11**(9), pp 1690 (2018).
469. Drouet, C., Apatite Formation: Why It May Not Work as Planned, and How to Conclusively Identify Apatite Compounds. *J. BioMedical Research International*, **2013**, pp 490946 (2013).
470. Kim, H. M., et al., The mechanism of biomineralization of bone-like apatite on synthetic hydroxyapatite: an *in vitro* assessment. *J. Interface*, **1**(1), pp 17-22 (2004).

471. Weng, J., et al., The role of amorphous phase in nucleating bone-like apatite on plasma-sprayed hydroxyapatite coatings in simulated body fluid. *J. Materials Science Letters*, **16**(4), pp 335-337 (1997).
472. Lusvardi, G., et al., P(2)O(5)-Free Cerium Containing Glasses: Bioactivity and Cytocompatibility Evaluation. *J. Materials*, **12**(19) (2019).
473. Franchini, M., et al., Gallium-containing phospho-silicate glasses: synthesis and *in vitro* bioactivity. *Mater Sci Eng C Mater Biol Appl*, **32**(6), pp 1401-1406 (2012).
474. Hosseini, S. and Farnoush, H., Characterization and *in vitro* bioactivity of electrophoretically deposited Mn-modified bioglass-alginate nanostructured composite coatings. *J. Materials Research Express*, **6**(2), pp 025404 (2018).
475. Xu, Z., et al., Effect of Immersion in Simulated Body Fluid on the Mechanical Properties and Biocompatibility of Sintered Fe–Mn-Based Alloys. *J. Metals*, **6**(12), pp 309 (2016).
476. Liu, P., et al., Microstructure, mechanical properties, degradation behavior, and biocompatibility of porous Fe-Mn alloys fabricated by sponge impregnation and sintering techniques. *J. Acta Biomaterialia*, **114**, pp 485-496 (2020).
477. Begley, E. R., Guide to refractory and glass reactions. Cahn's Book Division, (1970).
478. Filgueiras, M. R., et al., Solution effects on the surface reactions of a bioactive glass. *J. Biomedical Material Research*, **27**(4), pp 445-453 (1993).
479. Dorozhkin, S. V., Calcium orthophosphates: occurrence, properties, biomineralization, pathological calcification and biomimetic applications. *J. Biomaterialia*, **1**(2), pp 121-64 (2011).
480. Eriksson, A., Bioactivity testing of dental materials, (2019).
481. Vandecandelaere, N., et al., Biomimetic apatite-based biomaterials: on the critical impact of synthesis and post-synthesis parameters. *J. Materials Science*, **23**(11), pp 2593-606 (2012).
482. Drouet, C., Apatite Formation: Why It May Not Work as Planned, and How to Conclusively Identify Apatite Compounds. *J. BioMedical Research International*, **2013**, pp 490946 (2013).
483. Kaygili, O., et al., The effect of simulating body fluid on the structural properties of hydroxyapatite synthesized in the presence of citric acid. *J. Progress in biomaterials*, **5**(3-4), pp 173-182 (2016).
484. Tite, T., et al., Cationic Substitutions in Hydroxyapatite: Current Status of the Derived Biofunctional Effects and Their *In Vitro* Interrogation Methods. *J. Materials*, **11**(11), pp 2081 (2018).
485. Bang, L. T., et al., Carbonate Hydroxyapatite and Silicon-Substituted Carbonate Hydroxyapatite: Synthesis, Mechanical Properties, and Solubility Evaluations. *J. The Scientific World*, **2014**, pp 969876 (2014).
486. Sarma, B. K. and Sarma, B., Role of magnesium on the biomimetic deposition of calcium phosphate. *J. Physics: Conference Series*, **765**, pp 012025 (2016).
487. Keenan, T. J., et al., Structural characterization and anti-cancerous potential of gallium bioactive glass/hydrogel composites. *J. Carbohydrate Polymers*, **153**, pp 482-491 (2016).
488. Zhang, J., et al., The effects of Mn(2+) on the proliferation, osteogenic differentiation and adipogenic differentiation of primary mouse bone marrow stromal cells. *J. Biological Trace Element Research*, **151**(3), pp 415-23 (2013).
489. Bae, Y. J. and Kim, M. H., Manganese supplementation improves mineral density of the spine and femur and serum osteocalcin in rats. *J. Biological Trace Element Research*, **124**(1), pp 28-34 (2008).

490. Pepa, G. D. and Brandi, M. L. Microelements for bone boost: the last but not the least. Clinical cases in mineral and bone metabolism, **13**(3), pp 181-185 (2016).
491. Hirsch, H. R. and J. Engelberg, Determination of the cell doubling-time distribution from culture growth-rate data. J. Theoretical Biology, **9**(2), pp 297-302 (1965).
492. Jung, O., et al., Improved *in vitro* test procedure for full assessment of the cytocompatibility of degradable magnesium based on ISO 10993-5/-12. J. Molecular Sciences, **20**(2), pp 255. (2019).
493. Stoddart, M. J., Mammalian Cell Viability : Methods and Protocols (2011).
494. Jung, O., et al., Optimized *in vitro* procedure for assessing the cytocompatibility of magnesium-based biomaterials. J. Acta Biomaterialia, **23**, pp 354-363 (2015).
495. Grulke, E., et al., Nanoceria: factors affecting its pro- and anti-oxidant properties. J. Environmental Science, **1**(5), pp 429-444 (2014).
496. Wajda, A., et al., Structural characterization and evaluation of antibacterial and angiogenic potential of gallium-containing melt-derived and gel-derived glasses from CaO-SiO₂ system. J. Ceramics International, **44**(18), pp 22698-22709 (2018).
497. Kwon, H. J., et al., Ceria Nanoparticle Systems for Selective Scavenging of Mitochondrial, Intracellular, and Extracellular Reactive Oxygen Species in Parkinson's Disease. J. Angewandte Chemie, **57**(30), pp 9408-9412 (2018).
498. Alpaslan, E., et al., pH-Dependent activity of dextran-coated cerium oxide nanoparticles on prohibiting osteosarcoma cell proliferation. J. Biomaterials Science and Engineering, **1**(11), pp 1096-1103 (2015).
499. Rubio, L., et al., Nanoceria acts as antioxidant in tumoral and transformed cells. J. Chemico-Biological Interactions, **291**, pp 7-15 (2018).
500. Bouchaud, B., et al., pH-distribution of cerium species in aqueous systems. J. Rare Earths, **30**(6), pp 559-562 (2012).